The Effect of the Equation of State on the Properties of Disc-Instability Planets

Adam Fenton

A thesis submitted in partial fulfilment
of the requirements for the degree of
Doctor of Philosophy

Jeremiah Horrocks Institute for Mathematics, Physics and Astronomy
University of Central Lancashire

September 2023

Declaration

Type of Award: Doctor of Philosophy

School: Physical Sciences and Computing

I declare that while registered as a candidate for the research degree, I have not been a registered candidate or enrolled student for another award of the University or other academic or professional institution.

I declare that no material contained in the thesis has been used in any other submission for an academic award and is solely my own work.

No proof-reading service was used in the compilation of this thesis.

Adam Fenton

September 2023

Abstract

The discs around young stars may be massive enough to trigger gravitational instability and fragmentation. This process may form a number of bound objects that collapse to form protoplanets. In this thesis I run hydrodynamic simulations to investigate the effect of the thermodynamics of the disc on the properties of planets that form by gravitational instability.

I model the thermodynamics of a gravitationally unstable disc with the Smoothed Particle Hydrodynamics code PHANTOM, using a barotropic equation of state (EOS) combined with a locally isothermal EOS to provide a minimum temperature floor. In doing so, I mimic the effect of radiative feedback from the central star. I explore a parameter space wherein the critical density (i.e. the density at which the EOS switches from isothermal to adiabatic), the adiabatic index and the initial disc temperature are varied. I discuss the effect of these variations on the properties of protoplanets.

Most of the fragments, regardless of the equation of state used, form second cores (i.e. protoplanets) with masses below the planetary mass threshold (13 M_J) and initial radii of 2-8 $R_\odot$. The mass of the first core increases with steeper equations of state, with the most massive fragments ($> 80\,M_J$) forming with equations of state with $\gamma = 1.8$. Broadly speaking, the fragments that form in discs governed by steeper equations of state have wider first core accretion shocks and higher specific angular momentum. Equations of state with shallow adiabatic zones ($\gamma = 1.2$) form fragments that do not reach sufficiently high temperatures in their centres to trigger

the dissociation of hydrogen and so do not form a second core. These fragments fall in to one of two morphological groups: those with very small first cores with radii of $\sim 0.005 - 0.01\,\mathrm{AU}$ and those first cores with larger radii of $\sim 0.1\,\mathrm{AU}$. The latter group often exhibit evidence of spirals centred on the fragment.

A key finding of this work is that though the fragments that form by gravitational instability are approximately axisymmetric, they show evidence of being flattened and are oblate spheroids rather than spherical objects as has previously been assumed. I also find that fragments accrete gas from the disc from polar-aligned inflows (along with flows on the the disc mid-plane).

I have shown that the fragments that form in gravitationally unstable discs are sensitive to the specific equation of state, with their final mass having a strong dependence on the adiabatic index. I have also found that they are not spherically symmetric and their 3D structure must not be overlooked.

Contents

List of Tables

List of Figures

Acknowledgements

I must, first of all, acknowledge my deepest thanks to my supervisor, Dr. Dimitris Stamatellos for his guidance and encouragement throughout the pursuit of this work. My thanks extend to Dr. Adam Knowles and Dr. Jordan Thirlwall who, in the early days, provided me with the excellent advice, words of encouragement and, particularly the latter, cups of tea where appropriate. The help they provided and reassurance they offered was, and remains, a key element in the completion of this work. I must too thank Dr. Jason Kirk, Dr. Dan Johnson and Simon Ebo for their continuing support over the last few years. My gratitude also extends to a great many people I have met at conferences and workshops whose discussion and insight were deeply helpful. I must also thank the Science and Technology Funding Council for their financial support, without which I would surely still be at square one, only much colder and wetter.

Above all, my family deserve a great thanks. My Father, who taught me everything I know and my Mother, who listened patiently when I encountered something I didn't. My closest friends whose welcome distraction kept me grounded. My partner Sally for her open ear and gentle soul. My deepest thanks goes out to each of them, their endless patience and encouragement when doubt cleared its throat was fundamental to this entire endeavour.

More is thy due than more than all can pay

Chapter 1

Introduction

The Nebula Hypothesis, which suggests the idea of planets forming in discs, has been the subject of research and discussion since the 18th century (Laplace, 1796). However, only in the last 50 years has a description of terrestrial planet formation been postulated. By the 1980's, the core accretion model of giant planet formation (Mizuno, 1980; Stevenson, 1982; Lissauer, 1987; Pollack et al., 1996) had been developed and in the early 1990's the discovery of the first extra-solar planet (exoplanet) heralded a renewed interest in the science of planet formation. The Kepler Space Mission (Koch et al., 2010; Borucki et al., 2010) increased the number of known exoplanets by thousands and, after its retirement in 2018, exoplanet discoveries continue, following the launch of the Transiting Exoplanet Survey Satellite (Ricker et al., 2014). This mission, now in its fourth year, conducts an all sky survey, aiming to discover thousands more exoplanets in its lifetime.

Protoplanetary discs form as a natural consequence of star formation and have been observed around a number of protostars (Chini et al., 2006; Jiang et al., 2008). A collapsing cloud core has angular momentum due to its rotation and/or turbulence so that it forms a disc of material centred on the young protostar (Attwood et al., 2009; Terebey, Shu & Cassen, 1984). For the host star to accrete material from the disc, angular momentum must be lost by the action of disk winds or redistributed

outwards by the action of viscosity (e.g. via spiral arms) (Lynden-Bell & Pringle, 1974; Pringle, 1981).

In Chapter 1, I begin with an introduction to the properties of protoplanetary discs, their evolution and their structure. Then models for giant planet formation will be discussed. Finally, I will briefly discuss the properties of exoplanets and outline the structure of this work.

1.1 Classification of Young Stellar Objects

The existence of discs around Young Stellar Objects (YSOs) is suggested by the infra-red excess in their spectral energy distributions (SEDs). The emission profile at longer wavelengths is enhanced beyond that of a blackbody due to absorption and re-emission of radiation by the dust in the disc. YSOs are classified in terms of the slope, α_{IR}, of the SED between 2 and 25 μm (Williams & Cieza, 2011; Lada, 1987; Andre, Montmerle & Feigelson, 1987) given by

$$\alpha_{IR} \equiv \frac{\mathrm{dlog}\nu \mathrm{F}_\nu}{\mathrm{dlog}\nu} \equiv \frac{\mathrm{dlog}\lambda \mathrm{F}_\lambda}{\mathrm{dlog}\lambda}, \tag{1.1}$$

where ν and λ are the frequency and wavelength of the emission with fluxes F_ν and F_λ, respectively. The SED classification begins with Class 0 objects. These objects are highly obscured and show no near IR emission. These are the youngest sources in the classification system and were added to the class system by Andre, Ward-Thompson & Barsony (1993) following the improvement in the detection of faint millimetre emission. Following these are the Class I-III objects that feature an SED excess with slope ranges given in Table 1.1.

Table 1.1: SED Classification of YSOs

	α_{IR}
Class 0	Undefined
Class I	$\alpha_{IR} > 0.3$
Flat Spectrum Sources	$-0.3 < \alpha_{IR} < 0.3$
Class II	$-1.6 < \alpha_{IR} < -0.3$
Class III	$\alpha_{IR} < -1.6$

1.2 Properties of Discs

The properties of discs that form as a consequence of the collapse of a molecular cloud are likely affected by the specific conditions of the cloud itself. Given the wide variety of cloud masses and rotation rates (Goodman et al., 1993), we expect an equally wide variety in disc properties. In this section I will discuss the general properties of discs around YSOs.

1.2.1 Disc Radii

The difficulty in measuring precise disc sizes stems from the weak emission in the cool outer regions; it is a matter of resolution and sensitivity which requires high sensitivity observations at long wavelengths, which is possible only with large interferometers such as ALMA. Additionally, aerodynamic drag cause the orbits of dust grains to decay, resulting in an inward drift (Weidenschilling, 1977; Adachi, Hayashi & Nakazawa, 1976). This causes a separation between the gaseous and dust-rich elements of the disc, further complicating the issue of constraining the disc extent. Due to these complications, a practical approach is followed that defines the disc

extent R_j as the radius that contains some fraction of the emission of a tracer j. By way of example, Tripathi et al. (2017) define the effective radius $R_{\rm eff}$ of the disc to be that which contains 90% of the millimetre emission. This empirical definition is common in observational studies of protoplanetary discs. Ansdell et al. (2018) utilise ALMA to study the discs around stars in the Lupus star forming region, defining the dust disc radii ($R_{\rm dust}$) as that which encloses 90 % of the total flux at 1.33mm. The same method is applied to determine the gas disc radii ($R_{\rm gas}$) which is defined as that which contains 90% of the emission from ^{12}CO. In this study, $R_{\rm gas}$ is found to be universally larger than $R_{\rm dust}$ by an average factor of 1.96. $R_{\rm dust}$ and $R_{\rm gas}$ range from 38-334 AU and 68-462 AU, respectively.

1.2.2 Disc Mass

Disc mass is fundamental to the stability of a protoplanetary disc. However, for similar reasons to those outlined in § 1.2.1, disc masses are difficult to constrain. Observational estimates for the masses of protoplanetary discs have been made using millimetre emission from dust grains (Andre & Montmerle, 1994; Beckwith et al., 1990). This gives the mass of the dust in the disc; a gas-to-dust ratio is then assumed to calculate the total disc mass. Jørgensen et al. (2009) study an ensemble of Class 0 and Class I continuum observations from the Submillimeter Array (SMA) in an effort to constrain disc masses. They determine that disc masses around Class 0 and Class I objects range from $0.01\,{\rm M}_\odot$ to $0.1\,{\rm M}_\odot$. In the context of gravitational instability (GI), Stamatellos et al. (2011) discuss the mass required to facilitate disc fragmentation. They argue that, given observational evidence for the ratio of rotational to gravitational energy being of order $\beta = 0.02$, massive extended discs should be fairly common. Indeed, observational evidence in the last decade suggests that protostellar discs may have masses that are 10% or more of the mass of their host star (Veronesi et al., 2021; Paneque-Carreño et al., 2021; Tobin et al.,

2012). Additionally, in the early embedded stage of star formation, the discs around protostars are not isolated and may be subject to mass loading from the natal cloud core which may have an affect on the ability of the disc to fragment (Vorobyov & Basu, 2010).

1.2.3 Disc Kinematics

Gas in a disc with a Keplerian velocity profile has an orbital frequency given by

$$\Omega_{\rm k}(R) = \sqrt{\frac{GM_*}{R^3}}, \tag{1.2}$$

where M_* is the mass of the central star and R is the distance from it.

Measuring the velocity profile of early stage discs is non-trivial due to them being highly obscured by the in-falling envelope. Observations of discs need high angular resolution to resolve their kinematics, requiring the use of interferometers such as ALMA and the Submillimeter Array (SMA). Brinch et al. (2007) observed a young protoplanetary disc around the Class I object L1489 IRS; they were able to achieve sufficient resolution with the SMA to observe the inner disc on scales of $\approx 100\,\mathrm{AU}$ using the HCO+ J=3-2 emission as a tracer of high density gas. This study found that even this relatively young, embedded disc has a Keplerian rotational profile. Evidence for Keplerian rotation has since been found in a variety of Class I disks (Lommen et al., 2008; Takakuwa et al., 2012; Yen et al., 2013)

Maret et al. (2020) suggest that Keplerian discs around Class 0 sources larger than 50 AU are rare but make the poignant suggestion that observing such objects is difficult owing to the emission begin dominated by the in-falling envelope. Murillo et al. (2013) also find evidence for discs in Keplerian rotation around Class 0 protostars, suggesting that Keplerian discs can be formed at this stage of protostellar evolution at large radii up to 150 AU.

1.3 Disc Structure

1.3.1 Surface Density

The surface density Σ, of a disc provides a description of how mass is distributed throughout its radii and is given by the integral of the volume density ρ through the vertical direction z,

$$\Sigma(R) = \int_{-\infty}^{+\infty} \rho(R, z)\, dz. \tag{1.3}$$

Σ typically follows a power law with the form $\Sigma \propto R^{-p}$ where the index p lies within the range of 0.2 - 1 (Kitamura et al., 2002; Lay, Carlstrom & Hills, 1997; Wilner et al., 2000; Andrews & Williams, 2007). Millimetre observations of a collection of discs were carried out by Andrews & Williams (2007) and a simple power law of the form in Eq. (1.3) is used to fit observations. This study finds a median surface density profile with an index of p = 0.5. Observations using the isotopolgue CO as a gas tracer indicated that modelling disc surface density as a simple power law may be an over simplification. McCaughrean & O'Dell (1996) found that an exponential taper in surface density was required to fit the observed flux of discs in the Orion Nebula. This tapered profile is predicted by physical models of viscous accretion discs (Hartmann et al., 1998; Lynden-Bell & Pringle, 1974) and takes the form

$$\Sigma(R) = (2-\gamma)\frac{M_{\rm d}}{2\pi R_{\rm c}^2}\left(\frac{R}{R_{\rm c}}\right)^{-\gamma} \exp\left[-\frac{R}{R_{\rm c}}^{2-\gamma}\right], \tag{1.4}$$

where $M_{\rm d}$ is the disc mass, γ specifies the radial dependence of viscosity such that $\nu \propto R^{-\gamma}$, and $R_{\rm c}$ is the critical radius at which the profile deviates from the power law and tapers according to the exponential component. Hughes et al. (2008) model the surface densities of 4 discs using a truncated power law and the taper profile of Equation 1.4. They find that the power law, owing to it being truncated at a particular outer radius, underestimates the extent of the disc outer edge when compared to the observed CO emission. The tapered profile reproduces the observations much better with the average best fit parameters across the 4 discs being $\langle\gamma\rangle = 0.9$.

1.3.2 Thermal Structure

A disc is described as passive if its thermal properties are set only by irradiation from the central star or active if it generates heat by viscous processes. For a razor thin passive disc, the stellar radiation incident on an disc element decreases according to an inverse square law with the distance to the star, i.e. as R^{-2}. Additionally, the incident angle of the radiation decreases linearly as R^{-1} for a geometrically thin disc. This means that the total radiation incident on a disc element decreases as R^{-3} i.e.

$$F_{\text{incident}} \propto \sigma T_*^4 \left(\frac{R}{R_*}\right)^{-3}, \tag{1.5}$$

where σ is the Stefan-Boltzmann constant, T_* and R_* are the temperature and radius of the star, respectively. If the disc radiates like a black body then

$$F_{\text{emitted}} \propto \sigma T_d^4(R), \tag{1.6}$$

where $T_d(R)$ is the temperature of the disc at a radius R. Then by setting $F_{\text{incident}} = F_{\text{emitted}}$ the temperature of the disc at a radius R from the star is given by

$$T_d \propto T_* \left(\frac{R}{R_*}\right)^{-3/4}. \tag{1.7}$$

By considering the disc scale height $H = c_{\text{s}}/\Omega$ where c_{s} is the sound speed which itself has the dependence $c_{\text{s}} \propto T^{1/2}$, Equation 1.7 can be used to show that the aspect ratio of the disc has a radial dependence such that $H/R \propto R^{1/8}$. This shows that the disc is flared, i.e. its scale height increases with radius. A flared disc absorbs far more radiation than a geometrically thin one.

Active discs generate heat through viscous processes. Considering that 1/2 of the energy generated by the transfer of material inward in an annulus between radii R and ΔR is radiated away via blackbody radiation, then

$$\frac{GM_*\dot{M}}{2R}\frac{\Delta R}{R} \simeq 4\pi R \Delta R \sigma T_d^4(R), \tag{1.8}$$

where G is the gravitational constant, and M_* and $\dot{M}$ are the star mass and mass accretion rate, respectively. Then the temperature of the disc is given by

$$T_d(R) \simeq \left(\frac{GM_*\dot{M}}{8\pi\sigma R^3}\right)^{1/4}. \tag{1.9}$$

Both passive and active discs have temperature profiles with a $R^{-3/4}$ dependence; the former determined by the luminosity of the central star, the latter depending on the accretion rate in the disc.

1.3.3 Vertical Profile

The vertical structure of the disc is determined by considering the vertical force balance between gravity and thermal pressure force. The vertical component of the gravitational acceleration in a geometrically thin disc at a height z and radius r is given by

$$g_z = \frac{GM_*}{(r^2+z^2)}\frac{z}{(r^2+z^2)^{1/2}}, \tag{1.10}$$

where G is the gravitational constant, M_* is the mass of the star. For a disc to be in hydrostatic equilibrium the vertical component of the gravitational acceleration must be balanced by the thermal pressure acceleration. Up to densities of $\sim 0.1\,\mathrm{g\,cm^{-3}}$ the gas can be considered ideal and assuming that the disc is vertically isothermal, the thermal pressure P is given by $P = \rho c_s^2$ where c_s is the sound speed,

$$c_s = \sqrt{\frac{kT}{\mu m_h}}, \tag{1.11}$$

where k is the Boltzmann constant, T is the temperature of the gas, μ is the mean molecular weight, and m_h is the mass of a hydrogen atom. Equating the vertical component of gravitational acceleration and thermal pressure acceleration gives the separable differential equation

$$\frac{1}{\rho}\frac{dP}{dz} = -\frac{GM_*z}{(r^2+z^2)^{3/2}}. \tag{1.12}$$

For the case of a geometrically thin disc with $z << r$ and where the gas can considered ideal, we can substitute $P = \rho c_s^2$ and Equation 1.12 becomes

$$\frac{1}{\rho}\frac{d\rho}{dz} = -\frac{GM_* z}{r^3 c_s^2}. \tag{1.13}$$

Integrating both sides of Equation 1.13 yields

$$\ln(\rho) = -\frac{GM_* z^2}{2(r^3 c_s^2)} + C, \tag{1.14}$$

where C is the constant of integration. By recognising that the disc scale height is given by $h = c_\mathrm{s}/\Omega$ where $\Omega = \sqrt{GM_*/r^3}$, Equation 1.14 becomes

$$\ln(\rho) = -\frac{-z^2}{2h^2} + C, \tag{1.15}$$

and taking the inverse natural logarithm i.e. e^x of both sides of Equation 1.15 gives

$$\rho = \rho_0 e^{-z^2/2h^2}. \tag{1.16}$$

In Equation 1.16, the mid-plane density ρ_0 can be expressed in terms of the surface density of the disc such that

$$\rho_0 = \frac{1}{\sqrt{2\pi}}\frac{\Sigma}{h}. \tag{1.17}$$

1.4 Viscous Disc Evolution

The viscosity of the disc allows for the redistribution of angular momentum. Material, through the effect of viscosity, loses angular momentum and is allowed to spiral inward toward the star. It is this mechanism by which the star accretes material from the disc. The conservation of angular momentum implies that material must also gain angular momentum and migrate outwards, which leads to 'viscous spreading' of the disc. By considering the conservation of mass and angular momentum, Lynden-Bell & Pringle (1974) find that the evolution of surface density is given by

$$\frac{\partial \Sigma}{\partial t} = \frac{3}{r}\frac{\partial}{\partial r}\left[r^{1/2}\frac{\partial}{\partial r}(\nu \Sigma r^{1/2})\right], \tag{1.18}$$

where ν is the kinematic viscosity. Typically, the viscosity of a disc is considered in terms of the Shakura and Sunyaev prescription of an $\alpha-$viscosity (Shakura & Sunyaev, 1973) in which the viscosity is controlled by a dimensionless parameter α_{ss}. In this implementation, the viscosity is set via the sound speed c_s and the scale height h of the disc,

$$\nu = \alpha_{ss} c_s h. \tag{1.19}$$

1.5 Gravitational Instability

The occurrence of planets on wide orbits has been the subject of a number of observational surveys over the last two decades. Direct imaging surveys have explored the outer, cooler regions of discs ($\geq 20 - 30\,\mathrm{AU}$) and the properties of the cool, giant planets that form therein (Biller et al., 2007; Lafreniere et al., 2007; Heinze et al., 2010; Chauvin et al., 2010; Vigan et al., 2012; Bowler, 2016). Advances such as the SPHERE instrument (Beuzit et al., 2019) and James Webb Space Telescope (Gardner et al., 2006) have ushered in a new epoch of direct observations of exoplanets on wide orbits. Recent surveys using the SPHERE (Desidera et al., 2021) and Gemini Planet Imager (Nielsen et al., 2019) suggest that the population of giant planets on wide orbits is small. However, these observational surveys provide evidence to compare to populations synthesis models of planets in discs. Vigan et al. (2012) suggest that core accretion is a viable mechanism for the formation of giant planets inside of 10 AU while gravitational fragmentation tends to form planets with masses $> 10\mathrm{M_J}$ outside of 10 AU (Forgan, Ilee & Meru, 2018; Emsenhuber et al., 2021). Comparing these models with detections of planets by direct imaging (which has a natural bias to planets on wide orbits) suggests that these planets may have formed by gravitational instability rather than via core accretion. Figure 1.1 shows the distribution of exoplanet masses as a function of their semi major axis[1]. The

[1] *https://exoplanetarchive.ipac.caltech.edu [Accessed: 07/11/2022]*

high-mass, wide-orbit 'Cold Jupiters' are indicated by the red points.

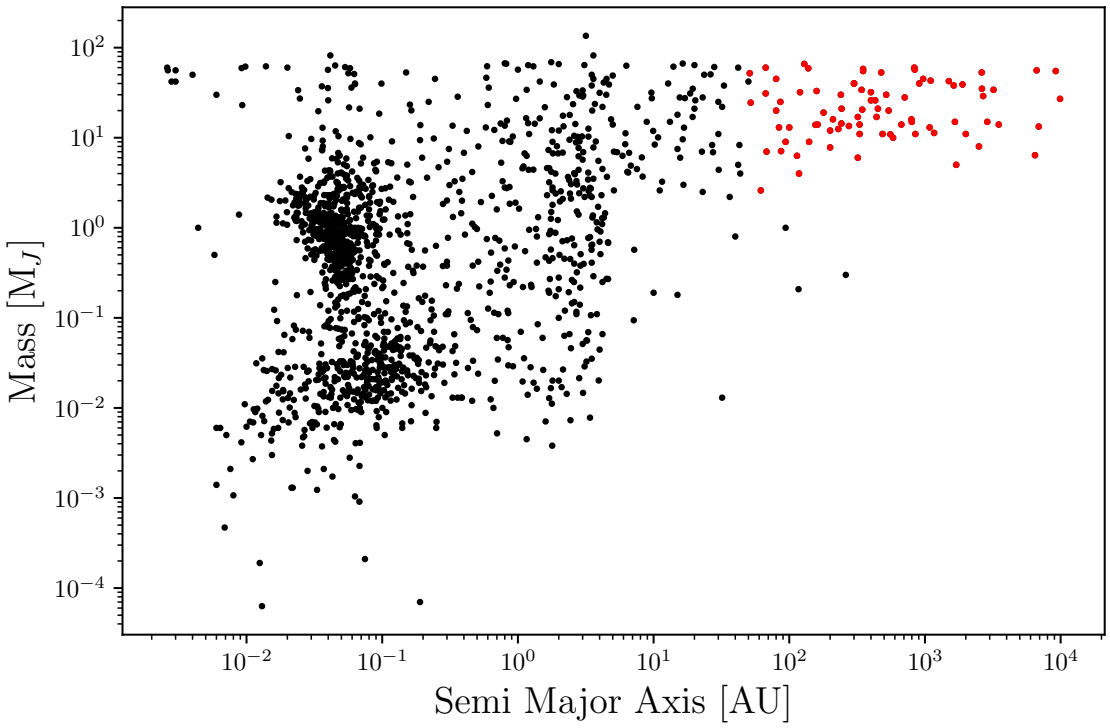

Figure 1.1: The distribution of exoplanet masses as a function of their semi major axis. The points in red correspond to wide-orbit planets ($a > 50\,\mathrm{AU}$) that have masses $M \geq 1\,\mathrm{M_J}$. These objects challenge the theory of giant planet formation by core accretion. (Plotted with data obtained from the NASA exoplanet archive.)

These objects challenge the core accretion model of giant planet formation as the time needed for them to form by the gradual coagulation of matter in the outer regions of the disc, where material is sparse, may exceed the disc lifetime which has been estimated to be $\sim 5 - 10\,\mathrm{Myr}$ (Haisch, Jr., Lada & Lada, 2001; Ribas et al., 2014). Figure 1.2 shows an ensemble of observations of star forming regions and their approximate disc fraction as a function of age. The point at which the disc fraction reduces to zero gives an approximate value for the maximum disc lifetime of $\sim 10\,\mathrm{Myr}$.

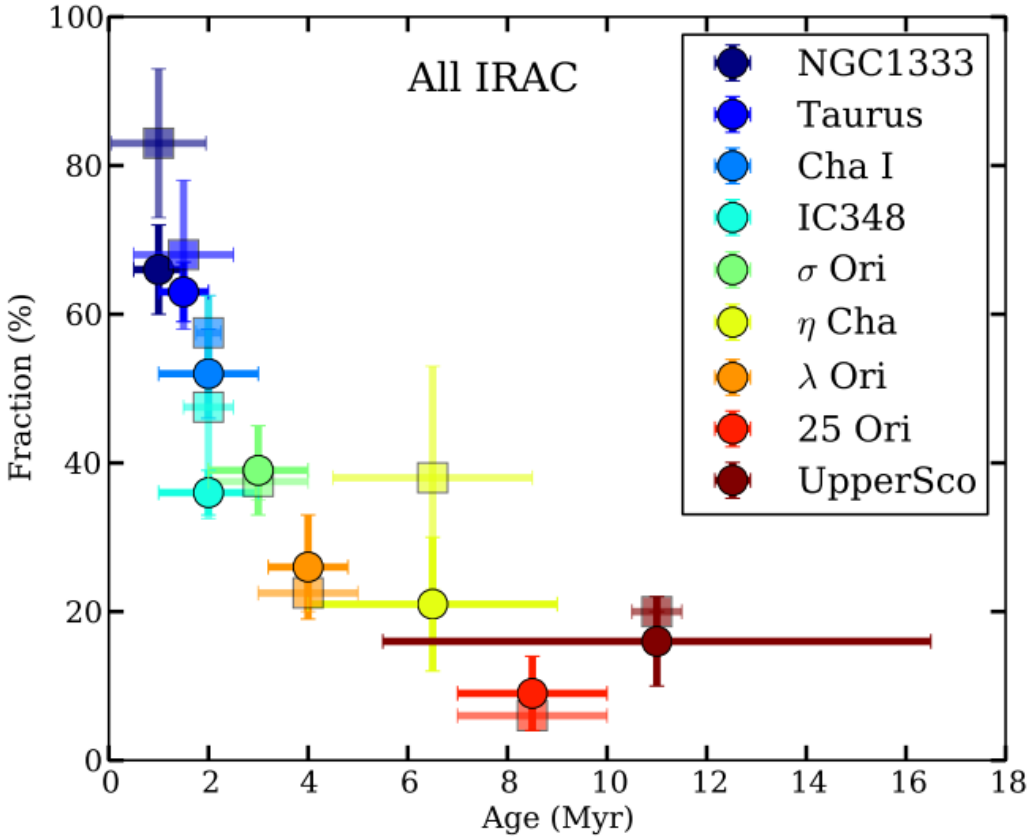

Figure 1.2: The disc fraction in a number of observations of star forming regions. An estimate for the lifetime of discs around stars is given by the time after which the disc fraction has reduced to 0. Taken from Ribas et al. (2014).

Simulations carried out by Dodson-Robinson et al. (2009) follow the accretion of a 0.1 $M_{\oplus}$ seed core for disc lifetime of 5 Myrs. The core has the potential to accrete a gaseous envelope if its mass increases to 10 $M_{\oplus}$. Their results suggest that core accretion cannot form giant planets on stable orbits with semi major axes greater that 35 AU.

Gravitational instability offers an alternate formation mechanism for high mass objects on wide orbits (Kuiper, 1951; Boss, 1997). Assuming a gravitationally unstable disc develops fragments with a characteristic size Δr and a mass $m \sim \pi \Delta r^2 \Sigma$

where Σ is the local surface density, this fragment will collapse on the free fall timescale given by

$$t_{\rm ff} \sim \sqrt{\frac{\Delta r}{\pi G \Sigma}}, \tag{1.20}$$

where G is the gravitational constant. In this scenario, the shear and thermal pressure act to stabilise the fragment. The shear timescale, the timescale on which the fragment is sheared azimuthally by Δr is given by

$$t_{\rm shear} \sim \Omega^{-1}, \tag{1.21}$$

where Ω is the Keplerian angular velocity. The thermal pressure timescale is given by the time taken for a sound wave to cross the fragment, i.e.

$$t_{\rm p} \sim \frac{\Delta r}{c_{\rm s}}, \tag{1.22}$$

where $c_{\rm s}$ is the sound speed. By equating Equations 1.21 and 1.22, the scale Δr is represented in terms of the sound speed and angular velocity,

$$\frac{\Delta r}{c_{\rm s}} \sim \frac{1}{\Omega} \longrightarrow \Delta r \sim \frac{c_{\rm s}}{\Omega}. \tag{1.23}$$

For gravitational instabilities to develop, the free fall timescale must be shorter than the shear and pressure timescales,

$$\sqrt{\frac{\Delta r}{\pi G \Sigma}} \leq \frac{\Delta r}{c_{\rm s}} \tag{1.24}$$

$$\implies \frac{\Delta r}{\pi G \Sigma} \leq \frac{\Delta r^2}{c_{\rm s}^2} \tag{1.25}$$

$$\implies \frac{1}{\pi G \Sigma} \leq \frac{1}{c_{\rm s}\Omega} \tag{1.26}$$

$$\implies \pi G \Sigma \geq c_{\rm s}\Omega \tag{1.27}$$

Equation 1.27 can be represented using the Toomre Q parameter, denoting the condition for gravitation instability

$$Q \equiv \frac{c_{\rm s}\Omega}{\pi G \Sigma} < Q_{\rm crit}, \tag{1.28}$$

where c_s is the sound speed, Ω is the Keplerian orbital frequency and Σ is the local surface density. The critical value of Q, below which the disc is prone to instability, is generally taken as unity. However, a disc that satisfies this condition is not guaranteed to fragment. Instabilities in a disc develop into spiral arms which transport angular momentum outwards (Dong, Najita & Brittain, 2018; Kratter et al., 2010; Kratter & Lodato, 2016; Lodato & Rice, 2004; Rice et al., 2003; Stamatellos & Whitworth, 2008). This outward flow of material causes an inward flow of mass and therefore an increase in disc temperature owing to the dissipation of the energy generated by accretion. The sound speed and surface density therefore increase, causing a corresponding increase in the value of Q. In this way, a gravitationally unstable disc may settle into a quasi-steady state (Lodato & Rice, 2004). If the disc can cool sufficiently fast, the energy generated by gravitational instability can be readily radiated away. In this scenario, the gravitationally unstable regions of the disc can fragment, resulting in the formation of localised high density regions of gas which can undergo further collapse to form bound objects (Gammie, 2001).

Numerical simulations of planet forming discs have revealed that conditions in the outer part of the discs are such that the formation of giant planets by disc instability is viable (Boss, 2008; Mayer et al., 2007; Johnson & Gammie, 2003; Dodson-Robinson et al., 2009; Nero & Bjorkman, 2009).

1.5.1 Observations of Gravitationally Unstable Discs

The surface density required for Equation 1.28 to be satisfied is large. Armitage (2020) shows that for gravitational instabilities to develop in a disc around a solar mass star, the surface densities must be of order $10^3\,\mathrm{g\,cm^{-2}}$. This is an order of magnitude higher than what is expected from the minimum mass solar nebula i.e the minimum disc mass needed to form the planets of our Solar Systems (Weidenschilling, 1977). Discs that satisfy this condition are rare but candidates of sufficient

mass have been observed (Andrews et al., 2009).

Elias 2-27 is a young, Class II object of approximately 0.5-0.6 $M_{\odot}$, hosting a massive disc that exhibits spiral features in the millimetre continuum (Evans et al., 2009; Isella, Carpenter & Sargent, 2009; Ricci et al., 2010). Observations by Pérez et al. (2016) using ALMA reveal two symmetric spiral arms that extend from a ring of emission around the star. The left hand panel of Figure 1.3 shows the 1.3mm dust continuum emission of Elias 2-27. To highlight the spiral and ring features, an unsharp mask is performed on the data, the resulting image is shown in the right hand panel. Paneque-Carreño et al. (2021) argue that due to the symmetry and extent of the spirals in Elias 2-27, they are unlikely to have formed by the presence of a companion though planet-disc interactions. Furthermore, Elias 2-27 has been shown to have a high disc to star mass ratio (Andrews et al., 2009; Ricci et al., 2010), possibly higher that q=0.1, which is considered a threshold for instability. Paneque-Carreño et al. (2021) also show that the disc may be more optically thick than previously reported which may indicate a higher disc mass. The authors conclude by suggesting that the spiral structures in Elias 2-27 are driven by gravitationally instability.

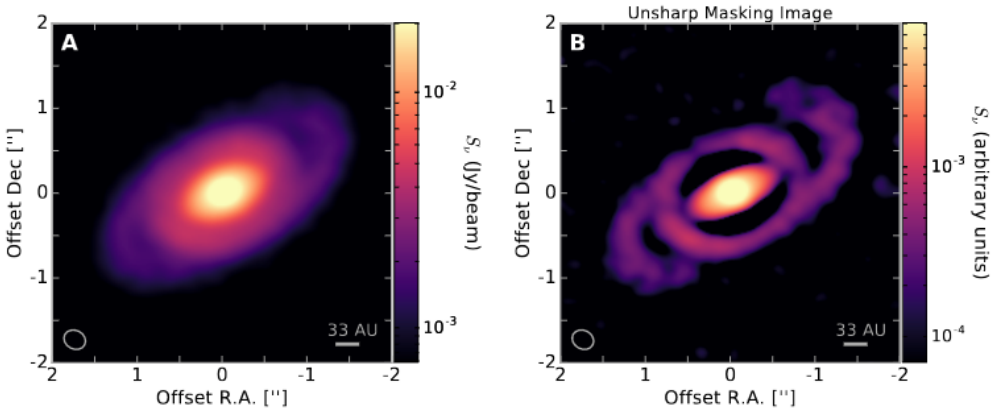

Figure 1.3: Left: 1.33 mm continuum image of Elias 2-27, the colour scale shows the flux density. Right: The original image captured by ALMA following the application of an unsharp mask to highlight the spiral and ring features. Taken from Pérez et al. (2016).

Forgan, Ilee & Meru (2018) examine whether spirals may also be driven by a high mass, wide orbit companion. The left hand panel of Figure 1.4 shows a snapshot from a simulation where the spirals are driven by gravitational instability, while the right hand panel shows spirals induced by a wide orbit companion (red marker). The white points show the location of the spiral features. The GI induced spirals have a constant pitch angle while spirals driven by a companion have pitch angles that increase with radius.

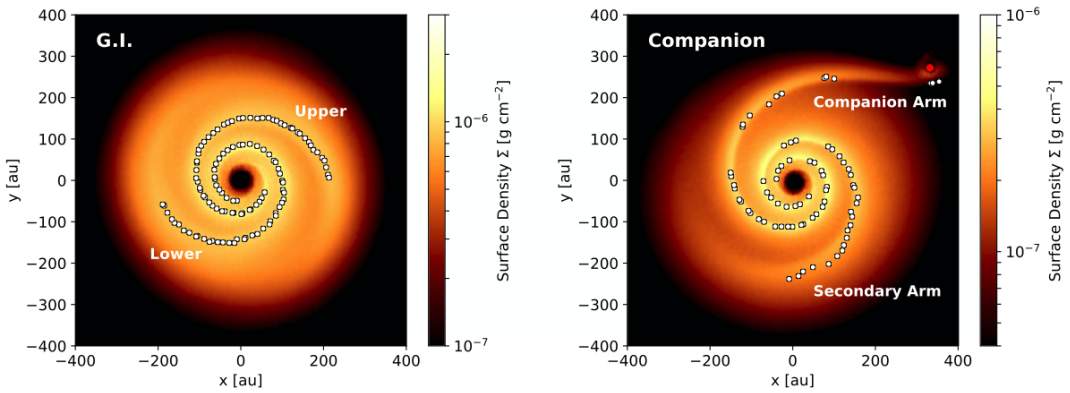

Figure 1.4: A demonstration of spiral arms driven by gravitational instability (left) or a companion (right). The GI induced spirals have a constant pitch angle while those driven by the companion increase with radius. Taken from Forgan, Ilee & Meru (2018).

1.5.2 The GI Wiggle

Spiral waves in discs may be driven by the presence of a high mass planet or a stellar companion (Forgan, Ilee & Meru, 2018; Dong et al., 2015; Dong & Fung, 2017; Fung & Dong, 2015; Price et al., 2018a). However, gravitational instability also induces spirals (Hall et al., 2016, 2019) and so differentiating between the two scenarios when determining the origin of spirals in protoplanetary discs is non-trivial. Hall et al. (2020) propose a method of identifying GI induced spirals by observing the effect they have on the kinematics of the gas in a disc. The authors show that for a disc with Keplerian velocity profile (bottom panels of Figure 1.5), the synthetic channel map does not show any substructure. However, for a disc that is gravitationally unstable, the synthetic channel map shows deviations from the Keplerian profile across the full extent of the disc, rather than a localised kink as would be case for an embedded planet or stellar companion. This is shown in the top panels of Figure 1.5.

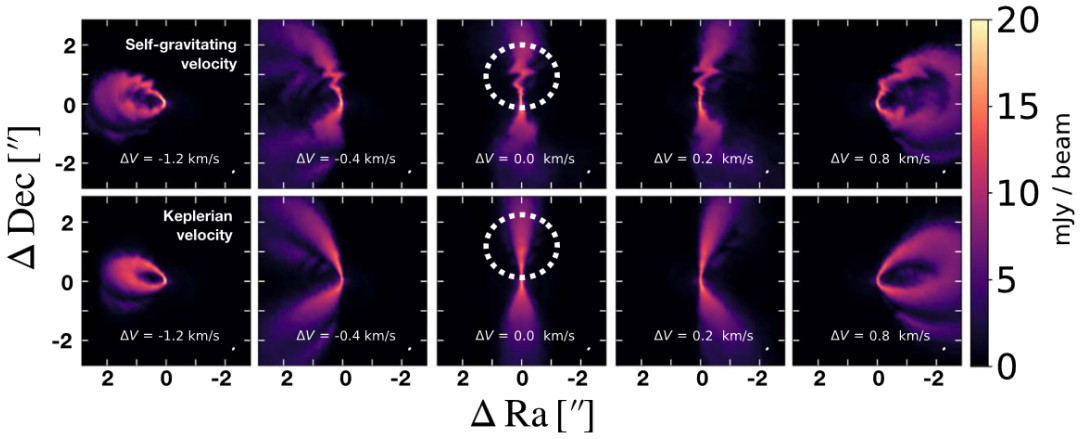

Figure 1.5: Snapshots of a hydrodynamics simulation, post-processed with raditative transfer to produce synthetic emission maps. The top row shows the velocity structure of a self gravitating disc, the bottom shows a disc with a purely Keplerian velocity profile. The 'GI Wiggle' is shown in the circle in the middle panel of the top row, the feature is not present in the Keplerian profile in the bottom row. Taken from Hall et al. (2020).

The perturbations from Keplerian velocity, i.e. the 'GI wiggle', are identified by Hall et al. (2020) as a method by which one can distinguish between planet driven and GI driven spiral modes. Further work by Terry et al. (2022) suggests that a linear relationship exists between the amplitude of the 'wiggle' and the mass ratio M_d/M_* of the system.

1.5.3 Tidal Downsizing

This is an extension to the gravitational fragmentation scenario for planet formation proposed by Nayakshin (2010b) by which terrestrial planets and gas giant planets with solid cores form by the stripping of the outer envelope of a fragment produced by gravitational instability. The process begins with a fragment that begins to migrate inwards owing to the effect of disc torques. Grain sedimentation at the centre of the fragment causes the formation of a solid core. The evolution of the

fragment can then take two possible routes. If the contraction of the initial fragment occurs on a long a timescale, it is tidally disrupted and the solids are released into the disc and form rings of debris, leaving behind a terrestrial core. If contraction occurs on a short timescale, i.e. faster than the inward migration, then a giant gas planet with a solid core forms (see Nayakshin (2017) for a review). Therefore, dividing the population of exoplanets into those that form by core accretion and those that do so by gravitational instability by a threshold radius away from the central star may then be an over simplification. The tidal downsizing hypothesis allows for fragments having originally formed by gravitational instability to end up as planets located within the few tens of AU, a region traditionally thought as the realm of planets formed by core accretion (Nayakshin, 2017, 2010a; Forgan & Rice, 2013; Forgan et al., 2018).

1.6 Thesis Outline

This thesis focuses on the effect of thermodynamics on the formation and evolution of protoplanets in a gravitationally unstable disc. I will use a hybrid version of the barotropic equation of state which, in addition to including adiabatic heating, also accounts for radiative feedback from the star. This is achieved by imposing a minimum temperature floor that is a function of the distance from the star, i.e. $T_{\rm min} \propto R^{-q}$. By varying the adiabatic index, I control the temperature increase of the gas with density which effects how fragments collapse and their final properties. I will also vary the density at which the gas becomes optically thick. This is particularly important for realistic modelling of fragments across a wide range of masses as low mass fragments may become optically thick at higher densities.

Chapter 2 discusses the evolution of a collapsing cloud of gas from the initial stages of collapse through the formation of the first and second cores. I describe how the mechanism of cloud collapse is applied to the formation of fragments in

a gravitationally unstable disc and the evolution of these fragments from diffuse pockets of gas to objects that have evolved to high central densities with first and second hydrostatic cores. Chapter 3 discusses the computational techniques that are utilised in this research. I introduce the underlying fundamentals of numerical hydrodynamics and smoothed particle hydrodynamics (SPH), including a description of self gravity and artificial viscosity. I also discuss the implementation of SPH in this project by highlighting the specifics of the SPH code PHANTOM which is the code used in this work. Chapter 4 discusses the initial conditions that I use to construct the discs in this work. I introduce the density and temperature profiles of the disc and also discuss its rotation and initial stability. The specific thermodynamics that are under investigation in this project are also discussed. In Chapter 5 I present the results of the benchmark simulation where the analysis performed on the data is introduced. This chapter serves as a basis for comparison to the fragments that form in the simulations where the equation of state is varied. In Chapter 6 I present results from simulations with different equations of state and draw conclusions based on the statistics they provide. I summarise the work presented in this thesis in Chapter 7.

Chapter 2

From Cores to Protostars and Protoplanets

Larson (1969) performed numerical calculations to describe the collapse of a molecular cloud to stellar densities under self gravity. This study and its contemporaries (Gaustad, 1963; Hayashi & Nakano, 1965) found that the collapse goes through a series of clearly defined stages; an initial isothermal regime of steady collapse ending with the formation of the first hydrostatic core and a second collapse terminating in the formation of the second hydrostatic core, i.e. the protostar. The same phases apply to the evolution of the low mass fragments that form by gravitational instabilities within a disc from low densities to protoplanets.

2.1 Isothermal Collapse Regime

The collapse of a molecular cloud begins when the thermal pressure of the cloud fails to counteract the gravitational force, i.e.

$$\frac{kT}{\mu m_H} < \frac{GM}{R}, \tag{2.1}$$

where T, M and R are the temperature, mass and radius of the cloud respectively.

Initially, the heating that occurs as a result of compression is low and so the thermal support cannot withstand the gravitational forces and the cloud collapses. During this phase, the cloud is optically thin and so the gravitational energy from the collapse can be radiated away unimpeded and the collapse occurs isothermally on the free fall timescale. The inward flow of material causes an increase in the density of the inner regions. The increased thermal pressure decelerates the collapse, causing the density at the centre of the cloud to increase more rapidly than elsewhere resulting in a centrally peaked distribution as seen in Figure 2.1 (Larson, 1969).

2.2 Formation of the First Core

The collapse is isothermal until the central density reaches $\rho \approx 10^{-13}\,\mathrm{g\,cm^{-3}}$ whereupon the cloud becomes optically thick. At this stage, the thermal energy generated as a result of the collapse cannot be readily radiated away and the temperature at the centre of the cloud increases. The collapse is halted and the first hydrostatic core forms. Its mass and temperature increase gradually as more gas falls towards the centre of the cloud.

The in-falling gas meets the first hydrostatic core and slows down, resulting in a shock front outside the first hydrostatic core with radius of a few AU. This shock front begins to show as a sharp peak at a few AU in the infall velocity, shown in the lower left panel of Figure 2.1.

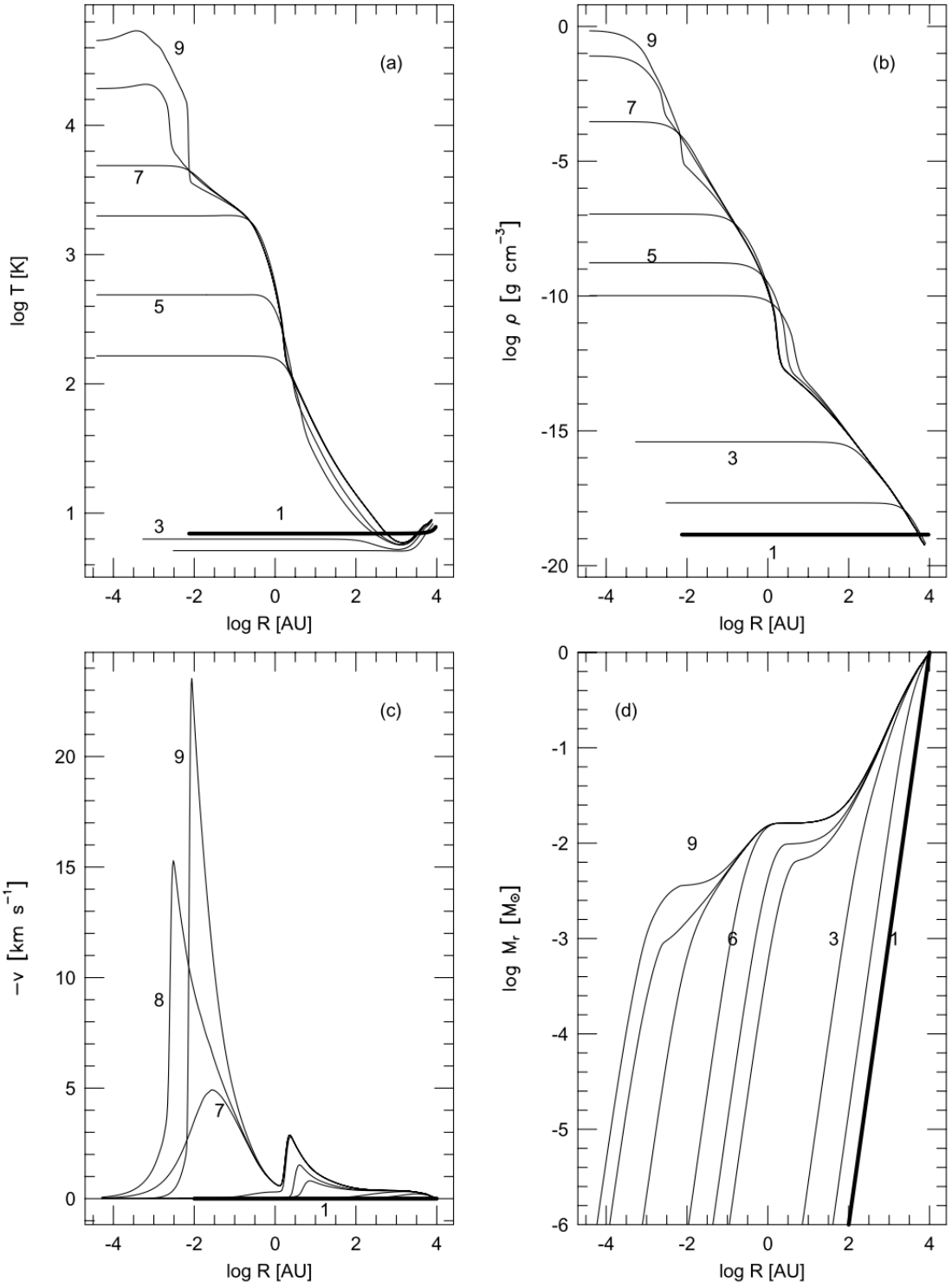

Figure 2.1: The central temperature (a), density (b), infall velocity (c) and mass within a specified radius (d) of the collapsing cloud core. Figure taken from Masunaga & Inutsuka (2000)

2.3 Dissociation of H_2 and the Formation of the Second Core

Following the formation of the first core, the temperature at the centre of the cloud continues to increase. The evolution in the log T - log ρ plane is described by the condition of adiabaticity, i.e.

$$\frac{d\,log\,T}{d\,log\,\rho} = \gamma - 1, \tag{2.2}$$

where γ is the adiabatic exponent, given by the ratio of specific heats $\gamma = c_p/c_v$. The simulations carried out in Masunaga, Miyama & Inutsuka (1998) suggest that the gradient of the evolutionary track in this stage of evolution is $\approx 2/3$, giving, by Equation 2.2, $\gamma = 5/3$. This is consistent with molecular hydrogen which, due to its lack of a dipole moment, behaves as a monotomic gas at low temperatures. (Stamatellos & Whitworth, 2009). This stage of evolution occurs between $\rho \approx 10^{-12}\,\mathrm{g\,cm^{-3}}$ and $\rho \approx 10^{-11}\,\mathrm{g\,cm^{-3}}$ (see Figure 2.2).

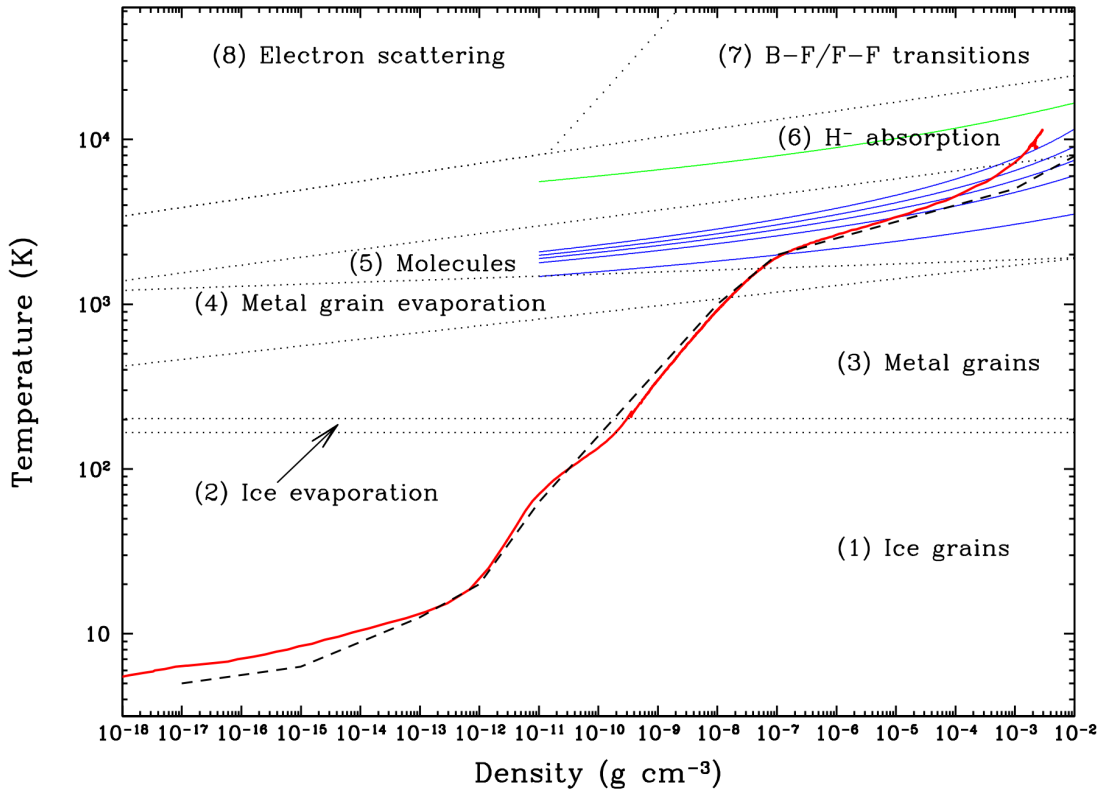

Figure 2.2: The evolution of the centre of a collapsing molecular cloud in the log T - log ρ plane. The results from the simulation using the diffusion approximation of radiative transfer are shown in red and the black dashed line shows the evolution from a 1D hydrodynamic simulation with multi-frequency radiative transfer (Masunaga, Miyama & Inutsuka, 1998). Figure taken from Stamatellos et al. (2007).

Stamatellos et al. (2007) finds that at $\rho \approx 3 \times 10^{-11}\,\mathrm{g\,cm^{-3}}$, the central temperature reaches $T \approx 100K$. At this temperature, the rotational modes of molecular hydrogen are excited, as illustrated by the kink in the red line in Figure 2.2. During this intermediate stage, the adiabatic index γ is 7/5. The temperature at the centre of the cloud increases to 2000 K and molecular hydrogen begins to dissociate, reducing the adiabatic index to 1.1 (Masunaga & Inutsuka, 2000).

The energy resulting from the radiative heating inside the cloud is partially diverted into hydrogen dissociation and so the cloud is no longer sufficiently supported

against further collapse and the second collapse begins. In the simulation carried out by Masunaga & Inutsuka (2000), hydrogen dissociation occurs when the central density reaches approximately $10^{-7}\,\mathrm{g\,cm^{-3}}$. This result is supported by Stamatellos et al. (2007).

The free fall time is given by

$$t_{ff} = \left(\frac{3\pi}{32G\rho}\right)^{1/2}. \tag{2.3}$$

Using this equation for a density of $10^{-7}\,\mathrm{g\,cm^{-3}}$, i.e. the density of the core when hydrogen dissociation begins, we find that the free fall time is approximately 0.1 yrs (Masunaga & Inutsuka, 2000). The second collapse continues until the most of the hydrogen has been dissociated and the central temperature and density of the cloud core are $T \approx 10^4$ K and $\rho \approx 10^{-3}\,\mathrm{g\,cm^{-3}}$ respectively. At this temperature the collapse is again slowed down due to the increase in temperature, resulting in the formation of the second hydrostatic core. Figure 2.1 illustrates the evolution from the formation of the first hydrostatic core through the adiabatic regime to the dissociation of hydrogen. In the lower left panel, the infall velocity shows a sharp peak at the location of the second core at R≈ 0.01 AU. The peak is associated with the accretion shock around the second core.

2.4 Properties of the First and Seconds Cores

Masunaga, Miyama & Inutsuka (1998) define the radius of the core R_{fc}, to be the location at which the gas pressure is balanced by the pressure of the in-falling envelope. They explore the parameter space and present an analysis on the effect of temperature, opacity and initial cloud mass on the value of R_{fc}. Similar exploration of the effect of the initial conditions on the properties of the first and second hydrostatic cores is presented in Stamatellos et al. (2007).

2.4.1 Dependence on Initial Temperature of the Cloud

The density at which the cloud becomes optically thick $\rho_{\tau\approx1}$ is higher by two orders of magnitude for a cloud with an initial temperature of $T = 5\,\mathrm{K}$ than it is for a warmer cloud that is initially at $T = 10\,\mathrm{K}$. This means that the central temperature of the cloud remains low up to higher densities because the thermal energy can be radiated away unimpeded. Masunaga, Miyama & Inutsuka (1998) find that for a cloud with $T_{\mathrm{init}} = 5\,\mathrm{K}$, $\rho_{\tau\approx1} = 2.2 \times 10^{-11}\mathrm{g\,cm^{-3}}$ while with $T_{\mathrm{init}} = 10\,\mathrm{K}$, $\rho_{\tau\approx1} = 4.3 \times 10^{-13}\mathrm{g\,cm^{-3}}$. This causes the first core to form later and at a higher central density. A cloud with a higher initial temperature reaches high opacities faster and at a much reduced density than in both of the previous cases with $\rho_{\tau\approx1} = 8.3 \times 10^{-16}\mathrm{g\,cm^{-3}}$ for the case of $T_{\mathrm{init}} = 30\,\mathrm{K}$. Masunaga, Miyama & Inutsuka (1998) also find that the density at which the compressional heating rate and the radiative cooling rate balance is far higher than $\rho_{\tau\approx1}$ in this case meaning that the value of $\rho_{\tau\approx1}$ no longer forms a signal for first core formation.

The initial temperature of the cloud has only a small effect on the radius of the first core R_{fc}, with higher temperatures resulting in a marginally inflated first core. Figure 2.3 shows the effect of the initial temperature of the cloud on the radius of the first core. The data points correspond to snapshots throughout the simulation, indicating the temporal evolution of the radius of the first core. The markers illustrate the different starting temperatures used.

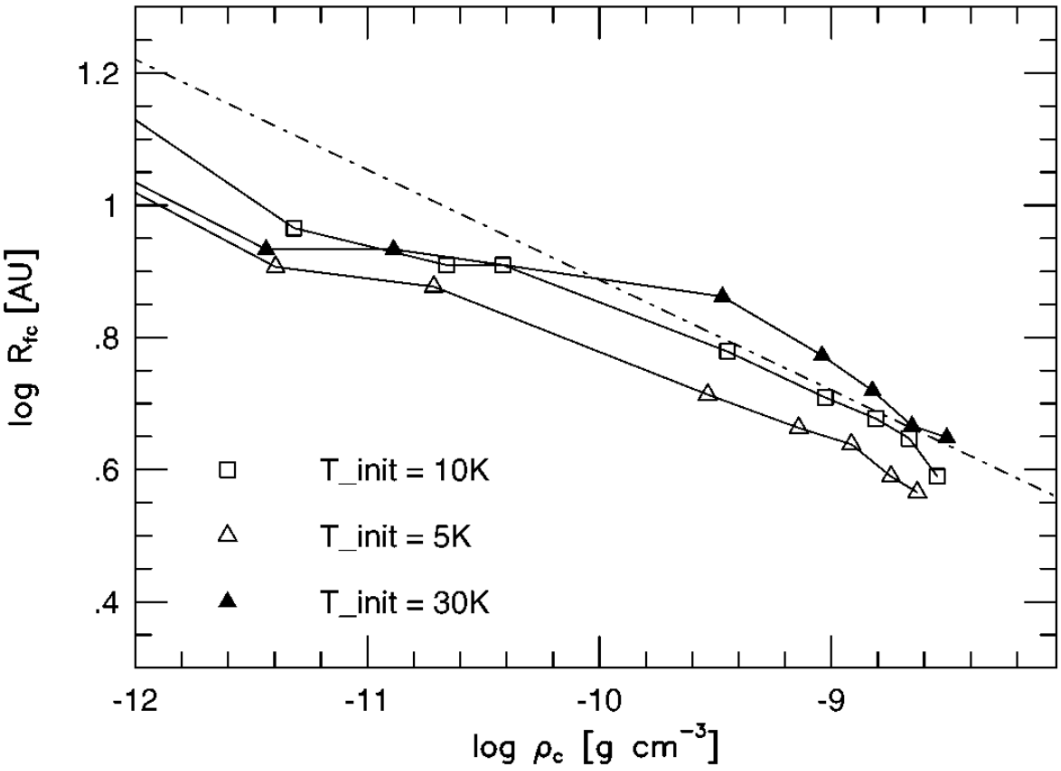

Figure 2.3: The radius of the first core at various stages of evolution as a function of central density. Each of the markers corresponds to a different initial temperature of the cloud. Taken from Masunaga, Miyama & Inutsuka (1998)

2.4.2 Dependence on Cloud Mass

The radius of the first core is largely independent of the initial mass of the cloud (see Figure 2.4 which shows the temporal evolution of the cloud where, as with Figure 2.3, the marker style indicates the initial conditions.). During the initial phase of isothermal evolution, the density distribution develops into a centrally peaked profile and, as outlined in § 2.4.1, the change in the evolution from isothermal into adiabatic is determined by the initial temperature and the opacity. Bhandare et al. (2018) do note that in the high mass regime (40 - 100 $M_\odot$), there is little to no evidence of first core formation, with the evolution proceeding directly to the second phase of

collapse. This is due to the gravitational force being overwhelmingly dominant and preventing the formation of the initial shock front.

A more massive cloud results in a more massive second core. For a cloud of $1\,M_\odot$, the mass of the second core is of order of a few to a few tens of Jupiter masses. For a cloud of $8\,M_\odot$, the mass of the second core increases beyond $100\,M_J$ (Bhandare et al., 2020). Furthermore, an increasing cloud mass results in a larger second core radius. Bhandare et al. (2020) find that the second core radius increases from $R_{sc} = 0.253\,AU$ for a $1\,M_\odot$ cloud to $R_{sc} = 0.613\,AU$ for an $8\,M_\odot$ cloud.

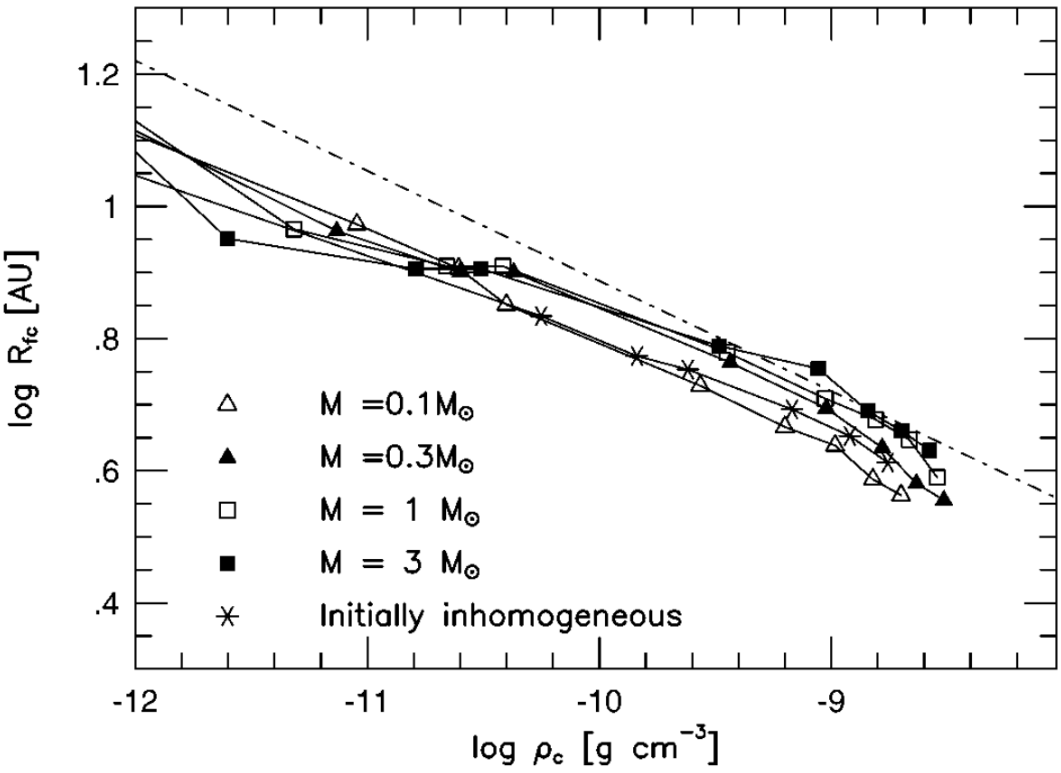

Figure 2.4: The radius of the first core at various stages of evolution as a function of central density. Each of the markers correspond to a different initial temperature of the cloud. Taken from Masunaga, Miyama & Inutsuka (1998)

2.4.3 Dependence on Opacity

At high optical depth, the ability of the cloud to cool by radiative emission is lessened and so the temperature of the cloud at a given density is higher than in the case of low optical depth. Additionally $\rho_{\tau\approx1}$ is lower and so the formation of the first core occurs earlier in the evolution and a more massive first core forms with a larger radius. In Figure 2.5, model b) shows the effect of a higher opacity on the radius of the first core. A lower opacity (model c in Figure 2.5) causes the temperature at the centre of the cloud to increase more slowly. This lengthens the stage of the first collapse and results in a first core with a reduced mass and radius (Masunaga, Miyama & Inutsuka, 1998; Mercer & Stamatellos, 2020). Figure 2.5 follows the same standard as Figures 2.3 and 2.4 for the marker style.

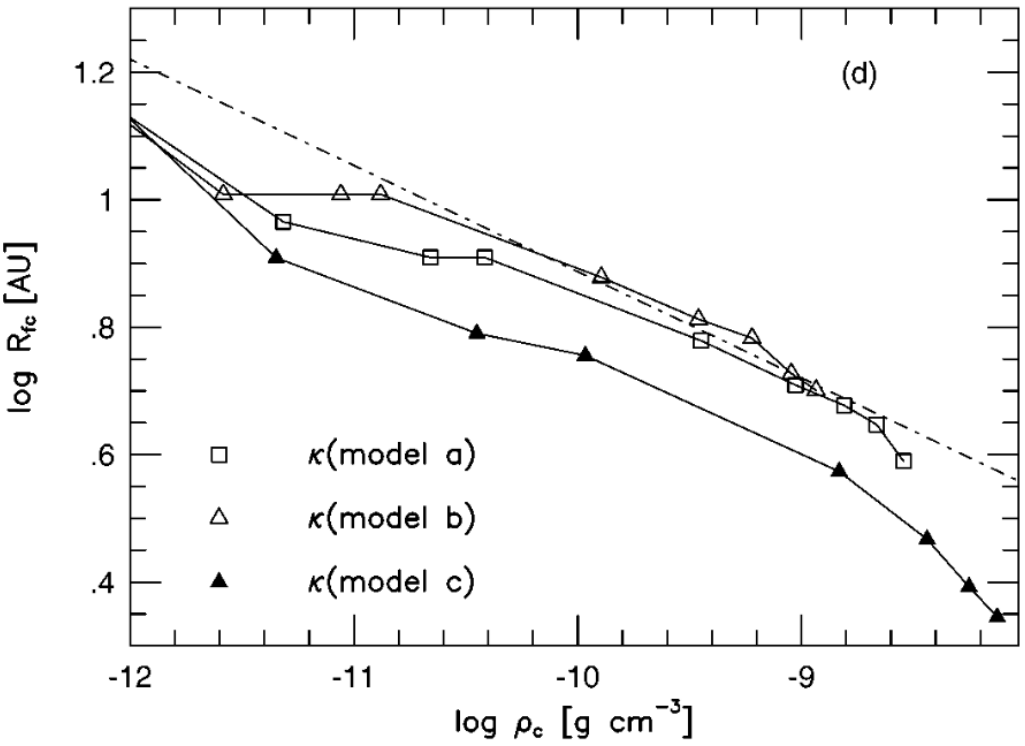

Figure 2.5: The radius of the first core at various stages of evolution as a function of central density. Each of the markers corresponds to a different initial temperature of the cloud. Taken from Masunaga, Miyama & Inutsuka (1998)

2.5 Core Collapse in the Context of Planet Formation

A sufficiently massive disc with a short enough cooling time is gravitationally unstable and has the potential to fragment and form high density clumps of gas (see discussion in §1.5). These fragments have masses from a few to tens of Jupiter masses and undergo an evolution that is similar to that of a collapsing molecular cloud, as detailed in the preceding sections. Figure 2.6 illustrates the evolution of a fiducial fragment formed in a gravitationally unstable disc around an M dwarf (Mercer & Stamatellos, 2020). The fragment, similar to the case of a solar-mass cloud, undergoes a first collapse to the first hydrostatic core and a subsequent second collapse to form the second hydrostatic core, which in this case is a protoplanet instead of a protostar. Figure 2.7 shows the evolution of the temperature and density at the centre of fragments forming in an gravitationally unstable disc (Stamatellos & Whitworth, 2009). The solid red line indicates the evolution of a solar-mass cloud.

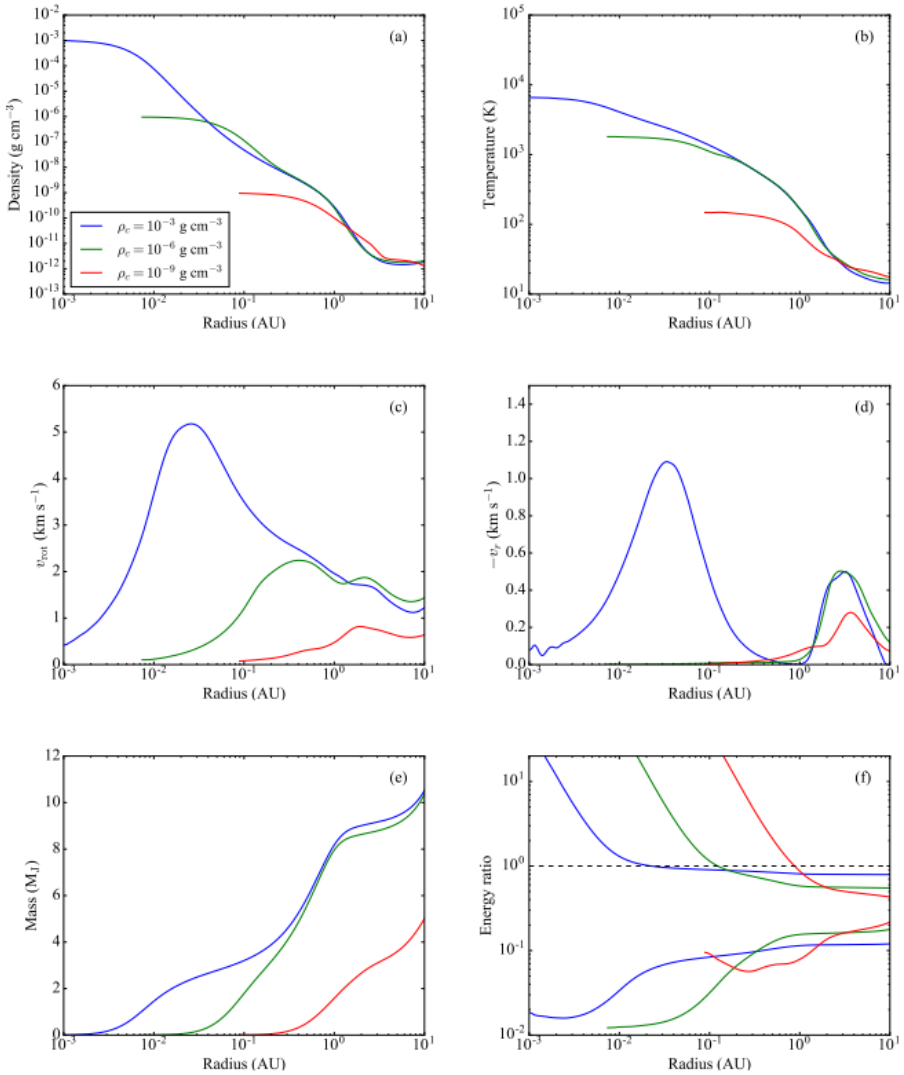

Figure 2.6: The properties of a fiducial fragment at three stages of its evolution. Each of the coloured lines represents a different central density. Panels a) and b) show the averaged density and temperature at the centre of the fragment. Panels c) and d) show the rotational and infall velocities of the gas in the clump, the locations of the first and second cores are indicated by the peaks in the infall velocity. Panel e) shows the mass of the fragment up to a given radius. Panel (f) shows the ratios between the rotational, gravitational and thermal energies. Taken from Mercer & Stamatellos (2020)

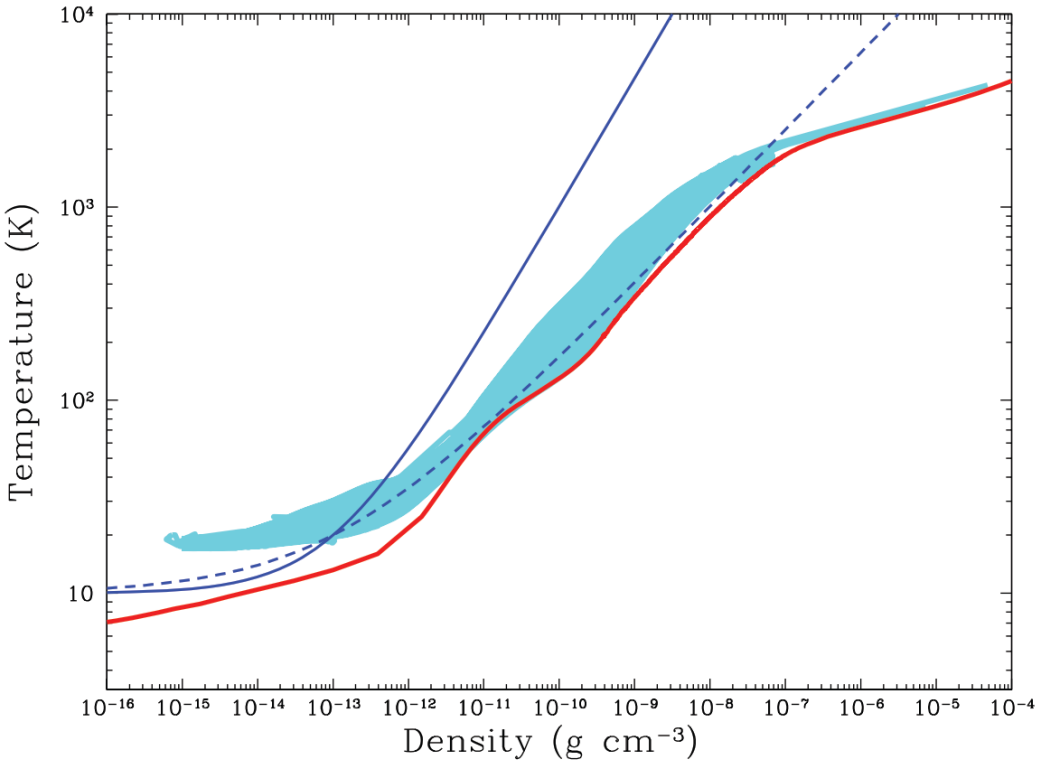

Figure 2.7: The evolution of the density and temperature at the centre of fragments that form in a gravitationally unstable disc (cyan region). The solid red line shows the evolution of a collapsing solar-mass cloud using the diffusion approximation. The blue lines are reference lines corresponding to a barotropic EOS with $\gamma = 7/5$ (dashed) and $\gamma = 5/3$ (solid). Taken from Stamatellos & Whitworth (2009).

Fragments that form at smaller distances from the host star do so earlier than those forming farther away. Their evolution occurs on a relatively long timescale of ≈3-4 kyr with the first core forming after a few thousand years. The fragments that form at later times in the outer disc however evolve to the point of first core formation much more rapidly ($\approx 20-100$ yr). This is due to interactions with spiral arms and mergers with existing fragments in the disc (Stamatellos & Whitworth, 2009). Inner disc fragments evolve from the first core to the second core more rapidly than those in the outer disc owing to there being more mass in the inner disc than

in the outer regions.

Mercer & Stamatellos (2020) identify two types of protoplanets formed by disc instability: Type I protoplanets which undergo the second collapse and reach temperatures of 2000 K and densities of $10^{-3}\mathrm{g\,cm^{-3}}$ at their centres, and Type II protoplanets which do not reach central densities of $10^{-3}\mathrm{g\,cm^{-3}}$. Figures 2.8 and 2.9 shows the masses and radii of the first and second cores formed in simulations by Mercer & Stamatellos (2020).

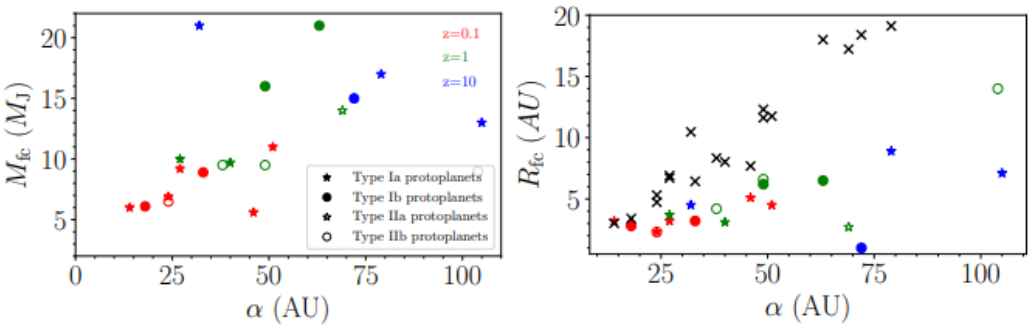

Figure 2.8: The masses (left panel) and radii (right panel) of the first cores formed in simulations by Mercer & Stamatellos (2020). The filled markers indicate type I protoplanets the empty markers correspond to type II protoplanets. The shape of the marker indicate the sub-classes of these protoplanet types, with stars and circles corresponding to sub-classes a and b respectively. The colour of the marker illustrates the factor z the authors use to control the opacity. The crosses correspond to the Hill radius of each fragment. Taken from Mercer & Stamatellos (2020).

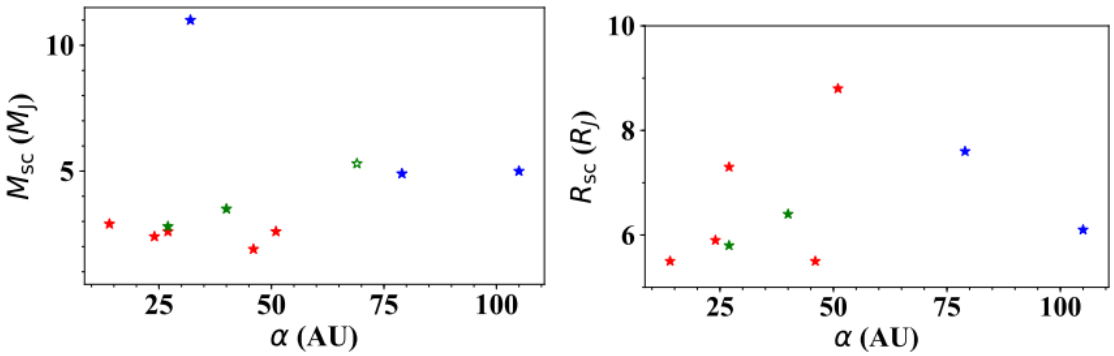

Figure 2.9: The masses (left panel) and radii (right panel) of the second cores formed in simulations by Mercer & Stamatellos (2020). The colours and symbols are the same as that in Figure 2.8. Taken from Mercer & Stamatellos (2020).

The majority of fragments that form by gravitational fragmentation evolve to become Type I protoplanets with central temperatures of 6,000 - 12,000 K and central densities of $10^{-3}\mathrm{g\,cm^{-3}}$. Type II protoplanets may evolve to Type I protoplanets or disperse due to tidal interactions with the disc. Mercer & Stamatellos (2020) find that first core masses are super-Jovian (see Figure 2.8) with radii of a few AU. There is also evidence of a dependence on the metalicity; both the first core mass and radius are higher for higher metalicity though there is significant spread shown by the different colour markers in Figures 2.8 and 2.9. A change in metalicity can be modelled by modifying the value of opacity. In optically thick regions, the ability of the protoplanet to cool is lessened and so the mass and radius of the first core increases.

2.6 Summary

In this chapter I have discussed the collapse of a molecular cloud and the formation of the first and second hydrostatic cores. I have provided context for how this process occurs in the formation of giant planets. The fragments that form in gravitationally

unstable discs, which may go on to form protoplanets, undergo the same phases of collapse (Mercer & Stamatellos, 2020; Stamatellos & Whitworth, 2009). In this thesis, I will analyse how the disc thermodynamics effects the final properties of fragments such as the masses and radii of the first and second cores.

Chapter 3

Numerical Hydrodynamics

3.1 Smoothed Particle Hydrodynamics

Modelling the behaviour of astrophysical fluids requires the solution of the fluid equations. For this we appeal to the higher order principles of the conservation of mass, momentum and energy. Two main schools of thought exist on how to achieve this computationally: Eulerian methods, those which model the flow of the fluid through a stationary reference frame, and Lagrangian methods, those which model the flow of a fluid via the means of a discrete set of particles that move with the flow. Smoothed Particle Hydrodynamics, herein SPH, is an example of the latter developed independently by Lucy (1977) and Gingold & Monaghan (1977). SPH is particularly useful for modelling astrophysical flows with no fixed boundary and problems where a high degree of spatial resolution is required. The advantage of SPH over Eulerian grid based codes is its inherent adaptive resolution; areas with low density are represented by fewer particles and those with higher densities with more particles. In this way, computational expense is spared.

The value of some field f at a point $\mathbf{r}$ is given by the convolution of the field at

an arbitrary point $\mathbf{r}'$ with the Dirac δ-function,

$$f(\mathbf{r}) = \int_V f(\mathbf{r}')\,\delta(\mathbf{r}-\mathbf{r}')\,d\mathbf{r}'. \tag{3.1}$$

To model a continuous fluid with a discrete set of particles the δ-function is broadened i.e. smoothed out, over a characteristic length scale h, referred to as the smoothing length, into a kernel function $W(\mathbf{r}-\mathbf{r}', h)$. In the limit of small smoothing lengths, the kernel function is equal to the Dirac δ-function, i.e.

$$\lim_{h\to 0} W(\mathbf{r}-\mathbf{r}', h) = \delta(\mathbf{r}). \tag{3.2}$$

The volume integral in Equation 3.1 is discretized by calculating the sum over all particles of mass m_i, performing the substitution

$$\int_V \to \sum_i \frac{m_i}{\rho_i}, \tag{3.3}$$

thereby representing the volume integral as a sum of individual elements of mass m_i and density ρ_i. This gives the SPH estimate for the field f at the position of particle i as

$$f(\mathbf{r}_\mathrm{i}) \approx \sum_\mathrm{j} \frac{m_\mathrm{j}}{\rho_\mathrm{j}}\, f(\mathbf{r}_\mathrm{j})\, W_\mathrm{ij}, \tag{3.4}$$

using the compact notation $W_{ij} = W(\mathbf{r_i}-\mathbf{r_j}, h)$. The SPH estimator in Equation 3.4 trivially provides the SPH continuity equation where the field $f(\mathbf{r}_j)$ is equal to $\rho(\mathbf{r}_j)$ and so

$$\rho(\mathbf{r}_\mathrm{i}) = \sum_\mathrm{j} \frac{m_\mathrm{j}}{\rho_\mathrm{j}}\, \rho(\mathbf{r}_\mathrm{j})\, W_\mathrm{ij} = \sum_\mathrm{j} m_\mathrm{j}\, W_\mathrm{ij}. \tag{3.5}$$

To model a fluid using this formalism, an SPH estimate for the momentum and energy equations is required. Lodato & Cossins (2011) derive the equations of motion and energy for the SPH framework by using the Lagrangian formalism and arrive at

$$\frac{d\mathbf{v}_\mathrm{i}}{dt} = -\sum_\mathrm{j} \left[m_\mathrm{j} \left(\frac{P_\mathrm{i}}{\rho_\mathrm{i}^2} + \frac{P_\mathrm{j}}{\rho_\mathrm{j}^2} \right) \nabla_\mathrm{i} W_\mathrm{ij} + \Pi_{ij} \right] + \left.\frac{d\mathbf{v_i}}{dt}\right|_\mathrm{grav}, \tag{3.6}$$

and

$$\frac{du_i}{dt} = \frac{P_i}{\rho_i^2} \sum_j m_j \, \mathbf{v}_{ij} \cdot \nabla W_{ij} + \Pi_{ij}, \tag{3.7}$$

respectively, where the $\frac{d\mathbf{v_i}}{dt}\big|_{\text{grav}}$ and Π_{ij} terms correspond to the effect of self gravity and artificial viscosity. Each of these terms will be discussed separately in sections 3.3 and 3.4. respectively.

3.2 The smoothing kernel

The purpose of the smoothing kernel is to broaden a δ-function over the smoothing length in order to discretize the continuous fluid. To avoid unnecessary computational cost, a kernel with compact support, where its values are exactly zero for $|\mathbf{r}| > 2h$, is chosen. This truncation avoids the calculation of contributions from all particles in the simulation, as would be the case for a Gaussian kernel where the values tend asymptotically to zero, resulting in a time complexity for the calculation of $\mathcal{O}(N^2)$. In essence, this type of kernel means that only contributions from a selected number of neighbouring particles N_{neigh}, are calculated for any particle in the simulation, drastically reducing the computational expense of the calculation to a time complexity of $\mathcal{O}(N_{neigh}N)$. Several kernel functions exist to facilitate the smoothing of the δ-function. A particularly common one is the M_4 cubic spline (Schoenberg, 1946) given by

$$W_{ij} = \frac{\sigma}{h^d} \begin{cases} \frac{1}{4}(2-q)^3 - (1-q)^3, & 0 \leq q < 1; \\ \frac{1}{4}(2-q)^3, & 1 \leq q < 2 \\ 0. & q \geq 2, \end{cases} \tag{3.8}$$

where $q = |\mathbf{r_i} - \mathbf{r_j}|/h$. The normalisation constant σ is dependant on the number of dimensions, d such that $\sigma = [2/3, 7/10\pi, 1/\pi]$ for d = [1,2,3] respectively. The M4 cubic spline kernel with its first and second derivatives are show in Figure 3.1

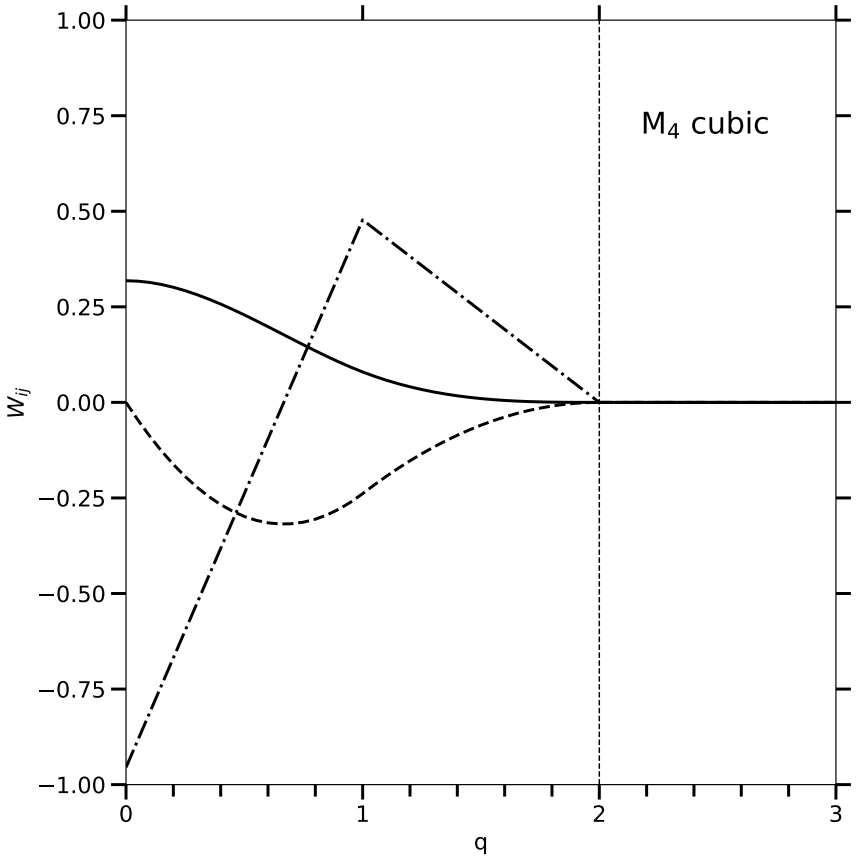

Figure 3.1: The M4 kernel (solid line) is chosen for its compact support. The vertical dashed line in the figure indicates the limit beyond which particle contributions are neglected.The kernel's first and second derivative are plotted in the dashed and dash-dot lines respectively.

3.2.1 Choice of smoothing length and adaptive resolution

One option for defining the smoothing length h is to fix $N_{\rm neigh}$ to ensure each kernel is sufficiently sampled, this is the method utilised in early forms of SPH (e.g. Gingold & Monaghan (1977). In 3-dimensions it is generally agreed that for a kernel to be sufficiently numerically sampled $N_{\rm neigh}$ is 40-60. The downside to a spatially constant value of the smoothing length is that it can introduce noise and uncertainty for physical problems with large density ranges. A particle moving from a high density

region, where the smoothing length is small, to a lower density region would lead to an under-sampled kernel and lower resolution. Rather than set a constant value of h by means of a number of neighbours, an alternate method is to specify the smoothing length function of the local number density such that

$$h = h_{\rm fact}\left(\frac{m_{\rm i}}{\rho_{\rm i}}\right)^{1/3}. \tag{3.9}$$

Here, $h_{\rm fact}$ is a factor of proportionality describing the relationship between smoothing length and the local particle spacing. The value of $h_{\rm fact}$ is linked to the mean number of neighbours via

$$\bar{N}_{\rm neigh} = \frac{4}{3}\pi(R_{\rm kern}h_{\rm fact})^3. \tag{3.10}$$

Price (2012) discusses at length the issues related to attempting to increase spatial resolution by increasing the radius of the kernel $R_{\rm kern}$, i.e. increasing $N_{\rm neigh}$. "Stretching" the kernel in this way results in a loss of resolution by simultaneously increasing the smoothing length (via Equation (3.10)). It also leads to the onset of the pairing instability wherein, due to the forces between neighbouring particles inside $\approx 2/3\,q$, the particles drift toward one another and form a pair. This is due to the negative maximum in the kernel gradient (dashed line in Figure 3.1) (Price, 2012). The M4 cubic spline (Equation 3.8) is generally stable against the pairing instability for $1.0 < h_{fact} < 1.2$.

To appropriately evaluate the momentum and energy equations, they must be corrected for the temporal variability in the smoothing length, given by the time derivative of Equation 3.9 giving, for a system in 3 dimensions, as

$$\frac{dh_i}{dt} = \frac{-h_i}{3\rho_i}\frac{d\rho_i}{dt}. \tag{3.11}$$

By taking the Lagrangian derivative of Equation 3.5, one obtains the discrete form of the continuity equation in SP

$$\frac{d\rho_i}{dt} = \frac{1}{\Omega_i}\sum_j m_j(\mathbf{v}_i - \mathbf{v}_j)\cdot\nabla_i W_{ij}(h_i), \tag{3.12}$$

where the Ω_i factor corrects for the variability in the smoothing length and is given by

$$\Omega_i \equiv 1 - \frac{\partial h_i}{\partial \rho_i} \sum_j m_j \frac{\partial W_{ij}(h_i)}{\partial h_i}. \tag{3.13}$$

Springel & Hernquist (2002) give the corrected equations of motion to be

$$\frac{d\mathbf{v}_\mathrm{i}}{dt} = -\sum_\mathrm{j} \left[m_\mathrm{j} \left(\frac{P_\mathrm{i}}{\Omega_i \rho_\mathrm{i}^2} + \frac{P_\mathrm{j}}{\Omega_j \rho_\mathrm{j}^2} \right) \nabla_\mathrm{i} W_\mathrm{ij} + \Pi_{ij} \right] + \left. \frac{d\mathbf{v_i}}{dt} \right|_\mathrm{grav}, \tag{3.14}$$

and

$$\frac{du_i}{dt} = \frac{P_i}{\Omega_i \rho_i^2} \sum_j m_j \, \mathbf{v}_{ij} \cdot \nabla W_{ij} + \Pi_{ij}, \tag{3.15}$$

3.3 Self Gravity

Self gravity is implemented in SPH by solving Poisson's equation,

$$\nabla^2 \Phi = 4\pi G \rho(\mathbf{r}), \tag{3.16}$$

where Φ is the gravitational potential and ρ is the density of the fluid, a continuous quantity. The acceleration then is given by

$$\left. \frac{d\mathbf{v_i}}{dt} \right|_\mathrm{grav} = -\nabla \Phi \tag{3.17}$$

The appendices of Price & Monaghan (2007) provide an extensive discussion of the implementation of self gravity in the fluid equations and introduce two additional softening functions for the gravitational potential ϕ and the gravitational force ϕ'. In the case where the M4 cubic spline is used for density smoothing, ϕ and $\phi\prime$ are given by

$$\phi_{ij}(\mathbf{r}_i - \mathbf{r}_j, h_i) = \frac{1}{h_i} \begin{cases} \frac{2}{3}q^2 - \frac{3}{10}q^4 + \frac{1}{10}q^5 - \frac{7}{5}, & 0 \le q < 1; \\ \frac{4}{3}q^2 - q^3 + \frac{3}{10}q^4 - \frac{1}{30}q^5 - \frac{8}{5} + \frac{1}{15}q, & 1 \le q < 2 \\ -q^{-1}. & q \ge 2, \end{cases} \tag{3.18}$$

$$\phi'_{ij}(\mathbf{r}_i - \mathbf{r}_j, h_i) = \frac{1}{h_i^2} \begin{cases} \frac{4}{3}q - \frac{6}{5}q^3 + \frac{1}{2}q^4, & 0 \leq q < 1; \\ \frac{3}{3}q - 3q^2 + \frac{6}{5}q^3 - \frac{1}{6}q^4 - \frac{1}{15}q^{-2}, & 1 \leq q < 2 \\ q^{-2}. & q \geq 2. \end{cases} \tag{3.19}$$

Price & Monaghan (2007) show how Equation 3.16 is solved for a spatially variable smoothing length and, using the general formulation as in Dehnen (2001), present the smoothed gravitational potential as

$$\Phi(\mathbf{r}) = -G \sum_{i=j}^{N} m_i \phi(|\mathbf{r}_i - \mathbf{r}_j|, h), \tag{3.20}$$

where ϕ is the softening kernel and G is the gravitational constant. For the case with variable smoothing lengths, the average of kernels in Equations 3.18 and 3.19 is required for the conservation of energy, i.e.

$$\Phi(\mathbf{r}) = -G \sum_{i=1}^{N} m_i \left[\frac{\phi_{ij}(h_i) + \phi_{ij}(h_j)}{2} \right], \tag{3.21}$$

Price & Monaghan (2007) show the Lagrangian formulation for the solution to Equation 3.17 as

$$\left. \frac{d\mathbf{v_i}}{dt} \right|_{\text{grav}} = -\nabla\Phi \tag{3.22}$$

$$= -G \sum_{i=1} m_i \left[\frac{\phi_{ij}(h_i) + \phi_{ij}(h_j)}{2} \right] \tag{3.23}$$

$$- \frac{G}{2} \sum_{i=1} m_i \left[\frac{\zeta_i}{\Omega_i} \nabla_i W_{ij}(h_i) + \frac{\zeta_i}{\Omega_i} \nabla_i W_{ij}(h_j) \right], \tag{3.24}$$

where the Ω and ζ terms are corrections necessary for the conservation of energy. Ω is given by Equation 3.13 and ζ by

$$\zeta_i = \frac{\partial h_i}{\partial \rho_i} \sum_j m_j \frac{\partial \phi_{ij}(h_i)}{\partial h_i}. \tag{3.25}$$

3.4 Artificial Viscosity

Thus far it has been assumed that the fluid has been non-dissipative, that is that there has been no heating due to viscous forces. Observing the fluid equations in this way leads non-linear behaviour. If a fluid can be considered collisionless, this is the correct interpretation. An example of this would be modelling large dust grains in debris discs. If however the fluid elements are allowed to physically collide, as is the case with molecules in a gas, then the SPH equations must be altered to allow for dissipation and energy loss. In SPH, this is done by means of an artificial viscosity. Viscosity is fundamental in physical modelling of astrophysical fluids, particularly those in accretion discs as it facilitates angular momentum transport radially outwards which allows for the inward flow of material and accretion onto the central host star. In realistic fluids, collisions between particles result in an increase in heat and this irreversible process implies an increase in entropy. This means that convergent flows introduce discontinuities in entropy, pressure, density and velocity at the location of the shock on length scales far smaller than the smoothing length. To correctly model this in SPH, the shock is broadened over a small number of smoothing lengths and discontinuities are dissipated with an artificial viscosity term in the momentum and energy equations (3.6 and 3.7 respectively) which, with this modification, become

$$\frac{dv_{\mathrm{i}}}{dt} = -\sum_{\mathrm{j}} m_{\mathrm{j}} \left(\frac{P_{\mathrm{j}}}{\rho_{\mathrm{j}}^2} + \frac{P_{\mathrm{i}}}{\rho_{\mathrm{i}}^2} + \Pi_{\mathrm{ij}} \right) \nabla_{\mathrm{i}} W_{\mathrm{ij}}, \tag{3.26}$$

$$\frac{du_{\mathrm{i}}}{dt} = \frac{1}{2} \sum_{\mathrm{j}} m_{\mathrm{j}} \left(\frac{P_{\mathrm{j}}}{\rho_{\mathrm{j}}^2} + \frac{P_{\mathrm{i}}}{\rho_{\mathrm{i}}^2} + \Pi_{\mathrm{ij}} \right) \mathbf{v}_{\mathrm{ij}} \cdot \nabla_{\mathrm{i}} W_{\mathrm{ij}}. \tag{3.27}$$

The Π term in equations 3.26 and 3.27 is the artificial pressure used to broaden the shock over a number of smoothing lengths. Monaghan & Gingold (1983) give Π as

$$\Pi_{ij} = \frac{-\alpha \bar{c}_{\mathrm{s,ij}} \mu_{\mathrm{ij}} + \beta \mu_{\mathrm{ij}}^2}{\bar{\rho}_{\mathrm{ij}}}, \tag{3.28}$$

where α and β are dimensionless parameters, $\bar{\rho}_{\rm ij}$ is the average density $\bar{\rho}_{\rm ij} = \frac{1}{2}(\rho_{\rm i}+\rho_{\rm j})$ and $\bar{c}_{\rm s,ij}$ is the average isothermal sound speed $\bar{c}_{\rm s,ij} = \frac{1}{2}(c_{\rm s,i} + c_{\rm s,j})$. The $\mu_{\rm ij}$ term is given by

$$\mu_{\rm ij} = \begin{cases} \frac{\bar{h}_{\rm ij}\mathbf{v}_{\rm ij}\cdot\mathbf{r}_{\rm ij}}{|\mathbf{r}_{\rm ij}|^2+\epsilon\bar{h}_{\rm ij}^2}, & \text{if } \mathbf{v}_i \cdot \mathbf{r}_{ij} < 0 \\ 0 & \text{Otherwise} \end{cases} \tag{3.29}$$

where h is a characteristic smoothing length and the shorthand $A_{\rm ij} = A_{\rm i} - A_{\rm j}$ is used in the case of the velocity $\mathbf{v}$ and the position $\mathbf{r}$. The over-bar is used to indicate that the quantity takes on the mean value for particles a and b. The factor ϵ where $\epsilon \ll 1$ is used to avoid a singularity in the limit where $\mathbf{r}_{\rm ij} \longrightarrow 0$. From Equation 3.29 we can see that for receding pairs $\Pi_{ij} = 0$, therefore artificial viscosity only effects compressive flows (Cullen & Dehnen, 2010). In practice, this artificial viscosity produces nonphysical dissipation away from the shock regions causing, in the case of a protoplanetary disc, unrealistic angular momentum transport.

3.4.1 Morris and Monaghan formulation

This model of artificial viscosity is modified in the method of Morris & Monaghan (1997) which allows for a continually adaptive value of $\alpha_{\rm SPH}$ for each particle. This leads to the modification of $\alpha_{\rm SPH}$ to instead take the average value of α for two particles i and j such that $\bar{\alpha}_{\rm SPH,ij} = (\alpha_{\rm SPH,i} + \alpha_{\rm SPH,j})/2$. This method has a lower limit of $\alpha = 0.1$ for all particles. Although the Morris & Monaghan (1997) method constitutes a significant improvement over the standard treatment of viscosity in SPH, any value of $\alpha > 0$ causes nonphysical angular momentum transport and dissipation.

3.4.2 The Balsara switch

One 'switch' to alleviate nonphysical angular momentum transport as a result of artificial viscosity in SPH was developed by Balsara (1995). The Balsara switch acts to reduce the artificial viscosity away from shocks by a factor $\bar{f}_{\rm ij}$ given by $\bar{f}_{\rm ij} = (\bar{f}_{\rm i} + \bar{f}_{\rm i})/2$ where

$$f_{\rm i} = \frac{|\nabla \cdot \mathbf{v}_{\rm i}|}{|\nabla \cdot \mathbf{v}_{\rm i}| + |\nabla \times \mathbf{v}_{\rm i}|}. \tag{3.30}$$

$\mathbf{v}_{\rm i}$ is the velocity of particle a (Balsara, 1995). This factor multiplies the artificial pressure $\Pi_{\rm ij}$, in the energy and momentum equations such that

$$\frac{du_{\rm i}}{dt} = \frac{1}{2}\sum_{\rm i} m_{\rm i}\left(\frac{P_{\rm i}}{\rho_{\rm i}^2} + \frac{P_{\rm i}}{\rho_{\rm i}^2} + \bar{f}_{ij}\Pi_{\rm ij}\right)\mathbf{v}_{\rm ij}\cdot\nabla_{\rm i}W_{\rm ij}, \tag{3.31}$$

$$\frac{dv_{\rm i}}{dt} = -\sum_{\rm i} m_{\rm i}\left(\frac{P_{\rm i}}{\rho_{\rm i}^2} + \frac{P_{\rm i}}{\rho_{\rm i}^2} + \bar{f}_{ij}\Pi_{\rm ij}\right)\nabla_{\rm i}W_{\rm ij}. \tag{3.32}$$

where P is pressure, ρ is density, m is mass and $\mathbf{v}_{\rm ij}$ is equal to the velocity difference $\mathbf{v}_{\rm i} - \mathbf{v}_{\rm i}$. $W_{\rm ij}$ is the SPH kernel function where $W_{\rm ij} = W(\mathbf{r}_{\rm i} - \mathbf{r}_{\rm i}, h)$.

In a Keplerian disc, the following are true:

$$|\nabla \times \mathbf{v_i}| = \left(\frac{GM}{4r^3}\right)^{1/2}, \tag{3.33}$$

$$|\nabla \cdot \mathbf{v_i}| = 0 \tag{3.34}$$

Convergent flow in the disc causes an increase in $|\nabla \cdot \mathbf{v}_{\rm i}|$ and a subsequent increase in $\bar{f}_{\rm i}$ up to the limit of unity when $|\nabla \cdot \mathbf{v}_{\rm i}| \gg |\nabla \times \mathbf{v}_{\rm i}|$. This means that when the vorticity $|\nabla \times \mathbf{v}_{\rm i}|$ dominates over the convergence i.e. in areas of stable Keplerian rotation, the artificial viscosity is in effect 'switched off'. The results from Cartwright & Stamatellos (2010) indicate that this method of controlling artificial viscosity in accretion discs suffers from nonphysically large values of $f_{\rm i}$. The same work finds that, when using $|\nabla \cdot \mathbf{v}_{\rm i}|$ as an indicator of convergence, particles form alignments in the leading direction. This causes a spurious increase in the value of $f_{\rm i}$ and reduces the effectiveness of the Balsara switch in 'turning off' artificial viscosity away from shocks.

3.4.3 The Cullen and Dehnen 2010 (CD10) switch

The Cullen & Dehnen (2010) switch (CD10 switch) for controlling artificial viscosity uses the total time derivative of the velocity divergence where a negative value of $\dot{\nabla} \cdot \mathbf{v}$ indicates a region where the convergence of the flow is steepened which is indicative of a pre-shock region while a positive value implies a post-shock region. The CD10 switch uses a limiter with the same functional form of Equation (3.30) but with particular attention paid to limiting false detections of convergent flows. The limiter for the CD10 switch takes the form

$$\xi_{\rm i} = \frac{|2(1-R_{\rm i})^4 \nabla \cdot \mathbf{v}_{\rm i}|^2}{|2(1-R_{\rm i})^4 \nabla \cdot \mathbf{v}_{\rm i}|^2 + |\nabla \times \mathbf{v}_{\rm i}|^2}, \tag{3.35}$$

$$R_{\rm i} = \frac{1}{\hat{\rho}_{\rm i}} \sum_b \text{sign}(\nabla \cdot \mathbf{v}_{\rm i}) m_{\rm i} W_{\rm ij}. \tag{3.36}$$

Here, $\hat{\rho}_{\rm i}$ is the local estimate of the density at the position of particle a given by the kernel estimator. $R_{\rm i}$ indicates the presence of shocks using a sign function that takes a value of -1 when $\nabla \cdot \mathbf{v}_{\rm i} < 0$

$$\text{sign}(\nabla \cdot \mathbf{v}_{\rm i}) = \begin{cases} -1 & \text{if } \nabla \cdot \mathbf{v}_{refrmi} < 0 \\ 0 & \text{if } \nabla \cdot \mathbf{v}_{\rm i} = 0 \\ 1 & \text{if } \nabla \cdot \mathbf{v}_{\rm i} > 0. \end{cases} \tag{3.37}$$

This means that in the presence of a shock, $R_{\rm i} \approx -1$. This detection of shocks and improved limiter gives a much improved prescription of artificial viscosity in SPH which avoids false detections of shocks in complicated flows.

Cullen & Dehnen (2010) apply this method of controlling artificial viscosity in the context of a 2D Keplerian disc. The results for traditional SPH, the Morris & Monaghan (1997) method and the Balsara switch all show the disc breaks apart due to the viscous instability within a few inner orbital periods with only the CD10 method maintaining equilibrium after 5 periods.

3.5 Artificial Viscosity in Discs

The standard prescription of viscosity in discs given by Shakura & Sunyaev (1973) as

$$\nu = \alpha_{ss} c_s H, \tag{3.38}$$

where c_s is the sound speed, H is the disc scale height and α_{ss} is a dimensionless parameter that describes the efficiency of angular momentum transport in the disc. A practical method of recreating this effective viscosity in simulations of discs is to modify the shock viscosity term (equations. 3.28 and 3.29) to allow for the effect of artificial viscosity to effect both converging and receding flows. Artymowicz & Lubow (1994) justifies this modification as it preserves the property of the Navier-Stokes fluid equations wherein the viscosity remains nonzero for converging and expanding flows. With this alteration and adopting a constant value for α (Lodato & Price, 2010), the value of the effective viscosity α_{ss} simulated by an artificial viscosity α is given by

$$\alpha_{ss} \approx \frac{1}{10} \alpha \frac{h}{H}. \tag{3.39}$$

Too low a value for α can lead to non-physical dissipation and so the lowest meaningful value is $\alpha = 0.1$. Equation 3.39 shows that the minimum representable value of an effective viscosity is resolution limited i.e. dependant on the mean smoothing length h. Also shown by Equation 3.39, in order to obtain a constant effective viscosity, one must uniformly resolve the scale height of the disc.

3.6 Time Integration

The equations of motion are evolved temporally in accordance to a chosen time integration scheme. These methods advance the calculation in time by recalculating a particle's position and velocity after some unit of time has passed Δt.

A common choice for this is the Leapfrog method in which the velocity and position data are asynchronous i.e. the velocity $\mathbf{v}$, is calculated at half-timesteps, $\frac{1}{2}\Delta t$:

$$\mathbf{v}^{n+\frac{1}{2}} = \mathbf{v}^n + \frac{1}{2}\Delta t\,\mathbf{a}^n, \tag{3.40}$$

and so

$$\mathbf{v}^{n+1} = \mathbf{v}^{n+\frac{1}{2}} + \frac{1}{2}\Delta t\,\mathbf{a}^{n+1} \equiv \mathbf{v}^n + \frac{1}{2}(\mathbf{a}^n + \mathbf{a}^{n+1})\Delta t. \tag{3.41}$$

The position $\mathbf{r}$, of the particle at the next timestep is given by

$$\mathbf{r}^{n+1} = \mathbf{r}^n + \mathbf{v}^n\Delta t + \frac{1}{2}\mathbf{a}^n\Delta t^2, \tag{3.42}$$

where $\Delta t \equiv t^{n+1} - t^n$ and $\mathbf{a} = \frac{d\mathbf{v}}{dt}$. The advantage of this scheme is that is it time reversible i.e. the conservation of energy, angular momentum etc. is exactly preserved. It is also computationally efficient, with the acceleration needing only to be calculated once per time step.

3.7 Summary of Equations

The fundamental equations in SPH are: The continuity equation:

$$\rho(\mathbf{r}_\mathrm{i}) = \sum_\mathrm{j} \frac{m_\mathrm{j}}{\rho_\mathrm{j}}\,\rho(\mathbf{r}_\mathrm{j})\,W_\mathrm{ij} = \sum_\mathrm{j} m_\mathrm{j}\,W_\mathrm{ij}. \tag{3.43}$$

the momentum equation

$$\frac{dv_\mathrm{i}}{dt} = -\sum_\mathrm{j} m_\mathrm{j}\left(\frac{P_\mathrm{j}}{\rho_\mathrm{j}^2} + \frac{P_\mathrm{i}}{\rho_\mathrm{i}^2} + \Pi_\mathrm{ij}\right)\nabla_\mathrm{i} W_\mathrm{ij} + \left.\frac{d\mathbf{v}_i}{dt}\right|_\mathrm{grav}, \tag{3.44}$$

where the contribution from self gravity is given by

$$\left.\frac{d\mathbf{v_i}}{dt}\right|_\mathrm{grav} = -G\sum_{i=1} m_i\left[\frac{\phi_{ij}(h_i) + \phi_{ij}(h_j)}{2}\right] \tag{3.45}$$

$$-\frac{G}{2}\sum_{i=1} m_i\left[\frac{\zeta_i}{\Omega_i}\nabla_i W_{ij}(h_i) + \frac{\zeta_i}{\Omega_i}\nabla_i W_{ij}(h_j)\right], \tag{3.46}$$

the energy equation

$$\frac{du_{\rm i}}{dt} = \frac{1}{2}\sum_{\rm j} m_{\rm j}\left(\frac{P_{\rm j}}{\rho_{\rm j}^2} + \frac{P_{\rm i}}{\rho_{\rm i}^2} + \Pi_{\rm ij}\right)\mathbf{v}_{\rm ij}\cdot\nabla_{\rm i}W_{\rm ij}, \tag{3.47}$$

where the viscosity terms are given by

$$\Pi_{ij} = \frac{-\alpha\bar{c}_{\rm s,ij}\mu_{\rm ij} + \beta\mu_{\rm ij}^2}{\bar{\rho}_{\rm ij}}, \tag{3.48}$$

$$\mu_{\rm ij} = \begin{cases} \frac{\bar{h}_{\rm ij}\mathbf{v}_{\rm ij}\cdot\mathbf{r}_{\rm ij}}{|\mathbf{r}_{\rm ij}|^2+\epsilon\bar{h}_{\rm ij}^2}, & \text{if } \mathbf{v}_i\cdot\mathbf{r}_{ij} < 0 \\ 0 & \text{Otherwise} \end{cases} \tag{3.49}$$

and the correction terms Ω and ζ required for energy conservation are given by

$$\Omega_i \equiv 1 - \frac{\partial h_i}{\partial \rho_i}\sum_j m_j \frac{\partial W_{ij}(h_i)}{\partial h_i}. \tag{3.50}$$

and

$$\zeta_i = \frac{\partial h_i}{\partial \rho_i}\sum_j m_j \frac{\partial \phi_{ij}(h_i)}{\partial h_i}. \tag{3.51}$$

3.8 Sink Particles

Hydrodynamic simulations of planet forming discs often involve the formation of many protoplanets that achieve high central densities. Following the internal processes of a protoplanet is a source of immense computational cost and, in the event that several objects form, the progress of the simulation is drastically reduced. To avoid this, some detail of the internal physics is neglected and the protoplanet is replaced by a sink particle. First introduced by Bate, Bonnell & Price (1995), sink particles are created during a simulation when the density of gas reaches some critical threshold. Following this, the sink particle only interacts with the rest of the computational domain through its gravity and, in the case where radiative feedback is present, its luminosity (Stamatellos & Ichiro Inutsuka, 2018). After the formation of a sink particle, any gas located within its accretion radius is accreted, the particles

are removed from the simulation and their mass is added to the mass of the sink. In the simulations presented here, we introduce sink particles when the central density of the fragments reaches $\rho_c = 10^{-3}\,\mathrm{g\,cm^{-3}}$.

3.9 Smoothed Particle Hydrodynamics with PHANTOM

The simulations that were run in this work were done so using PHANTOM (Price et al., 2018b). PHANTOM was developed in an effort to make available an SPH code with a focus outside of large scale structures and dark matter physics. It instead includes a wide range of physics applicable to the smaller scales of star and planet formation (Price et al., 2018b). PHANTOM has seen extensive use in the modelling of protoplanetary discs (Facchini, Juhász & Lodato, 2018; Dipierro & Laibe, 2017; Cadman et al., 2020) and was chosen for use in this work for its low memory usage and modular code design. This latter point means that it is easy to develop and incorporate new modules into the code. This feature was utilised when developing the algorithm to follow the evolution of protoplanets in the disc.

All simulations ran in this study used the following features: individual timestepping; barotropic equation of state; kd-tree implementation of self gravity; sink particles and an artificial viscosity. The default method for implementing artificial viscosity in PHANTOM differs slightly from the standard approach of limiting the effect of dissipation by way of a shock detection switch as discussed in §3.4.2 and §3.4.3. Instead, a constant viscous-α is adopted and the viscosity term is multiplied by a factor of $\frac{h}{r_{ij}}$ is applied to both approaching and receding particles, see §3.5.

PHANTOM utilises a variable smoothing length with a default value of h_{fact} in Equation 3.9 of $h_{\mathrm{fact}} = 1.2$. This is chosen to be just short of the maximum number of neighbours to maintain stability against the pairing instability as outlined in

§3.2. The effect of self gravity is split into short and long range interactions, the short range interaction is calculated via the process outlined in §3.3 and the long range interaction is computed using a kd-tree. At long range, the second term in Equation 3.24 tends to zero since $\zeta = 0$ for $q \geq R_{\rm kern}$ and the first reduces to $1/r^2$. The computational cost arising from a direct summation of all contributions results in a time complexity of $\mathcal{O}(N^2)$. In PHANTOM, a kd-tree is used to reduce this to $\mathcal{O}(NlogN)$ for the calculation of the long range interaction.

Chapter 4

Initial Conditions

I investigate the effect of thermodynamics on the formation and evolution of fragments in gravitationally unstable discs by exploring different barotropic equations of state. In this chapter I will introduce the density and temperature profiles that are used to construct the discs for this study and discuss the specifics of the barotropic equation of state used.

4.1 Disc Initial Conditions

I use discs with mass of $0.6\,\mathrm{M}_\odot$ around a host star of $0.8\,\mathrm{M}_\odot$ that extend from 10 AU - 300 AU represented by 4×10^6 particles. Each of the discs follow the same density profile while the initial SPH particle distribution varies.

4.1.1 Disc Surface Density

The surface density of the disc is given by

$$\Sigma = \Sigma_0 \left(\frac{R}{R_{\mathrm{ref}}} \right)^{-p} (1 - \sqrt{R_{\mathrm{in}}/R}), \tag{4.1}$$

where p is the power-law index, R_{in} is the inner disc radius, and R_{ref} is a reference radius set to the inner disc radius, $R_{\mathrm{ref}} = R_{\mathrm{in}} = 10\,\mathrm{AU}$. The factor $1 - \sqrt{R_{\mathrm{in}}/R}$ is

included to smooth the density near the edge of the inner disc to prevent extremely high values close to the star. For the simulations in this work, I set $\Sigma_0 = 1.53 \times 10^3\,\mathrm{g\,cm^{-2}}$. Analytical studies of the initial structure of protoplanetary discs suggest the power-law index p lies in the range $1 - 3/2$. This is consistent with an estimate for the initial surface density profile for the minimum mass solar nebula where $p \approx 3/2$ (Hayashi, 1981; Lin & Pringle, 1990) and so I use a power-law index of $p = 3/2$. The surface density profile at $t = 0\,\mathrm{yr}$ is shown in the top panel of Figure 4.1, the effect of the softening caused by the $1 - \sqrt{R_{\mathrm{in}}/R}$ term in Equation 4.1 is illustrated in the gradual decrease of Σ towards the inner disc radius.

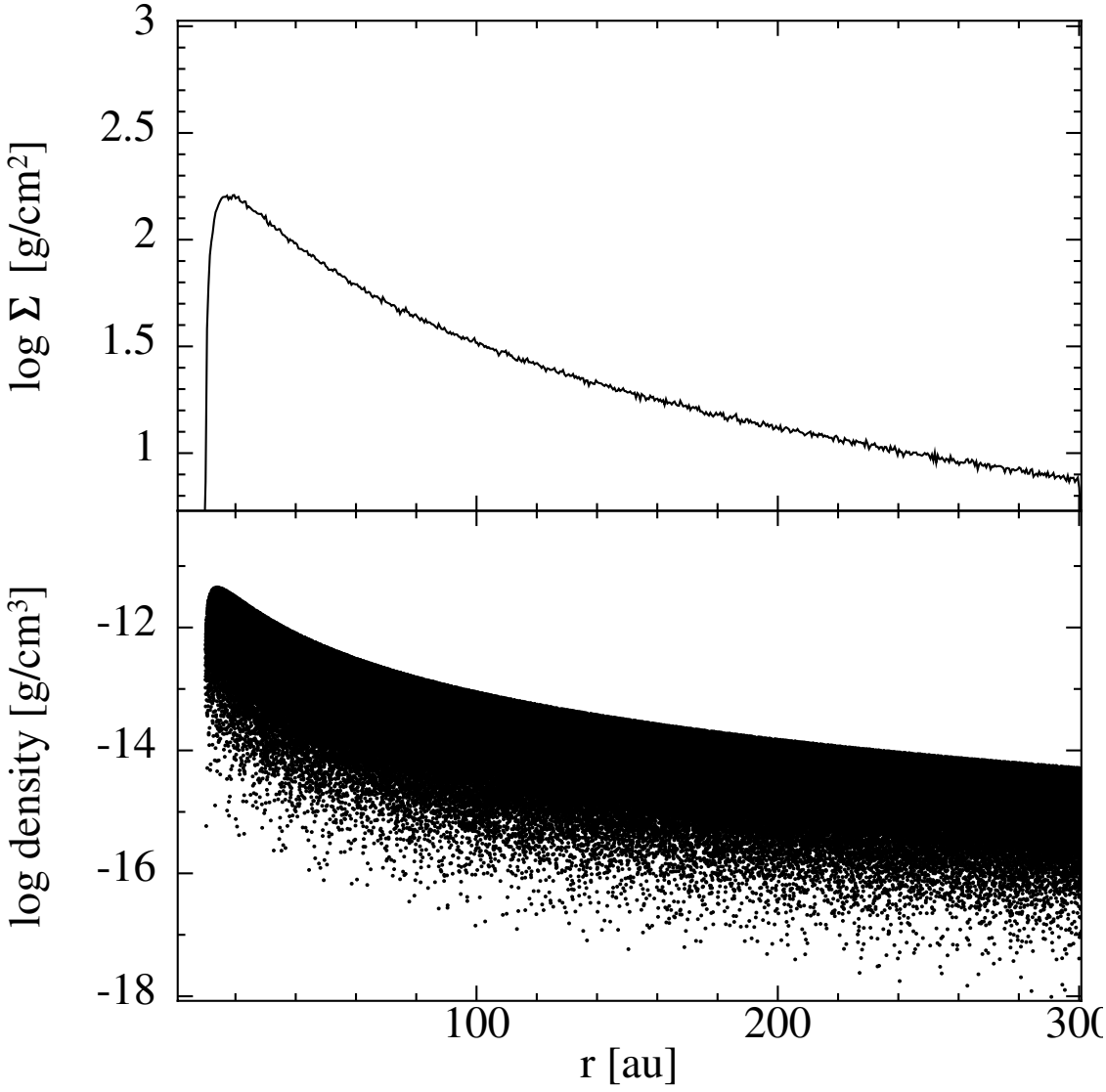

Figure 4.1: The initial surface density (top) and volume density (bottom) of the disc as functions of the radius.

4.1.2 Disc Vertical Structure

The vertical structure of the disc is derived by considering the vertical force balance at a point z above the mid-plane. The vertical component of the gravitational

acceleration must be balanced by the vertical pressure gradient of the gas i.e.

$$\frac{1}{\rho}\left(\frac{dP}{dz}\right) = -\frac{GM_* z}{(R^2+z^2)^{1/2}}, \tag{4.2}$$

where ρ and P are the density and pressure of the gas, M_* is the mass of the host star, R is the radius and z is the distance above the mid-plane. The pressure of the gas can be written as $P = \rho c_{\rm s}^2$ and assuming that the disc is in Keplerian rotation, the above yields

$$\rho = \rho_0 e^{-z^2/2h^2}, \tag{4.3}$$

where h is the disc scale height, $h = c_{\rm s}/\Omega$, and ρ_0 is the mid-plane density, which can be written in terms of the surface density

$$\rho_0 = \frac{1}{\sqrt{2\pi}}\frac{\Sigma}{h}. \tag{4.4}$$

The volume density of the disc as a function of the radius is shown in the bottom panel of Figure 4.1.

4.1.3 Disc Temperature Profile

The temperature profile of the discs is given by

$$T(R) = T_{\rm 1AU}\left(\frac{R}{\rm AU}\right)^{-0.5}. \tag{4.5}$$

To test the effect of the disc temperature profile on the formation and evolution of fragments in a gravitationally unstable disc, I choose $\rm T_{1\,AU}(K) = [150,\,200]\,K$.

4.1.4 Disc Stability - Toomre Q

As discussed in §1.5, fragmentation is thought to occur at large distances from the central star where the gas can cool on a suitably short timescale and Q<1. I choose the disc initial conditions outlined above that ensure that the disc is initially violently unstable outside of approximately 50 AU, this is to ensure prompt fragmentation.

This is shown in the left hand panel of Figure 4.2. The Toomre mass, shown in the right hand panel of Figure 4.2 as a function of distance from the star, indicates the expected initial mass of the fragments. The solid and dashed lines correspond to the Toomre Mass for simulations where the $T_{1\,AU}$ is 200 K and 150 K, respectively. Both mass profiles remain below the Brown Dwarf mass threshold of 13 M_J. The Toomre mass also provides a baseline for resolution in SPH simulations of gravitationally unstable discs. Nelson (2006) states that the Toomre mass must be resolved by at least 6 times the number of nearest neighbours. In the simulations run here, the minimum value the Toomre mass is $M_T \sim 2.5\,M_J$. This mass is sufficiently resolved as it is in far in excess of $200\times N_{Neigh}$ where $N_{Neigh} \sim 58$ i.e. the average number of neighbours in PHANTOM.

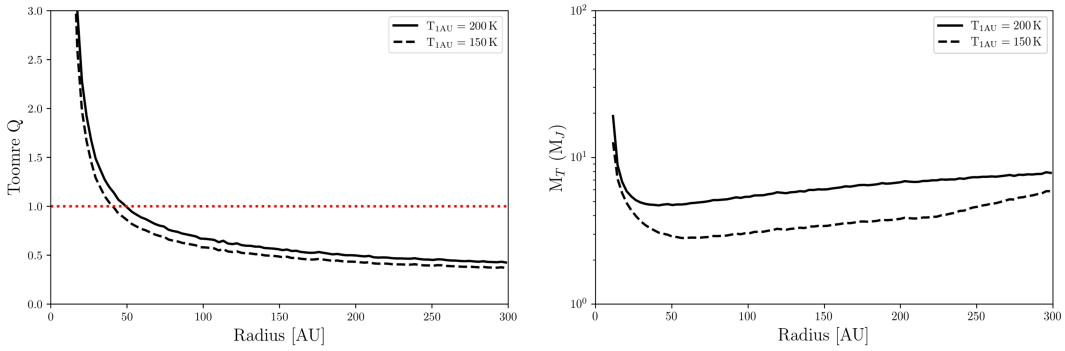

Figure 4.2: *Left:* The Toomre parameter Q as a function of radius at the start of the simulations. The disc is initially unstable at radii greater than ≈ 50 AU. The threshold for stability of Q = 1 is shown by the dotted line. *Right:* The Toomre mass, indicating the expected fragment mass, as a function of radius at the start of the simulations.

4.1.5 Disc Rotation

The effect of the disc mass cannot be neglected in the case of very massive discs and must be taken into account when setting initial velocities. Rather than setting the

gas around the star into simple Keplerian rotation such that

$$v = \left(\frac{GM_*}{R}\right)^{1/2}, \tag{4.6}$$

the mass of the disc interior to the radius R must be considered. I therefore set

$$v = \left[\frac{G[M_* + M_{\rm disc}(< R)]}{R}\right]^{1/2}, \tag{4.7}$$

where $M_{\rm disc}(< R)$ is the mass of the disc interior to R. Figure 4.3 shows the effect of the disc self-gravity on the velocity of the gas.

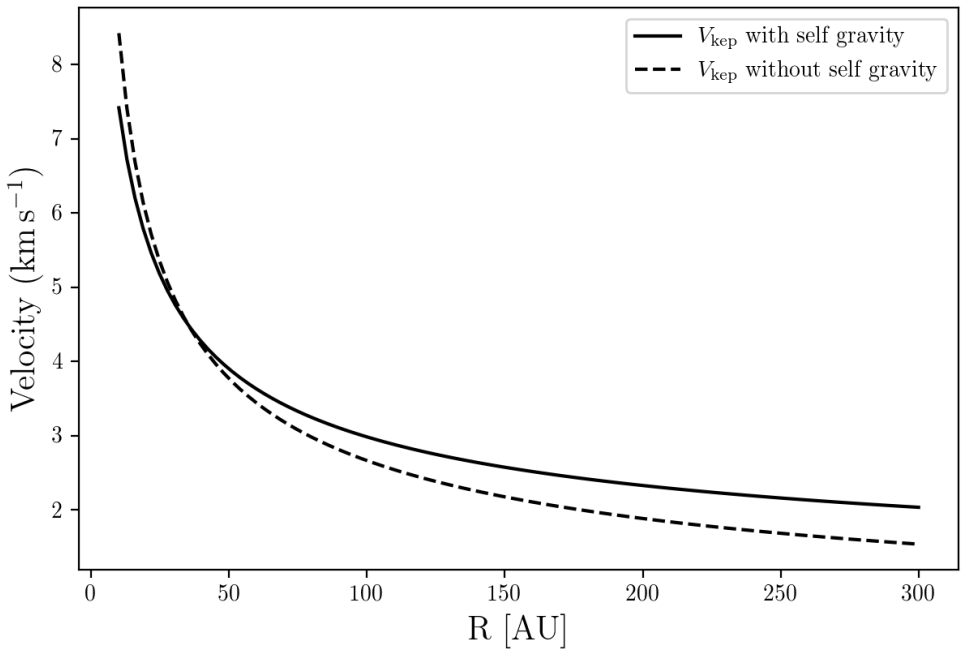

Figure 4.3: The mass of the disc is sufficiently large to have a non-trivial effect of the disc velocity and so self-gravity must be considered. The solid and dashed lines show the Keplerian velocity with and without the effect of self gravity, respectively.

4.2 Disc Thermodynamics

A full 3D multi-frequency model of raditative transfer (RT) as a representation of the thermodynamics is extremely computationally expensive. Studies using an accurate model of RT are often limited to single snapshots rather than full simulations. Traditionally, the approximation of the effects of radiative transfer in the context of gravitational collapse has been achieved by adopting a barotropic equation of state i.e. $P \propto \rho^{\gamma}$ where γ is the adiabatic index as this is far less taxing computationally.

4.2.1 Barotropic Equation of State

A barotropic equation of state (EOS) approximates the effect of radiative transfer in the context of star formation and gravitational collapse. It is used to emulate the evolution of a collapsing fragment as described in Chapter 2 by adjusting the critical densities and adiabatic exponents to best reflect the results of more exhaustive thermodynamic simulations.

Equation 4.8 is the form of the barotropic EOS used in PHANTOM which divides the thermodynamic evolution into three regions, the boundaries of which are controlled by ρ_1, ρ_2 and ρ_3

$$\frac{P}{\rho} = \begin{cases} c_{s,0}^2 & \text{if } \rho < \rho_1 \\ c_{s,0}^2 \left(\frac{\rho}{\rho_1}\right)^{(\gamma_1-1)} & \text{if } \rho_1 \leq \rho < \rho_2 \\ c_{s,0}^2 \left(\frac{\rho_2}{\rho_1}\right)^{(\gamma_1-1)} \left(\frac{\rho}{\rho_1}\right)^{(\gamma_2-1)} & \text{if } \rho_2 \leq \rho < \rho_3 \\ c_{s,0}^2 \left(\frac{\rho_2}{\rho_1}\right)^{(\gamma_1-1)} \left(\frac{\rho_3}{\rho_2}\right)^{(\gamma_2-1)} \left(\frac{\rho}{\rho_3}\right)^{(\gamma_3-1)} & \text{if } \rho \geq \rho_3, \end{cases} \tag{4.8}$$

where γ_1, γ_2 and γ_3 are the adiabatic indices that control the stiffness of the equation of state in the three regions i.e. to what degree the pressure increases for an increase in density. Though the simulations presented here do not include the effect of magnetic fields, it has been suggested that a stiffer EOS can mimic the effect of the

magnetic field pressure. The magnetic pressure that would arise from the inclusion of the magnetic field would cause a greater increase in pressure per unit temperature, resulting in a steeper slope in the log T - log ρ plane i.e. a stiffer EOS e.g. (Bitsch, Boley & Kley, 2013). Figure 4.4 is a schematic representation of Equation 4.8 in the log T - log ρ plane. This barotropic evolution is a good match to that shown in Figure 2.2 which illustrates the collapse of a molecular cloud using the Stamatellos et al. (2007) diffusion approximation of radiative transfer, a more rigorous treatment of the effects of thermodynamics.

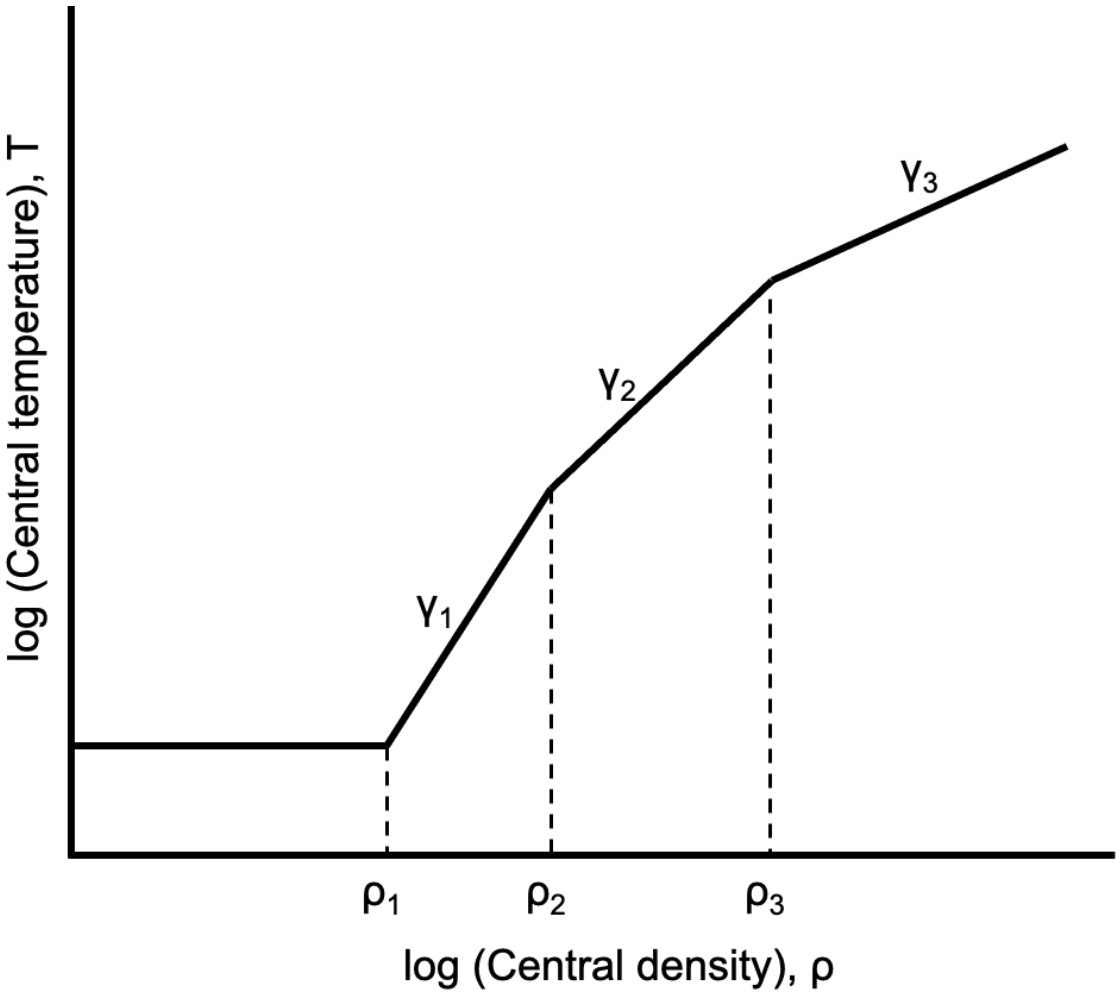

Figure 4.4: A schematic representation of the barotropic equation of state implemented in PHANTOM. The critical densities ρ_1, ρ_2 and ρ_3 illustrate the region boundaries described by Equation 4.8.

I use this equation of state to model the fragmentation of protoplanetary discs and the subsequent collapse of the fragments through to the formation of the second core. A stiffer barotropic equation of state, i.e. one with a steeper profile in the log T - log ρ plane is expected to produce fewer fragments. This is due to an increased temperature at a given density so that thermal pressure in the interior of a collapsing cloud or fragment is enough to maintain support against gravitational collapse (Stamatellos & Whitworth, 2009).

4.2.2 The Hybrid Barotropic EOS

The barotropic equation of state has a known artefact in that it underestimates the temperature of material around stars due to the lack of radiative feedback (Bate, 2009). To account for the effect of stellar heating on the temperature of the disc, I combine Equations 4.5 and 4.8 to form a hybrid equation of state in which the temperature of the gas is given by the maximum of Equations 4.5 and 4.8. At large distances from the star, where the gas is diffuse and has not reached $\rho = \rho_1$ (see Figure 4.4), the temperature of the gas is given by Equation 4.5. In regions of higher density, the temperature is enhanced beyond the isothermal profile in accordance with Equation 4.8.

4.3 Simulation Setup

I initially perform a benchmark run with $[\gamma_1,\ \gamma_2,\ \gamma_3] = [5/3,\ 7/5,\ 1.1]$. These values are chosen to reflect the behaviour of thermodynamic evolution of molecular Hydrogen which behaves like a monotomic gas at low temperatures, hence $\gamma_1 = 5/3$. As the temperature of the gas increases, the rotational degrees of freedom are excited and the adiabatic index decreases to $\gamma_1 = 7/5$. I explore a parameter space covering 16 sets of densities between boundaries and adiabatic indices, γ listed in Table 4.1 and shown in Figure 4.5. This is done to assess the effect of the thermodynamics on the evolution of fragments that form in gravitationally unstable discs and to compare them with observations of exoplanets. I choose to set $\gamma_1 = \gamma_2$ in this study.

As discussed in Chapter 2, a barotropic EOS mimics the thermodynamics of collapsing clouds during the formation of the first and second hydrostatic cores without the computational expense of more rigorous methods. It has also been shown that fragments forming in gravitational unstable discs undergo a collapse similar to that of a collapsing cloud, making it particularly applicable for this study

(Stamatellos & Whitworth, 2009; Mercer & Stamatellos, 2020). Additionally, a barotropic EOS allows for very precise control of the thermodynamics, meaning the effect of the parameters can be studied in detail.

Fragments form the first core at densities of order $\rho_1 \approx 10^{-13}\,\mathrm{g\,cm^{-3}}$ when the fragment becomes optically thick. I therefore investigate values of $\rho_1 = [1\times10^{-13}, 6\times10^{-13}]\,\mathrm{g\,cm^{-3}}$. This effectively corresponds to different metallicities/opacities of the fragments/disc.

I follow the evolution of fragments up to central densities $\rho = 10^{-3}\,\mathrm{g\,cm^{-3}}$. At this point a sink particle is introduced with an accretion radius of 0.1 AU. Sink particles allow us to continue the simulation without a prohibitively small timestep, meaning that other fragments can evolve to this density.

For simulations with stiff equations of state, only a few fragments form due to an increased temperature at a given density providing support against collapse. In these cases I run additional simulations with different initial particle distributions (maintaining the same macroscopic density profile) to increase the number of fragments.

Table 4.1: The critical densities and adiabatic indices explored in this work (see Equation 4.8). The second and third critical densities, ρ_2 and ρ_3 are those at which the temperature of the gas reaches values of 100 K (excitation of the rotational degrees of molecular hydrogen) and 2000 K (hydrogen dissociation) respectively. The temperature of the disc at 1 AU from the host star is also varied (final column).

Run ID	$\rho_1\,(\mathrm{g\,cm^{-3}})$	$\rho_2\,(\mathrm{g\,cm^{-3}})$	$\rho_3\,(\mathrm{g\,cm^{-3}})$	γ_1	γ_2	γ_3	$\mathrm{T_{1\,AU}(K)}$
Benchmark	1×10^{-13}	3.27×10^{-12}	5.86×10^{-9}	1.66	1.4	1.1	200.0
Run 1	1×10^{-13}	3.16×10^{-11}	5.66×10^{-8}	1.4	1.4	1.1	200.0
Run 2	1×10^{-13}	3.16×10^{-11}	5.66×10^{-8}	1.4	1.4	1.1	150.0
Run 3	1×10^{-13}	3.27×10^{-12}	3.06×10^{-10}	1.66	1.66	1.1	200.0
Run 4	1×10^{-13}	3.27×10^{-12}	3.06×10^{-10}	1.66	1.66	1.1	150.0
Run 5	1×10^{-13}	1.78×10^{-12}	7.52×10^{-11}	1.8	1.8	1.1	200.0
Run 6	1×10^{-13}	1.78×10^{-12}	7.52×10^{-11}	1.8	1.8	1.1	150.0
Run 7	1×10^{-13}	1×10^{-8}	3.20×10^{-2}	1.2	1.2	1.1	200.0
Run 8	1×10^{-13}	1×10^{-8}	3.20×10^{-2}	1.2	1.2	1.1	150.0
Run 9	6×10^{-13}	1.9×10^{-10}	3.39×10^{-7}	1.4	1.4	1.1	200.0
Run 10	6×10^{-13}	1.9×10^{-10}	3.39×10^{-7}	1.4	1.4	1.1	150.0
Run 11	6×10^{-13}	1.96×10^{-11}	1.84×10^{-9}	1.66	1.66	1.1	200.0
Run 12	6×10^{-13}	1.96×10^{-11}	1.84×10^{-9}	1.66	1.66	1.1	150.0
Run 13	6×10^{-13}	1.07×10^{-11}	4.51×10^{-10}	1.8	1.8	1.1	200.0
Run 14	6×10^{-13}	1.07×10^{-11}	4.51×10^{-10}	1.8	1.8	1.1	150.0
Run 15	6×10^{-13}	6×10^{-8}	1.92×10^{-1}	1.2	1.2	1.1	200.0
Run 16	6×10^{-13}	6×10^{-8}	1.92×10^{-1}	1.2	1.2	1.1	150.0

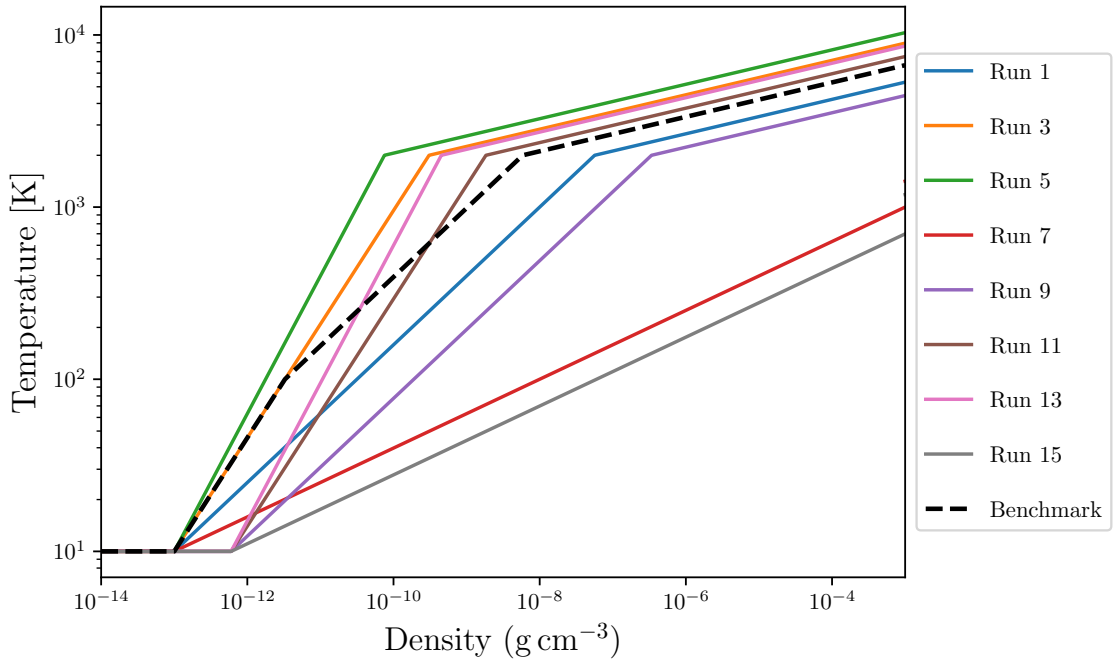

Figure 4.5: The parameter space of barotropic EOS explored in this study in the log T - log ρ plane. Runs 7 and 15 have a very shallow adiabatic region and so do not reach 2000 K before fragments are replaced by sink particles at $\rho = 10^{-3}$g cm^{-3}. This shows the standard EOS before the effects from stellar radiative feedback are included (see discussion in §4.2.2). The dashed black line shows the benchmark run.

Chapter 5

The Structure of Disc–Instability Protoplanets

I perform a benchmark simulation with γ_1, γ_2 and γ_3 set to 1.66, 1.4 and 1.1, respectively and the critical density at which the EOS switches from isothermal to adiabatic set to $\rho_1 = 10^{-13}\,\mathrm{g\,cm^{-3}}$, (see § 4.3 for full details). The run is used to provide a basis for comparison to the fragments/protoplanets that form in discs with thermodynamics controlled by the equations of state listed in Table 4.1. In this chapter, I will discuss the formation of the fragments and their general morphology.

5.1 Formation of Fragments

The disc is initially gravitationally unstable and spiral features develop early in its evolution. Densely packed spirals close to the central star give way to instabilities outside of approximately 100 AU (see Figure 5.1). The conditions in these outer regions are such that the Toomre parameter Q, is less than one and the spiral arms are susceptible to fragmentation. The evolution of the resulting fragments is not disrupted by tidal shredding nor suppressed due to the of thermal pressure as they would be in the inner, hotter regions of the disc. Fragmentation of the spiral arms

occurs within a few kyrs of evolution, as it is shown in panel f) of Figure 5.1.

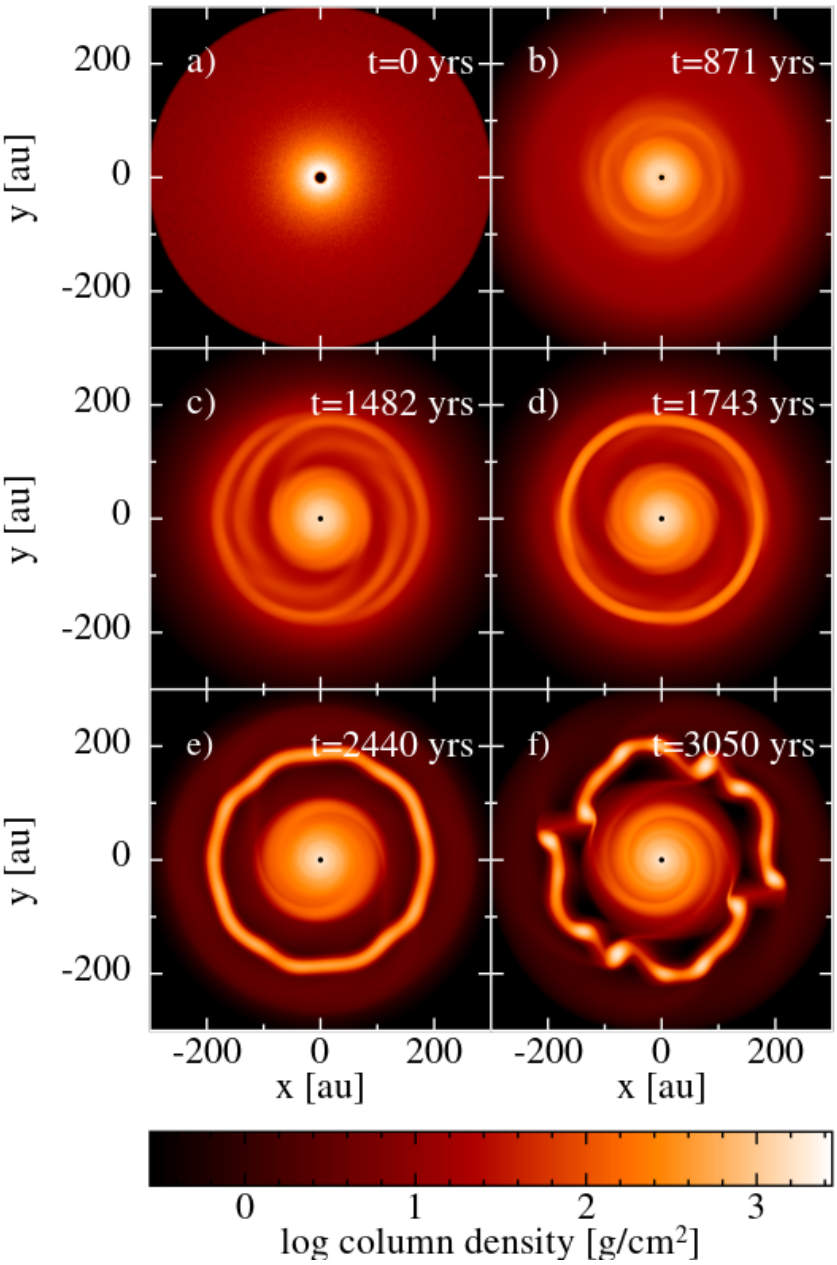

Figure 5.1: The development of instabilities in the disc throughout its evolution. Panel a) shows the disc at the start of the run. Spiral arms develop within 1482 yr as it is shown in panels b) and c). Spirals in the outer regions, where the Toomre parameter $Q < 1$, go on to break up into fragments unhampered by thermal pressure and tidal disruptions (see panels d) - f). This, as well as a number of other plots throughout this thesis were created using the SPH visualisation tool SPLASH (Price, 2007)

Shortly after the fragmentation of spiral arms, the resulting fragments are extended and are ∼30 - 50 AU in diameter with central densities of $\sim 10^{-12}\,\mathrm{g\,cm^{-3}}$. The fragments migrate inwards, colliding with the dense material in the inner disc, accreting more mass and contracting to evolve to smaller scale, higher density fragments that have the potential to continue their evolution to form protoplanets. In the 5000 yr that I follow the evolution of the disc, four fragments evolve to central densities of $10^{-3}\,\mathrm{g\,cm^{-3}}$. The rest are either disrupted, undergo mergers or do not reach high central densities by the end of the simulation. The four fragments form between ≈ 55 - 250 AU. Their positions at different stages of their evolution are shown in Table 5.1.

Table 5.1: The distance (R) of the fragments from the central star when their central densities are $\rho_1 = 10^{-9}\,\mathrm{g\,cm^{-3}}$, $\rho_2 = 10^{-6}\,\mathrm{g\,cm^{-3}}$ and $\rho_3 = 10^{-3}\,\mathrm{g\,cm^{-3}}$. Fragments F3 and F4 form by the merging of two low density fragments. This is followed by a period of rapid accretion and increase in density meaning that their evolution occurs on a much shorter timescale. This is shown by the small change in position across the evolutionary phase.

ID	R_{ρ_1}	R_{ρ_2}	R_{ρ_3}	t_{ρ_1}	t_{ρ_2}	t_{ρ_3}
-	(AU)	(AU)	(AU)	(yr)	(yr)	(yr)
F1	63	59	59	4054	4430	4431
F2	63	55	55	4055	4429	4429
F3	243	245	245	4502	4513	4513
F4	243	245	245	4505	4515	4515

Figures 5.2 and 5.3 show each of these fragments at three key stages of their evolution: after the formation of the first core ($\rho_c = 10^{-9}\mathrm{g\,cm^{-3}}$), shortly after the formation of the second core ($\rho_c = 10^{-5}\mathrm{g\,cm^{-3}}$) and when they reach density $\rho_c = 10^{-3}\mathrm{g\,cm^{-3}}$. The latter is shown in Figure 5.3 with axis and colour bar limits adjusted to illustrate the internal structure more clearly.

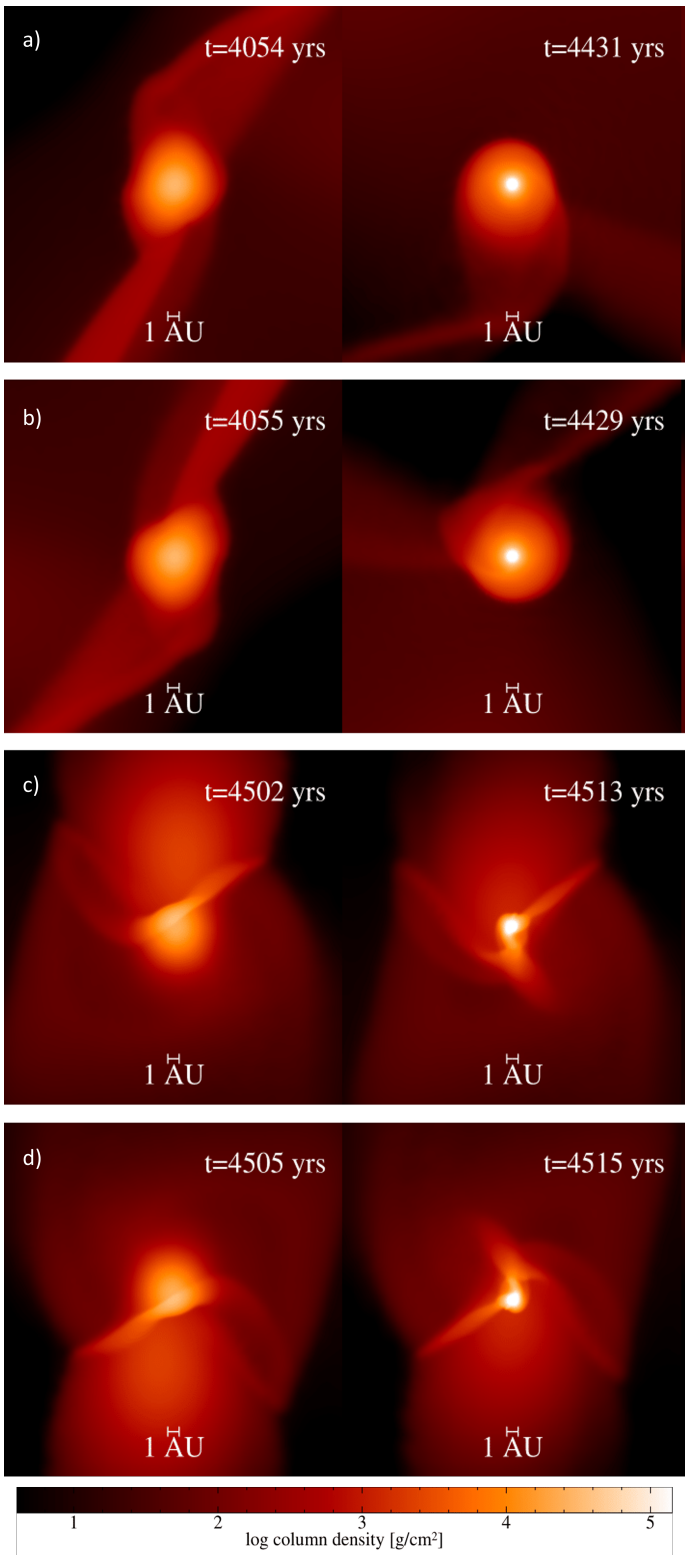

Figure 5.2: All 4 fragments (one fragment per row) that formed in the benchmark run at $\rho_c = 10^{-9}$ and $\rho_c = 10^{-5}\,\mathrm{g\,cm^{-3}}$ (left to right). Panels a) - d) show fragments 1 - 4 respectively.

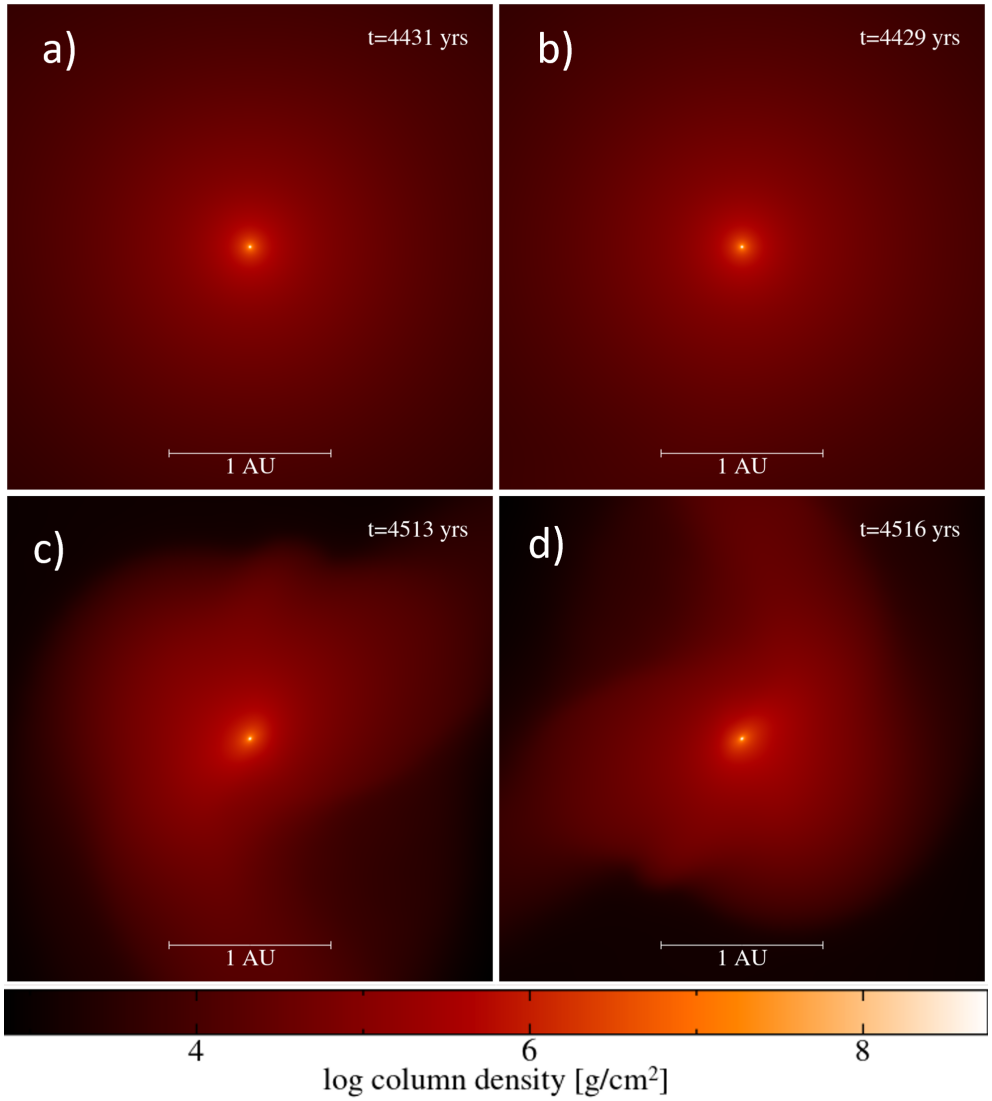

Figure 5.3: All 4 fragments when the central densities reach $\rho_c = 10^{-3}$. zoomed in to show the internal structure. Panels a) - d) show fragments 1 - 4 respectively.

The first two fragments to form, hereafter F1 and F2, do so at the intersection of two or more spiral arms and accrete most of their material from the inner disc. Figures 5.4 and 5.5 show the formation history of F1 and F2, respectively. The bright regions indicate the gas that eventually ends up within the first core of the fragment at the end of the simulation whereas the greyscale part of the plot shows the full disc. Most of the gas contained within F1 and F2 is located within a radius

of approximately 100 AU rather than contained by one or more of the fragments of the outer spiral arms. Once formed, the fragments accrete gas from the disc slowly, evolving from central densities of $\rho_c = 10^{-9}\,\mathrm{g\,cm^{-3}}$ to $\rho_c = 10^{-3}\,\mathrm{g\,cm^{-3}}$ within $\sim 375\,\mathrm{yr}$. The final stage of the fragments, shortly before a sink particle is introduced is shown in the right hand panels in the top two rows of Figure 5.2. They are roughly axisymmetric with filamentary structures tethering them to the spiral arm.

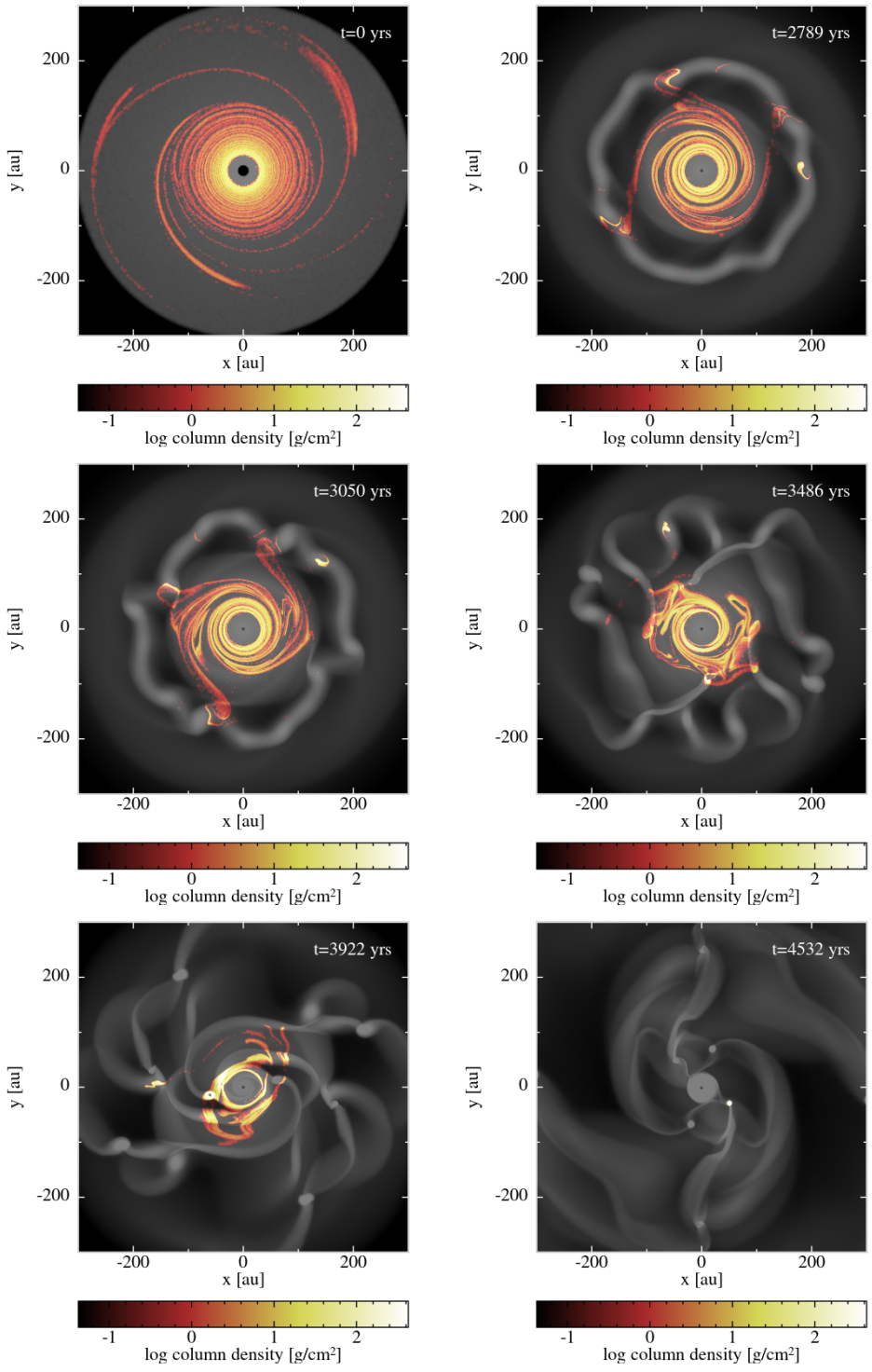

Figure 5.4: The formation history of F1. Bright regions indicate the distribution of material that ends up in the fragment various points throughout its development.

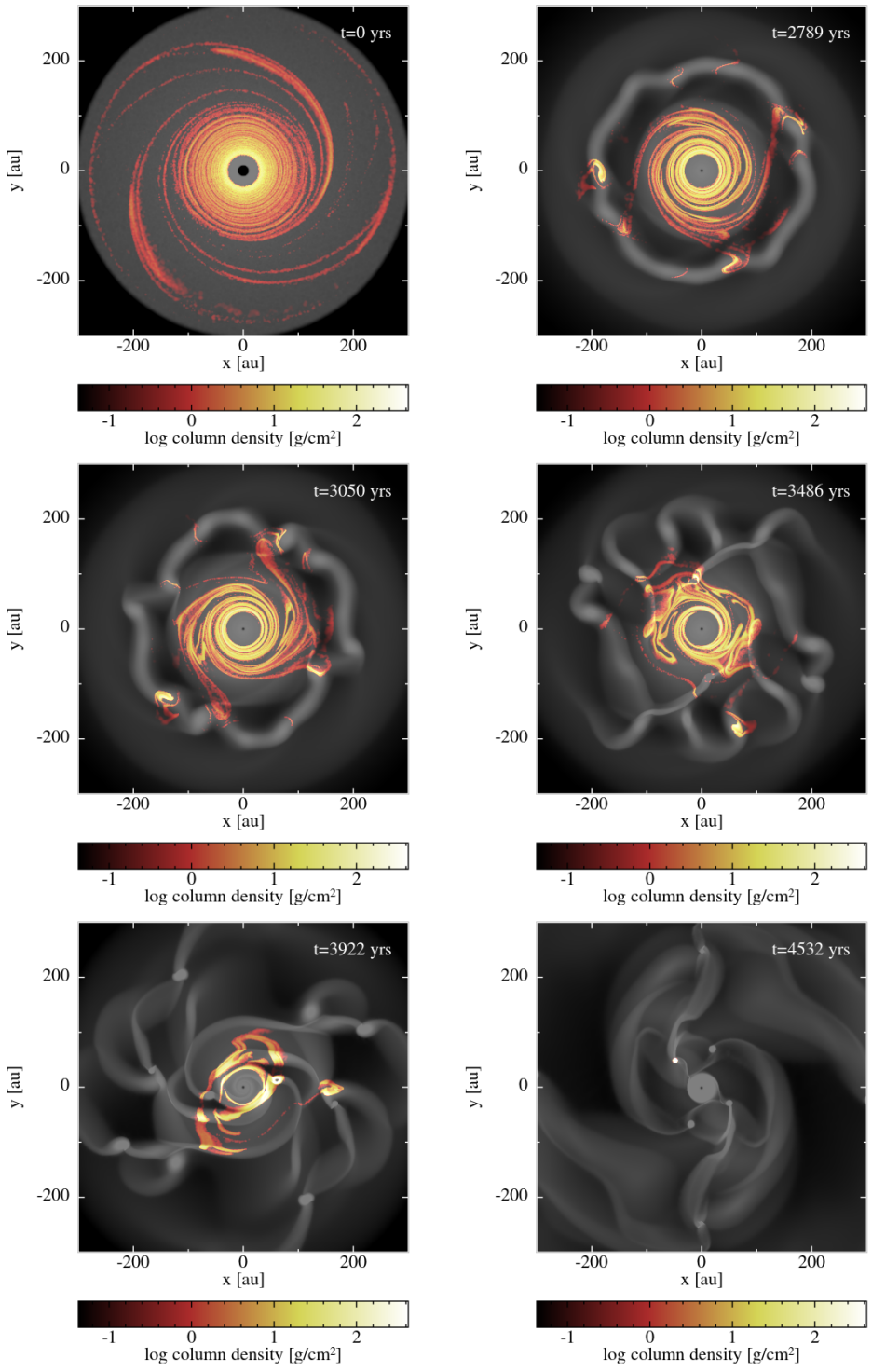

Figure 5.5: The formation history of F2. The colour key is the same as that in Figure 5.4

Fragments 3 and 4, hereafter F3 and F4, form by the merging of two already established high density regions of gas. This process is shown in the lower two panels of Figures 5.6 and 5.7. Individually, these 'proto-fragments' that combined to form F3 and F4 were of lower density. However, following the merging event, the gas from one is stripped and accreted by the other. This causes a very rapid increase in mass and so the following evolutionary stage occurs on a much shorter timescale than in the cases of F1 and F2, taking only $\approx 10\,\mathrm{yr}$ to evolve from $\rho_\mathrm{c} = 10^{-9}\,\mathrm{g\,cm^{-3}}$ to $\rho_\mathrm{c} = 10^{-3}\,\mathrm{g\,cm^{-3}}$.

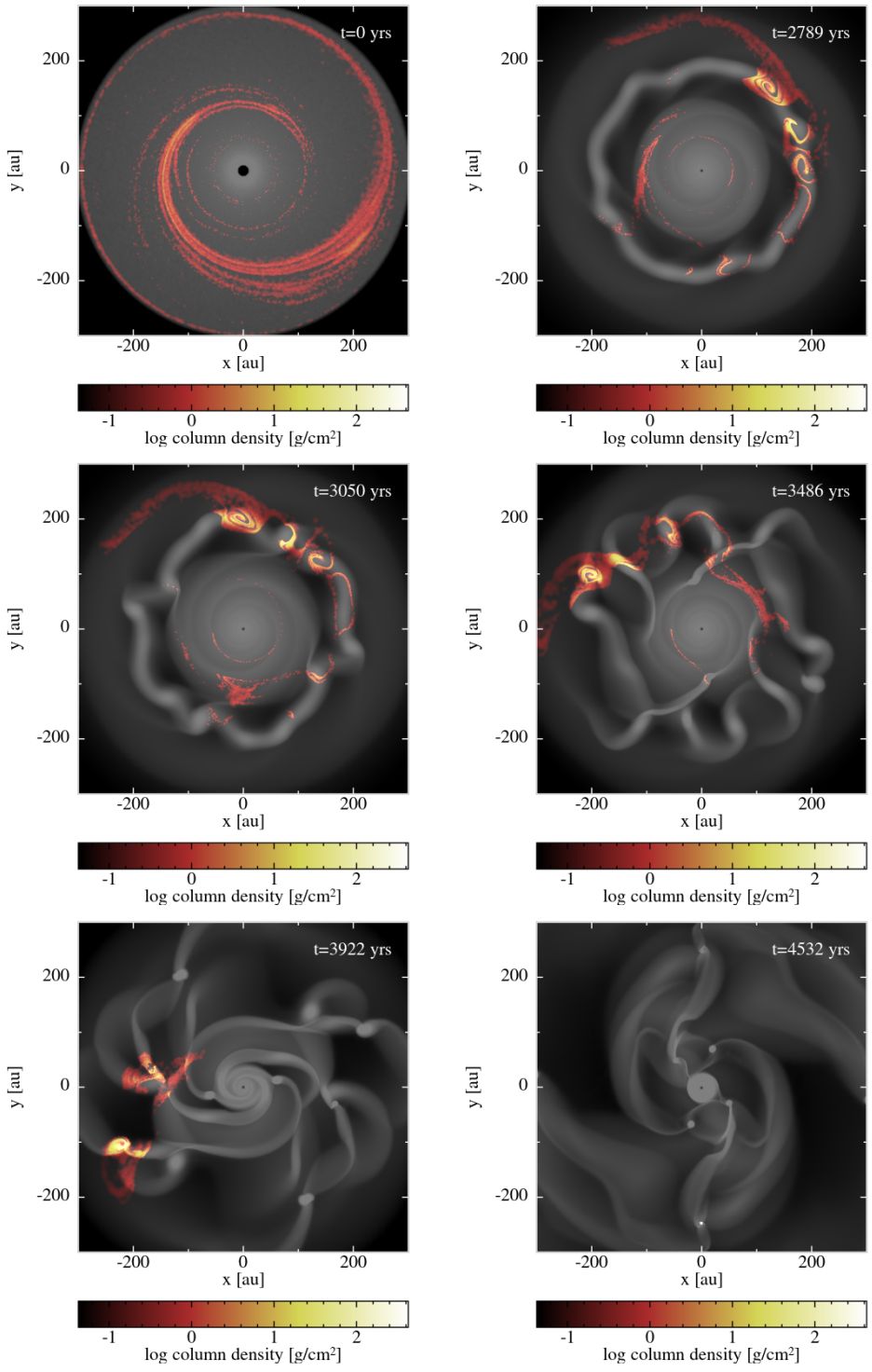

Figure 5.6: The formation history of F3. The colour key is the same as that in Figure 5.4

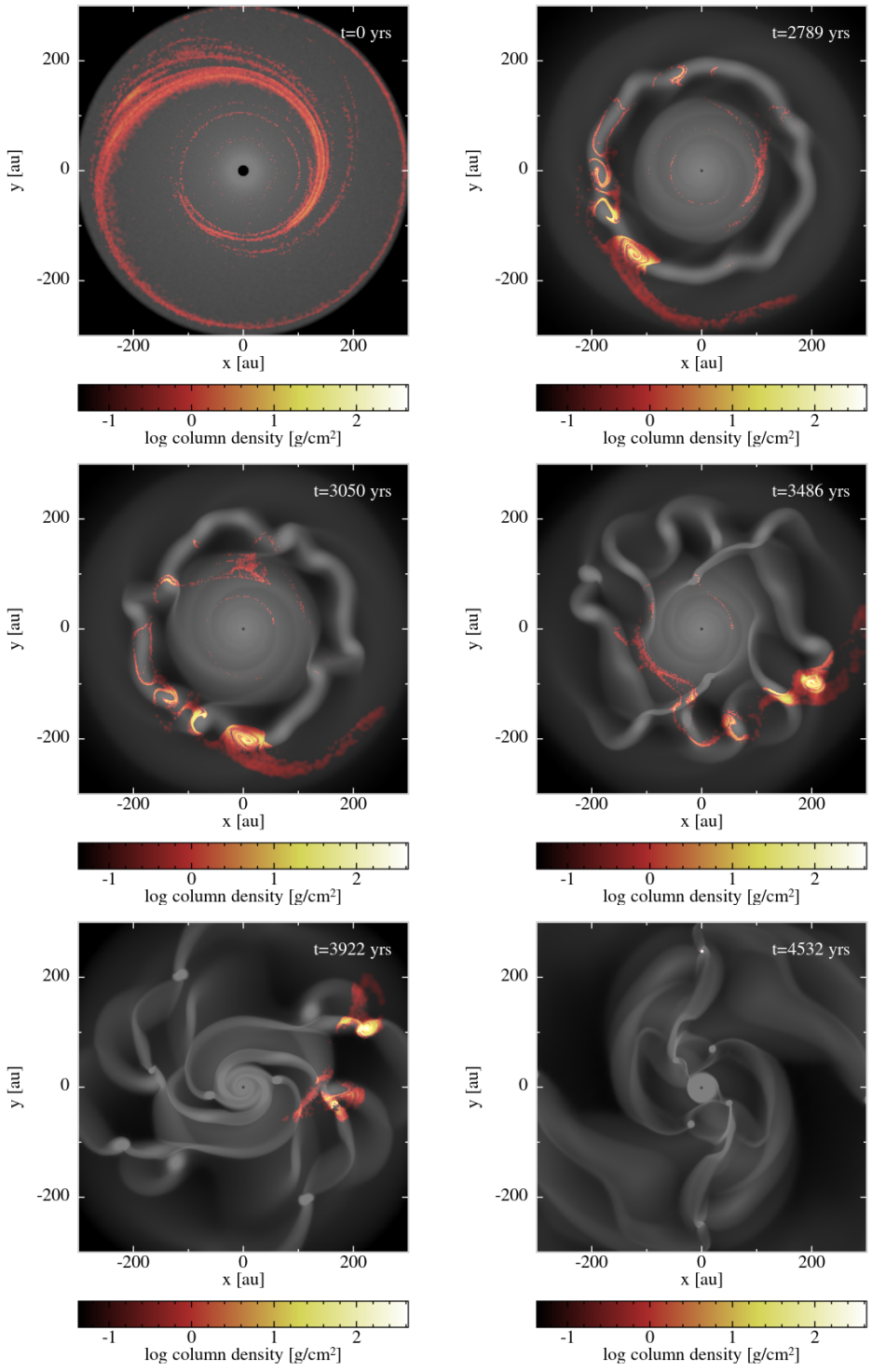

Figure 5.7: The formation history of F4. The colour key is the same as that in Figure 5.4

The gas that eventually ends up within the first cores of F3 and F4 is mostly originally located in the outer regions of the disc, originating from the outer spiral arms but also from the more diffuse material beyond them, as indicated by the extended spiral feature out to approximately 300 AU.

5.2 Fragment Properties

Initially I assume that the fragments are spherically symmetric and calculate averages of the fragment density, temperature, rotational and infall velocity (see Figure 5.14 panels a-d for the radial profiles for F1 for three stages during its evolution). I also calculate the mass contained within a radial distance r from the centre of the fragment (see panel e) of Figure 5.14) and the energy ratios $\alpha = E_{\rm therm}/E_{\rm grav}$ and $\beta = E_{\rm rot}/E_{\rm grav}$, which are shown in panel f) by the top and bottom sets of lines, respectively.

The green line in Figure 5.14 indicates the stage at which the density at the centre of the fragment is $\rho_{\rm c} = 10^{-9}\,{\rm g\,cm^{-3}}$. At this density and temperature, the thermal pressure inside the fragment resists the in-falling material leading to the development of a shock front at the location of the first hydrostatic core. This is shown by the peak in the green line in panel d) of Figure 5.14. The blue and yellow lines illustrate the structure of the fragment when the central density reaches $\rho_{\rm c} = 10^{-5}\,{\rm g\,cm^{-3}}$ and $\rho_{\rm c} = 10^{-3}\,{\rm g\,cm^{-3}}$, respectively. In both of these cases, the temperature and the centre of the fragment has surpassed that at which hydrogen dissociates and, as discussed in Chapter 2, the gravitational energy provided by the collapse is mainly used to dissociate hydrogen rather than becoming thermal energy. Unable to maintain hydrostatic equilibrium, the fragment collapses further and, as in the case of the first core, a shock front develops close to the centre of the fragment. This is the location of the second hydrostatic core, i.e. the protoplanet. The extended region between the point at which the infall velocity reaches zero and

the peak corresponds to the width of the accretion shock. I therefore calculate two radii for the first core, representing the inner and outer boundaries of the shock. While the second core will similarly have an inner and outer boundary, the inner boundary is poorly resolved and so only the outer boundary is recorded.

The mass within a radius r of the centre of the fragment at the three stages in its evolution is shown in panel e) of Figure 5.8. The mass interior to the outer boundary of the first core is $\approx 40\,\mathrm{M_J}$ at the early stages of its evolution. After the formation of the second core, the mass interior to the first core increases to $\approx 55\,\mathrm{M_J}$ but, due to the rapid second collapse, does not increase further. At all 3 stages of evolution, the thermal energy dominates over the gravitational energy towards the centre of the fragment, this is indicated in the value of α in panel f) of Figure 5.8 (top set of lines).

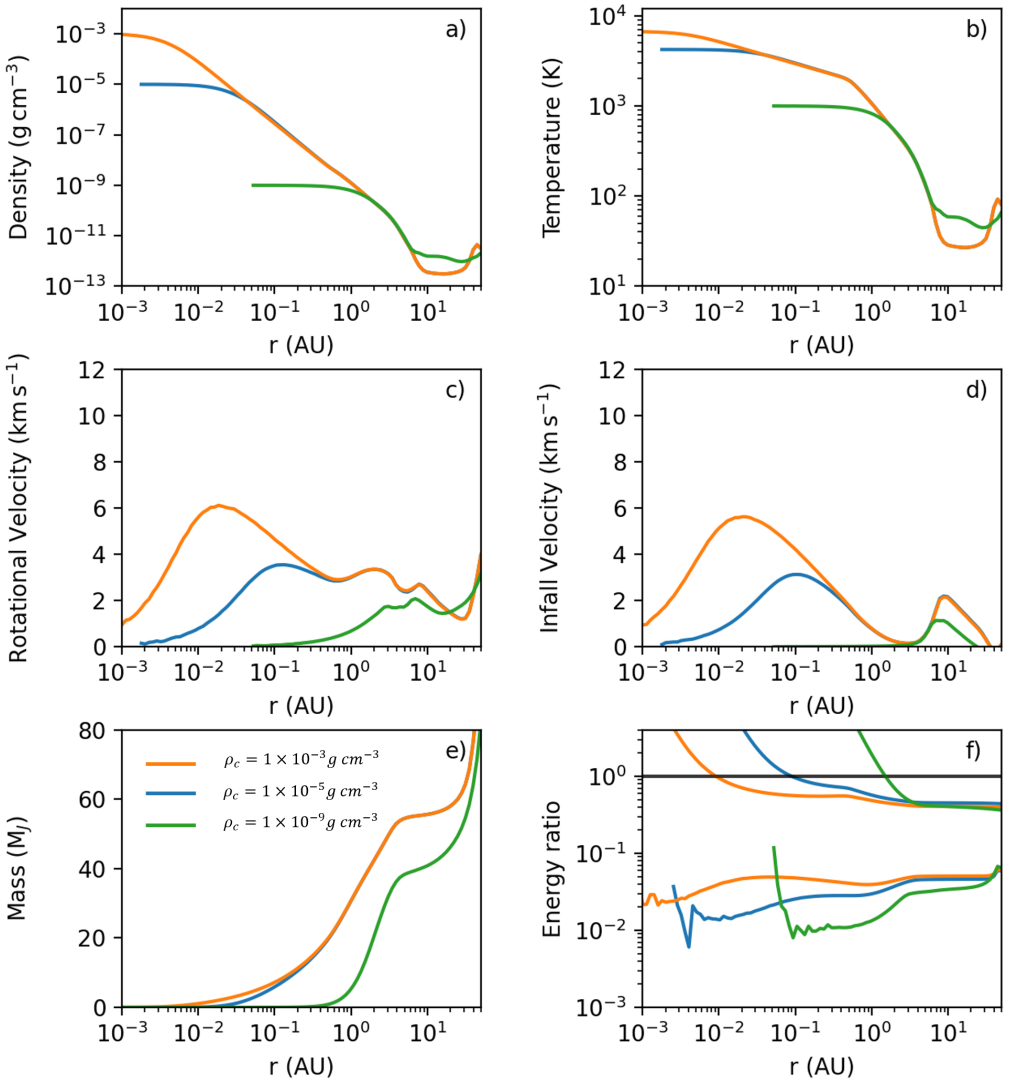

Figure 5.8: The evolution of the density, temperature, rotational velocity, infall velocity, mass and energy ratios of fragment F1. Stages at which the central density reaches $\rho_c = [10^{-9},\ 10^{-5},\ 10^{-3}]$ g cm^{-3} are shown by the green, blue and orange lines, respectively.

The temperature and density within 50 AU from the centre of a F1 is shown in

Figure 5.9. Panel a) shows the fragment at a central density of $\rho_c \sim 10^{-9} \mathrm{g\,cm^{-3}}$ and corresponds to the green line in Figure 5.8. At this stage, the fragment has undergone the first collapse and has formed the first core.

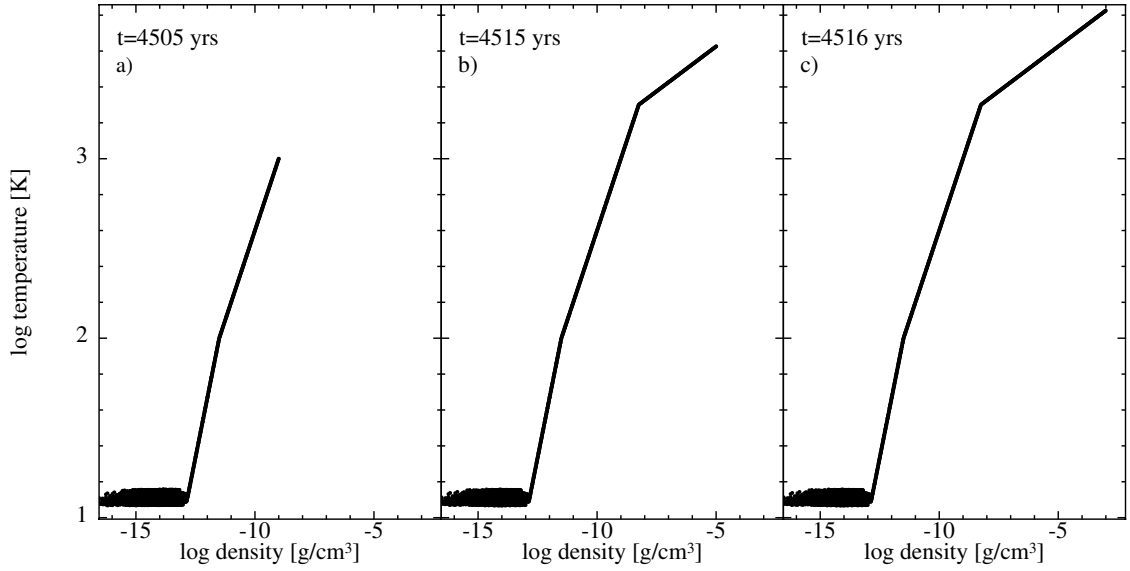

Figure 5.9: Gas within 50 AU from the centre of a F1 plotted in the log T - log ρ plane when the central density reaches $\rho_c = [10^{-9}, 10^{-5}, 10^{-3}]$ g cm^{-3} in panels a) b) and c), respectively.

Panels b) and c) show the fragment at later stages of its evolution at central densities of 10^{-5} and 10^{-3} g cm^{-3}. The temperature at the centre of the fragment has surpassed 2000 K, the threshold for hydrogen dissociation, and the second collapse begins, resulting in the formation of the second core. The blue and yellow lines in Figure 5.8 show the radial profiles of the fragment at times corresponding to those in panels b) and c) of Figure 5.9, respectively.

5.3 3 Dimensional Structure of the Fragments

Thus far is has been assumed the the fragments are spherically symmetric. To investigate the fragment structure in more detail I calculate the density, temperature,

rotational velocity and infall velocity along different directions from the centre of the fragment (±x, ±y, ±z). I define a number of logarithmic bins along each direction and count the number of particles within each bin to calculate the average value of the quantity I am interested in (e.g. density, temperature, etc).

As we will see, the fragments are approximately axisymmetric, so I also calculate axisymmetric averages on the x-y plane by constructing logarithmic annuli centred on the centre of the fragment.

The aforementioned averages from the fragments formed in the benchmark run are shown in Figures 5.10 - 5.13.

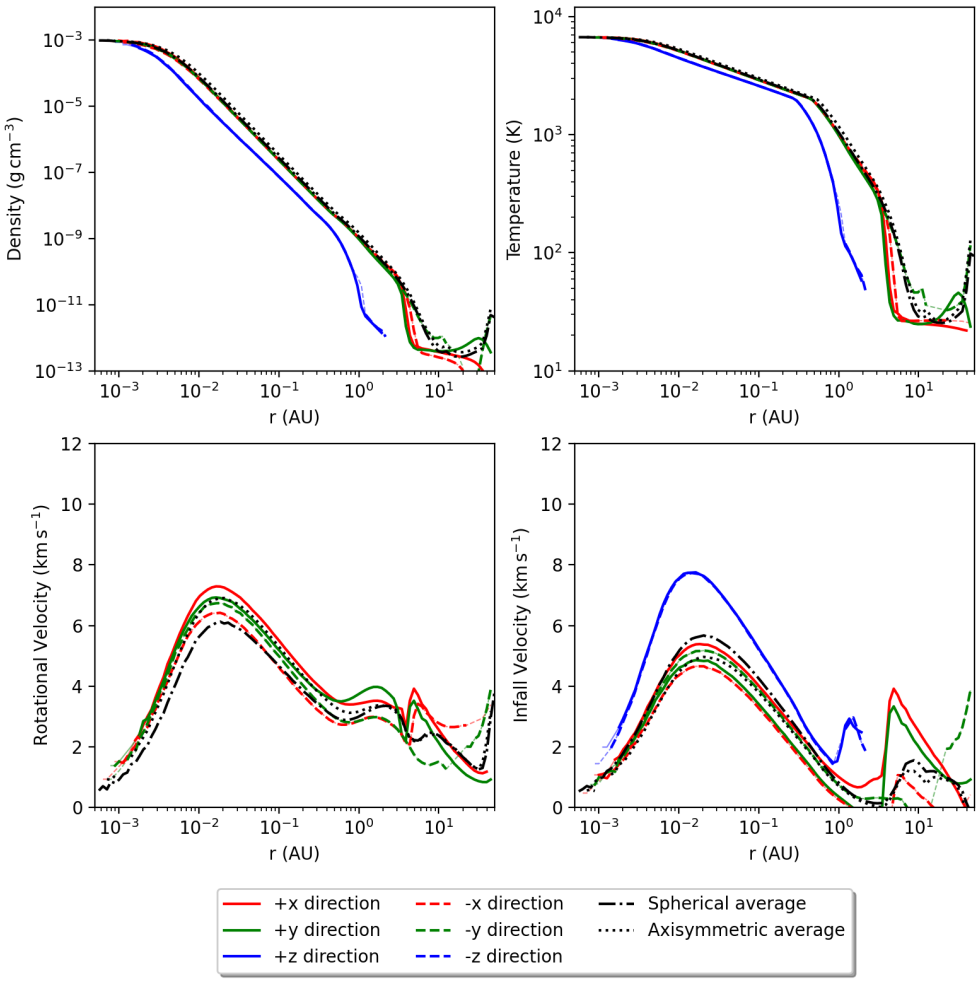

Figure 5.10: The density, temperature, rotational velocity and infall velocity at different directions from the centre of the fragment F1 (as marked on the graph). The axisymmetric average is indicated by the black dotted line and the spherical average is shown by the black dashed line.

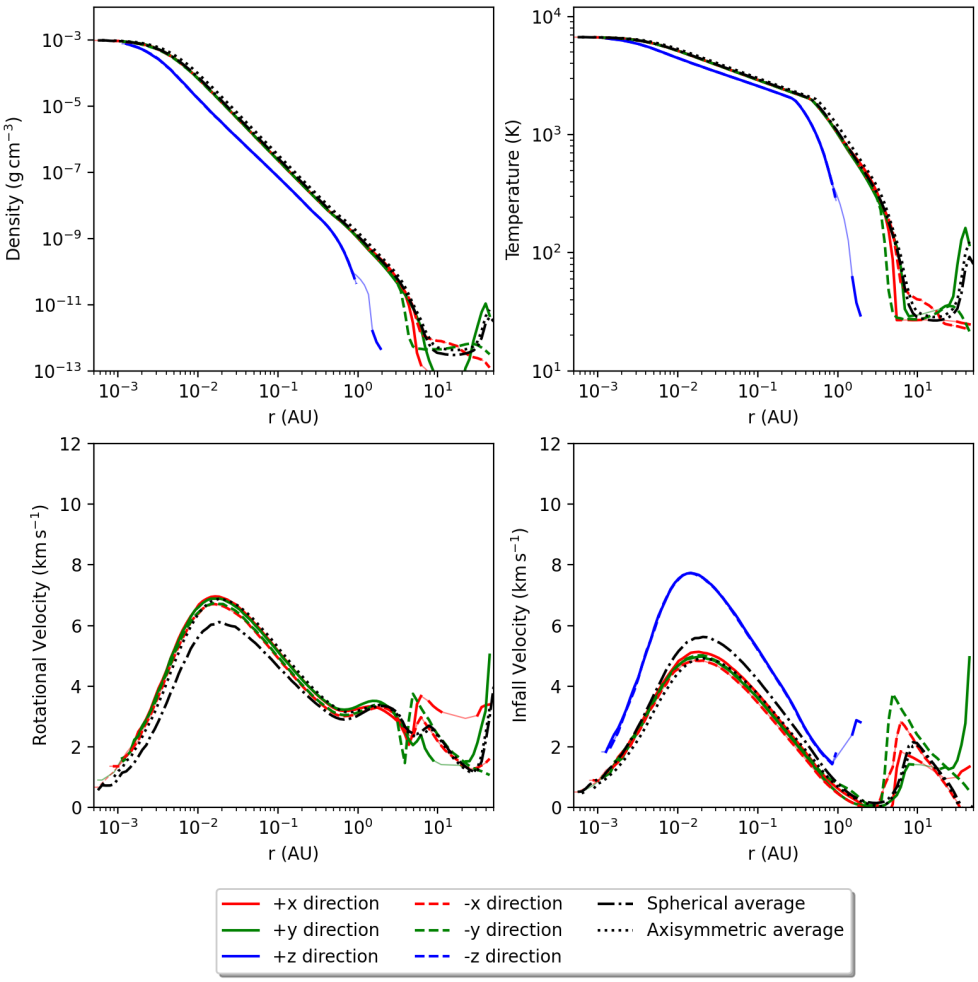

Figure 5.11: Same as in Figure 5.10 but for fragment F2.

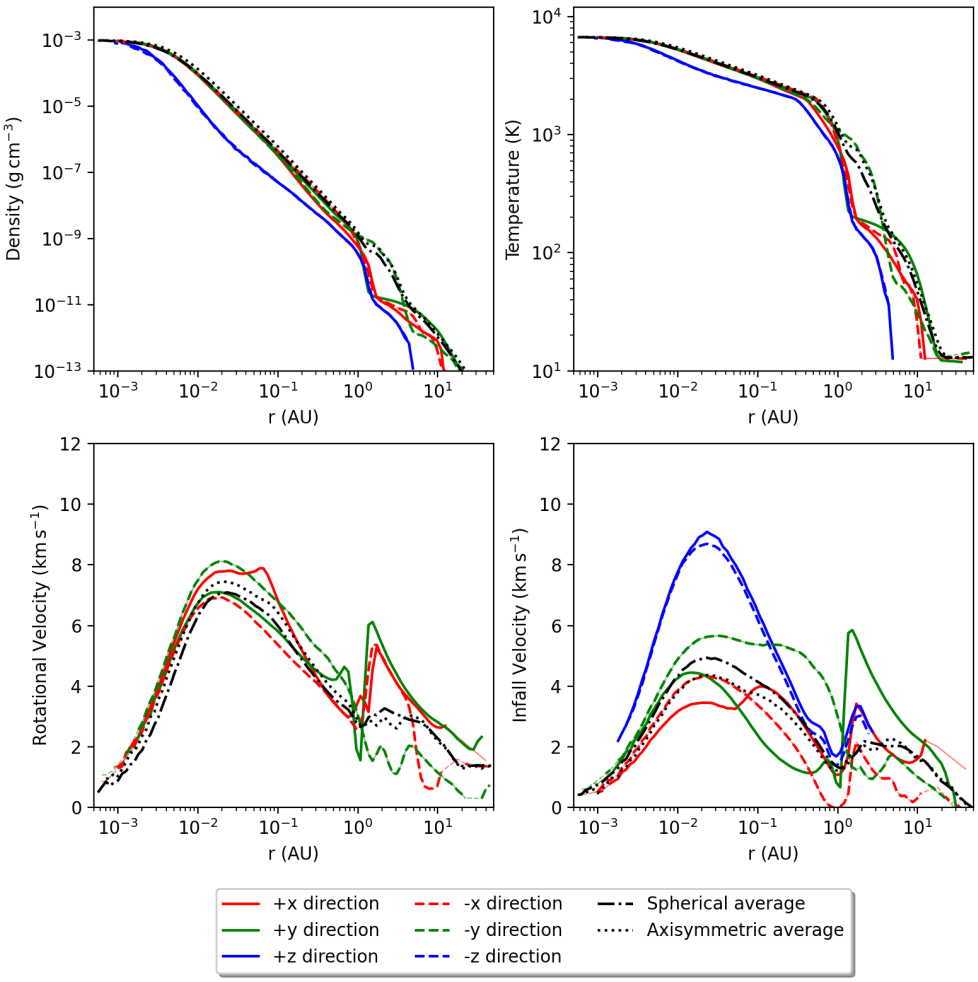

Figure 5.12: Same as in Figure 5.10 but for fragment F3.

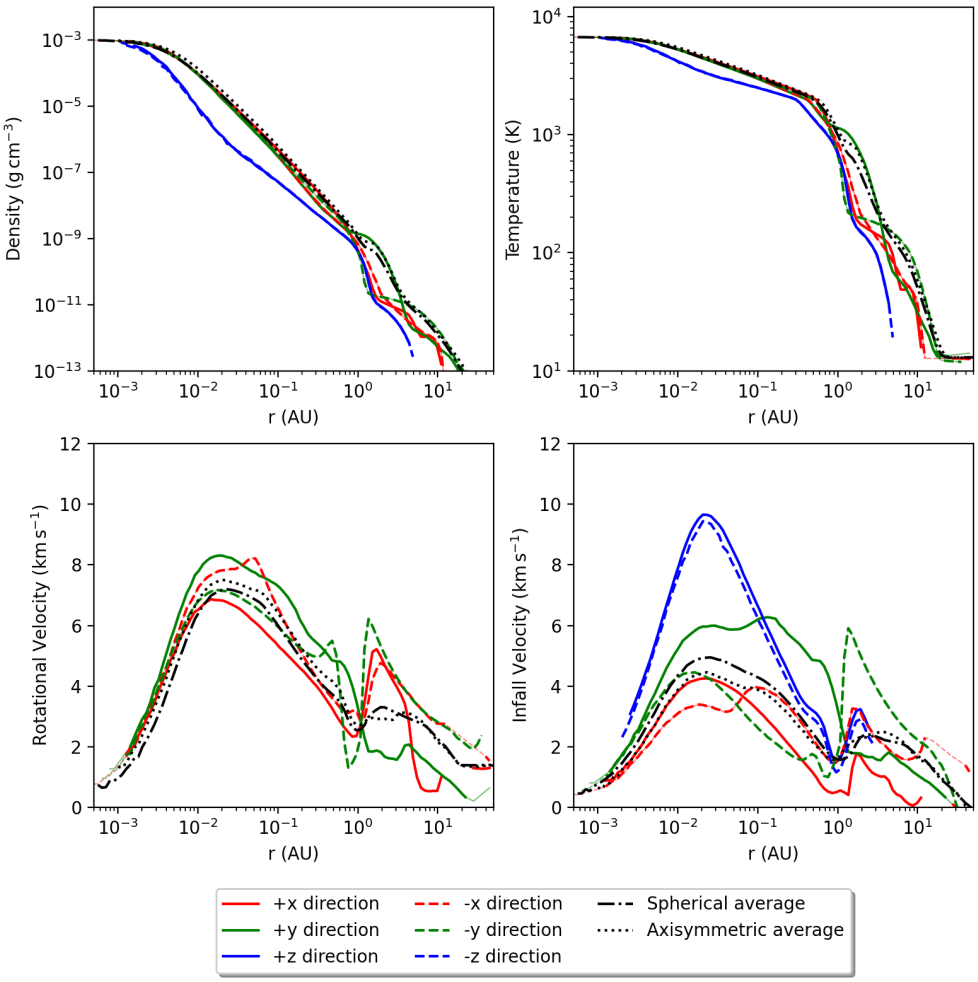

Figure 5.13: Same as in Figure 5.10 but for fragment F4.

The edges of the first and second cores in the ±x and ±y directions, as indicated by the positions of the peaks in the infall velocity profiles, are very similar (see Figures 5.10-5.13) and so the fragments can be assumed to be axisymmetric. The z component of the infall velocity however does show a distinguishable difference, indicating that the fragments are smaller in the z direction. For the remainder the analysis I assume that the fragments are roughly axisymmetric and compare their radial structure with their vertical structure. In Figure 5.14 I compare the structure

of the four fragments that formed in the benchmark run. Panels a) - d) in Figure 5.14 show the axisymmetric average (solid lines), averages along the ±z direction (dotted lines) for the density, temperature, rotational velocity and infall velocity as functions of the distance from the centre of the fragment. The infall velocity in the vertical z direction is larger than in the radial x-y plane. This suggests that the fragments accrete large amounts of material via polar inflows (see Tanigawa, Ohtsuki & Machida (2012)). Panels e) and f) show the spherically averaged (dashed lines) mass and energy ratios as functions of the distance from the centre of the fragment. The inner boundary of the first core is closer to the centre of the fragment in the z direction than it is in the radial direction on the x-y plane. This shows that the fragment is flattened in the z direction. This means that the fragments are oblate spheroids rather than being spherical as assumed in previous studies (Mercer & Stamatellos, 2020; Stamatellos et al., 2007).

The temperature at the centre of the fragment is high (around 6000 - 7000 K) and so the thermal energy dominates over the gravitational energy. This is shown in the upper set of lines in panel f), where, in the inner region disc, the value of α (ratio of thermal to gravitational energy) increases dramatically. α remains fairly constant at $\alpha \sim 0.5 - 0.6$ outside of the second core with a small kink around the vicinity of the inner boundary of the first core. The gravitational energy dominates over rotational energy as shown by the values of β, (between 0.01 and 0.1). F3 and F4, represented by the red and green lines, respectively, have slightly higher rotational velocity around the vicinity of the second core, as shown in panel c) and in panel f) where, as a result of the higher rotational velocity, the value of β is higher than in F1 and F2.

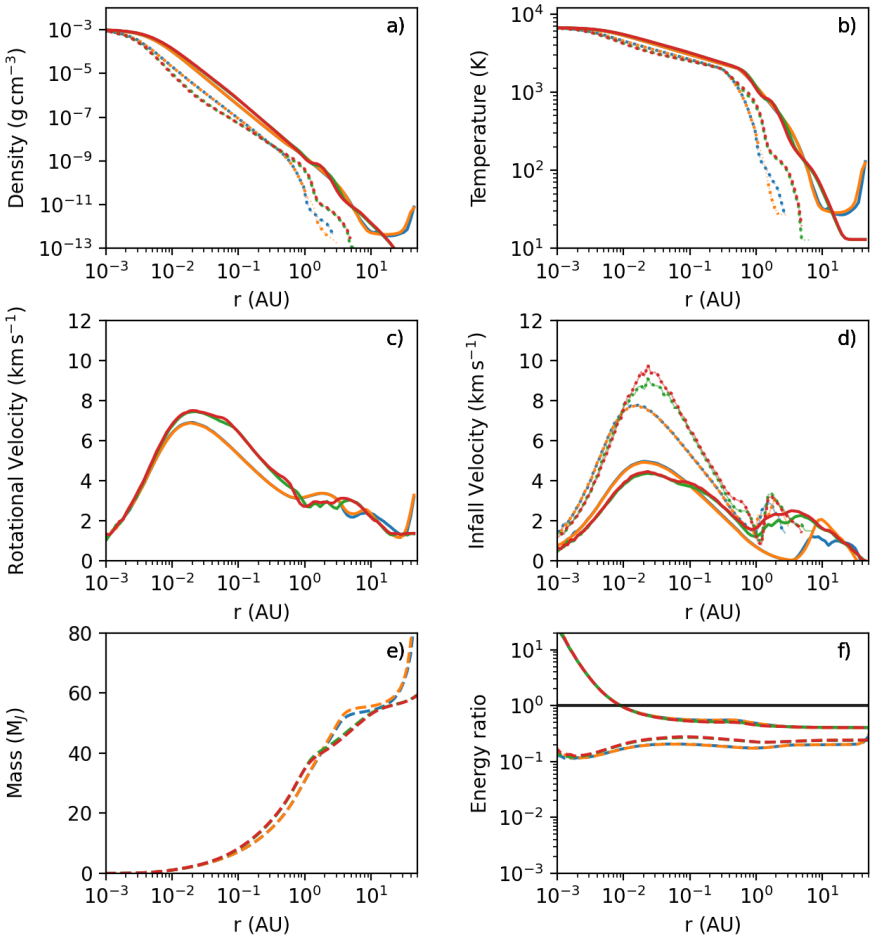

Figure 5.14: Radial (x-y plane; solid lines) and vertical (z; dotted lines) components of the density, temperature, rotational velocity and infall velocity for the fragments that form in the benchmark simulation when their central densities reach $\rho_c = 10^{-3}$g cm^{-3}. Panel e) shows the mass as a function of distance from the centre of the fragment. Panel f) shows the energy ratios $\alpha = E_{therm}/E_{grav}$ (top set of lines) and $\beta = E_{rot}/E_{grav}$ (bottom set of lines). The data in these two panels is spherically averaged. Fragments F1, F2, F3 and F4 are represented by the blue, orange, green and red lines, respectively.

5.4 Fragment Properties

5.4.1 General Properties

Tables 5.2, 5.3 and 5.4 show the properties of the second core and the first core. The time taken for the fragments to evolve from central densities of $\rho_c = 10^{-9}\mathrm{g\,cm^{-3}}$ to $\rho_c = 10^{-3}\mathrm{g\,cm^{-3}}$ is given by Δt_c. Values are given at the locations of the hydrostatic cores along the radial distance R on the x-y plane and the vertical distance z. R and z and are labelled accordingly in the superscript of the quantity.

Table 5.2: Properties of the second core in both vertical z and R (radial on the x-y plane) directions. Δt_c is the time taken for the fragment to evolve from $\rho_c = 10^{-9}$ to $\rho_c = 10^{-3}\mathrm{g\,cm^{-3}}$. $\mathrm{R_{sc}^R}$ is the radius of the second core in the R and z directions, as indicated by the superscripts. The mass and specific angular momentum of the second core are given by $\mathrm{M_{sc}}$ and $\mathrm{L_{sc}}$. α_{sc} and β_{sc} are the the energy ratios $\alpha_{sc} = E_{therm}/E_{grav}$ and $\beta_{sc} = E_{rot}/E_{grav}$. The number of particles contained within the second core is given by N_{sc} and a is the distance of the fragment from the central star.

ID	Δt_c	$\mathrm{R_{sc}^R}$	$\mathrm{M_{sc}}$	$\mathrm{L_{sc}}$	α_{sc}	β_{sc}	$\mathrm{R_{sc}^z}$	$\mathrm{N_{sc}}$	a
-	(yr)	(AU)	($\mathrm{M_J}$)	($\mathrm{cm^2\,s^{-1}}$)	-	-	(AU)	-	(AU)
F1	377	0.021	2.2	9.2×10^{17}	0.70	0.20	0.016	1.4×10^4	59
F2	374	0.020	2.2	8.9×10^{17}	0.71	0.19	0.016	1.4×10^4	55
F3	11	0.023	2.6	1.4×10^{18}	0.67	0.24	0.024	1.7×10^4	245
F4	10	0.023	2.6	1.4×10^{18}	0.66	0.25	0.023	1.7×10^4	245

Table 5.3: Properties of the first core in both z (vertical) and R (radial on the x-y plane) directions. Variables are the same as in Table 5.2 but for the first core with properties calculated at the inner boundary of the first core.

ID	$R^{R}_{fc,i}$	$M_{fc,i}$	$L_{fc,i}$	$\alpha_{fc,i}$	$\beta_{fc,i}$	$R^{z}_{fc,i}$	$N_{fc,i}$	a
-	(AU)	(M_J)	($cm^2\,s^{-1}$)	-	-	(AU)	-	(AU)
F1	3.40	50	1.3×10^{20}	0.42	0.20	0.97	3.2×10^5	59
F2	3.40	51	1.4×10^{20}	0.41	0.20	0.93	3.3×10^5	55
F3	0.97	34	4.1×10^{19}	0.46	0.23	1.20	2.2×10^5	245
F4	0.87	33	3.7×10^{19}	0.46	0.23	1.20	2.1×10^5	245

Table 5.4: Properties of the first core in both z (vertical) and R (radial on the x-y plane) directions. Variables are the same as in Table 5.2 but for the first core with properties calculated at the outer boundary of the first core.

ID	$R^{R}_{fc,o}$	$M_{fc,o}$	$L_{fc,o}$	$\alpha_{fc,o}$	$\beta_{fc,o}$	$R^{z}_{fc,o}$	$N_{fc,o}$	a
-	(AU)	(M_J)	($cm^2\,s^{-1}$)	-	-	(AU)	-	(AU)
F1	7.1	54	2.2×10^{20}	0.41	0.20	1.6	3.4×10^5	59
F2	9.3	56	2.6×10^{20}	0.41	0.19	2.0	3.5×10^5	55
F3	4.8	48	1.5×10^{20}	0.42	0.24	1.6	3.0×10^5	245
F4	3.5	44	1.1×10^{20}	0.42	0.25	1.6	2.8×10^5	245

Figure 5.15 shows the properties of the first and second core of fragments that form in the benchmark run. The dependence of the mass on the radius of the second core is shown in the the upper left panel. All four of the fragments have second core masses well below the planetary threshold of $13\,M_J$, above which an object is considered a brown dwarf. As discussed in the previous section, the fragments are best described as oblate spheroids and so have smaller second core radii in the z direction than they do in the radial direction on the x-y plane, R (see Tables 5.2, 5.3 and 5.4). I will use the extent of the fragment in the R direction when calculating its mass as there is little gas above the mid-plane and its contribution can be neglected. The second core radii range from $\sim$3.5 - $5.5\,R_J$ which is consistent with the findings

of Mercer & Stamatellos (2020). The masses contained within the inner and outer boundaries of the first core are shown in the upper right and lower left panels of the figure, respectively. The distance between the inner and outer boundaries of the first core, i.e. the accretion shock width, is shown as a function of the specific angular momentum of the core in the lower right panel. Fragments that have higher specific angular momentum tend to have a wider accretion shock.

5.4.2 Fragment Properties as a Function of the Distance from the Central Star

The properties of the first and second cores are shown in Figures 5.16 and 5.17, respectively as functions of distance a from the central star. The mass of the first core (see the top panel of Figure 5.16) is larger for fragments farther away from the the star. The second and third panels in Figure 5.16 show the radius of the inner edge of the first core and the width of the accretion shock, respectively. The values calculated in the radial direction on the x-y plane are indicated by the black points and those in the vertical z direction are shown by the red points. The radius of the first core in the radial direction on the x-y plane is smaller for the fragments on wide orbits and they also have a narrower accretion shock. Though, as discussed previously, the specific morphologies of these fragments farther away from the star may have been affected by their violent formation. The final panel in Figure 5.16 shows the specific angular momentum of the first core as a function of the distance from the central star. This indicates that the specific angular momentum of the fragments closer to the star is higher than that of fragments in the outer regions.

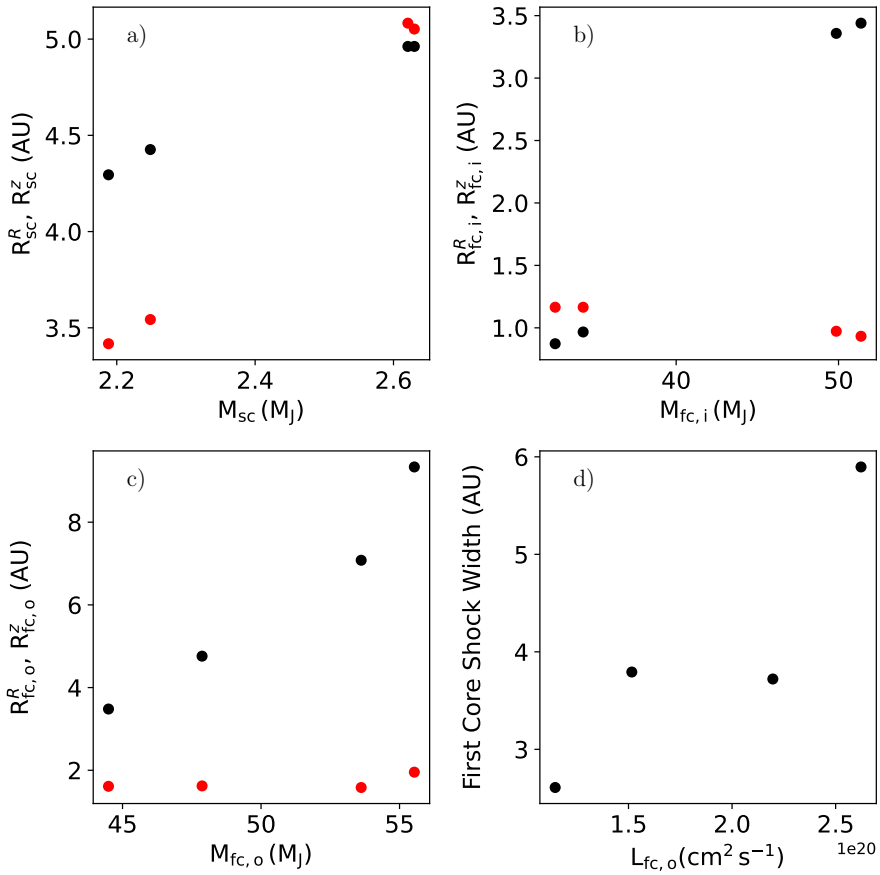

Figure 5.15: The properties of the fragments that formed in the benchmark run. The axis label symbols are defined in Tables 5.2, 5.3 and 5.4. Panel a) shows the radius of the second core in the radial direction R along the x-y plane (black points) and the vertical z direction (red points) as a function of the mass of the second core. Panels b) and c) show the radii of the inner and outer boundary of the first core, respectively and panel d) shows the width of the accretion shock around the first core in the radial direction on the x-y plane as a function of the specific angular momentum of the first core are its outer edge. I calculate the accretion shock width as $R_{\rm fc,o} - R_{\rm fc,i}$.

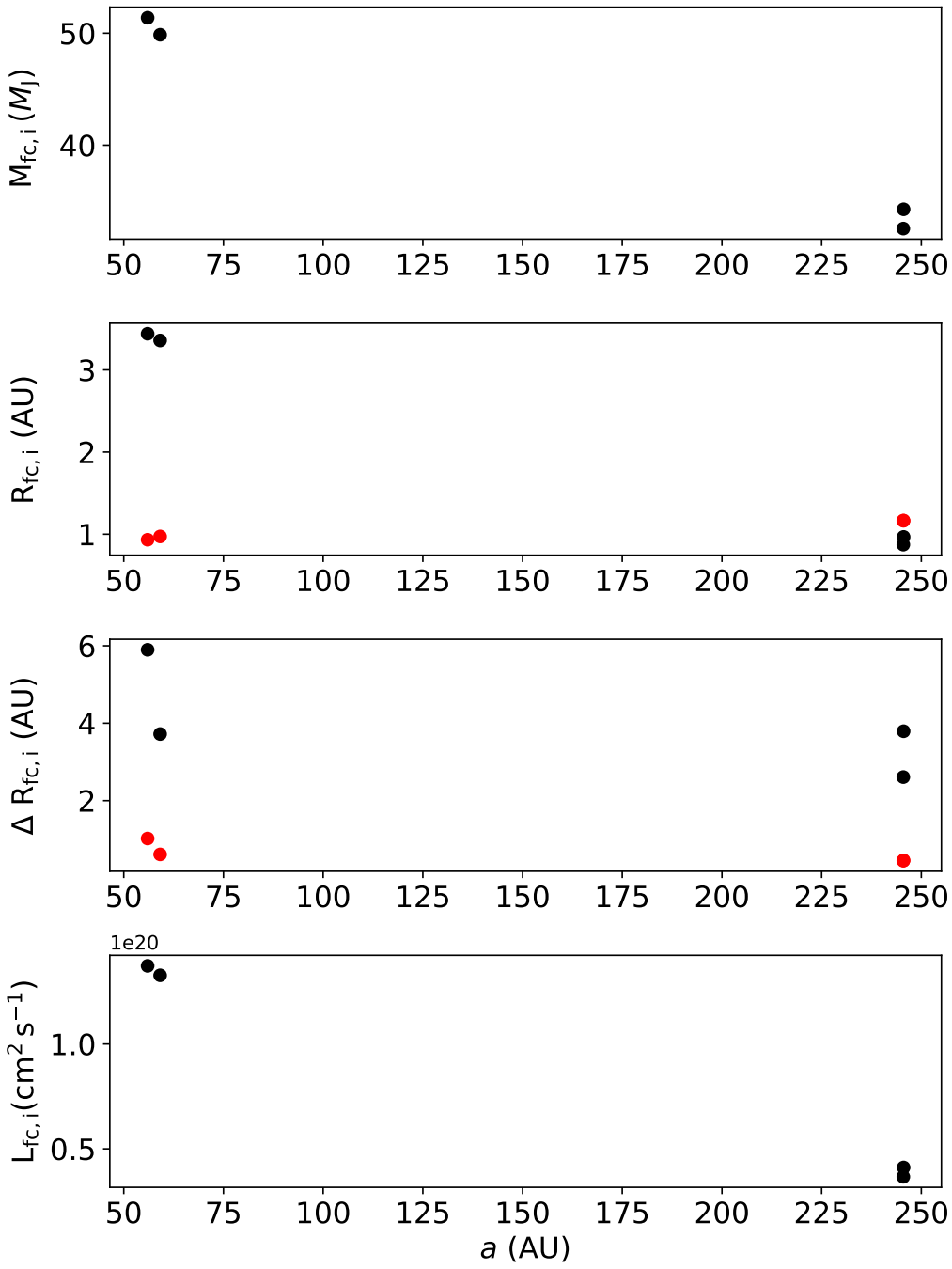

Figure 5.16: The mass, radius, accretion shock width and specific angular momentum of the first core, evaluated at the inner boundary of the first core (top to bottom). The black points show the values calculated in the radial direction on the x-y plane and the red points show those in the z direction. Symbols are defined in Tables 5.3 and 5.4

The second core masses for all four fragments, shown in the top panel of Figure 5.17, show a smaller spread than the first core masses. Fragments that form on wider orbits have second core masses that are only $\sim 0.4\,\mathrm{M_J}$ greater than those that form on shorter orbits. This dependence of the mass of the second cores on distance from the central star is the reverse of what is seen in the case of the first core where the mass decreases with radius. However, as the outer fragments formed by merger events, their mass may be higher than average for fragments forming in those regions due to the combination of two (or more) regions of high density gas. The radius of the second core in the radial direction on the x-y plane is similar for all fragments irrespective of their position in the disc, increasing only by $\sim 0.002\,\mathrm{AU}$ for fragments on wide orbits. The radius of the second core in the z direction increases to a greater degree with fragments on shorter orbits having second cores with radii $\sim 0.01\,\mathrm{AU}$ smaller than those further out. The specific angular momentum of the second core in the radial direction on the x-y plane is plotted as a function of distance from the star in the lower panel of the figure. The fragments on wide orbits, those that have more massive and slightly larger second cores, have higher specific angular momentum.

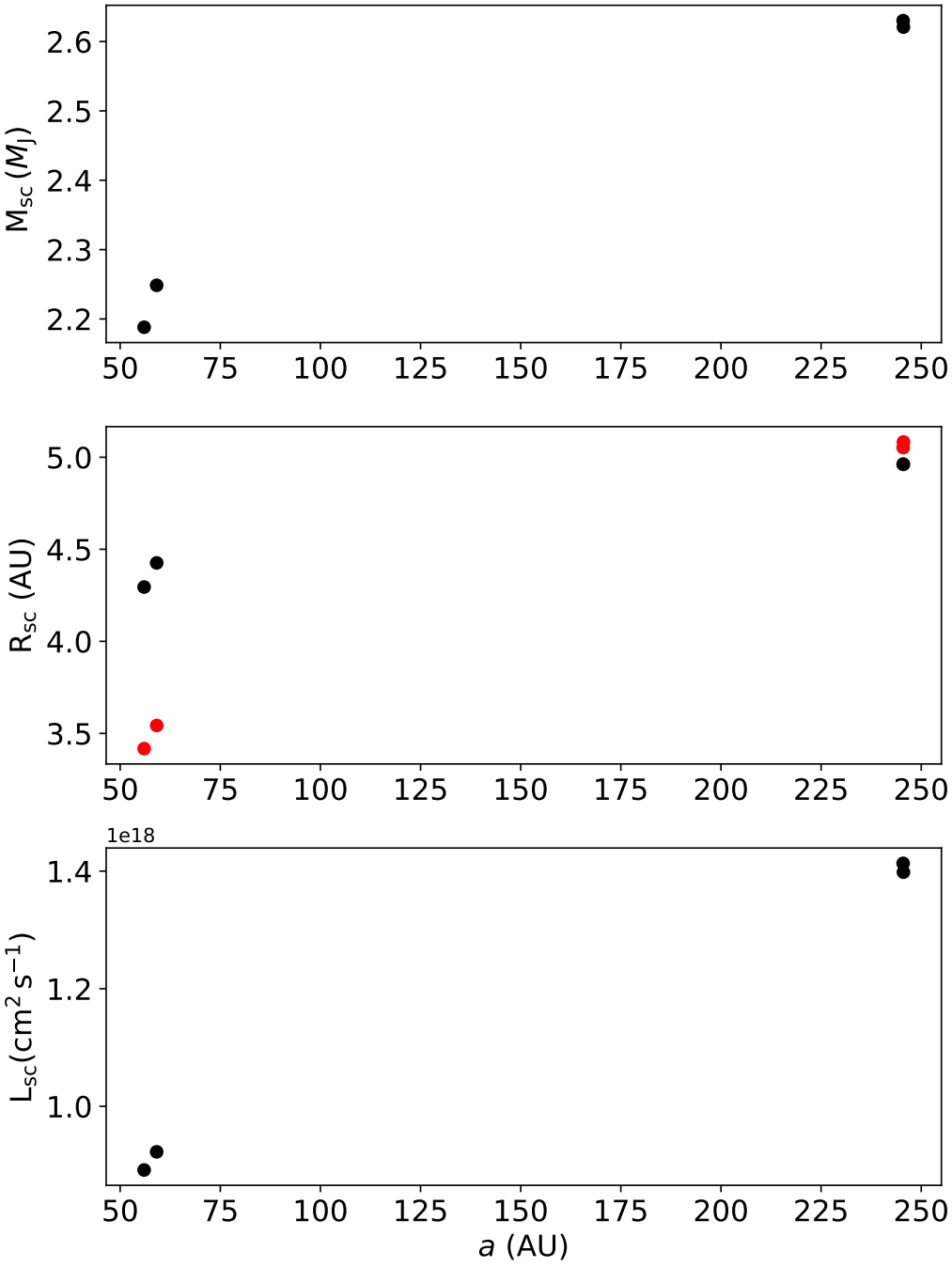

Figure 5.17: The mass, radius and specific angular momentum evaluated at the second core of the fragments that formed in the benchmark run (top to bottom). As in Figure 5.17, the black and red points correspond to the values in the radial direction on the x-y plane and z direction, respectively. Symbols are defined in Table 5.2.

5.4.3 The Shape of Fragments

The density along the vertical z direction of a fragment is much smaller than the corresponding density in the radial direction on the x-y plane R, and so the fragment can be considered flattened. I calculate the aspect ratio e of a fragment by calculating the fiducial extent of the fragment in the z direction, using the position where the density is $\rho_{\rm c} = 10^{-9}{\rm g\,cm^{-3}}$, and dividing that over the corresponding extent in the radial direction on the x-y plane (calculated at the same density). This ratio is plotted in green in Figure 5.18.

The first core, as defined by the minima of the infall velocity profile (i.e. by the accretion shock) is asymmetric; generally speaking the accretion shock in the radial direction on the x-y plane is at larger distance from the centre of the fragment than that in the vertical z direction, but this is not always the case. I calculate the ratio of the size of the first and second cores in the z-direction over that in the radial direction on the x-y plane, and define these as $e_{\rm fc,i}$ and $e_{\rm sc}$ which correspond to the black and red points in Figure 5.18. (I use the inner boundary of the first core for this calculation).

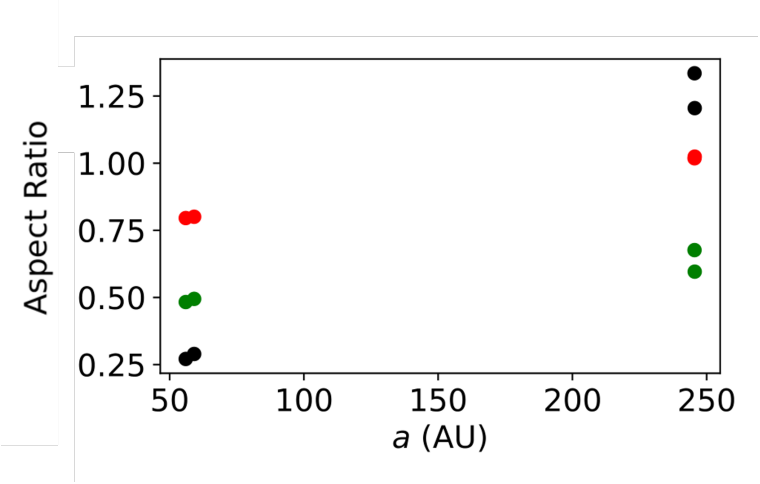

Figure 5.18: The aspect ratios for the four benchmark fragments as a function of their distance from the central star a. The black, red and green points correspond to $e_{\mathrm{fc,i}}$, e_{sc} and e, respectively.

Of the four fragments in the benchmark run, the two that form closer the central star have lower aspect ratios. This suggests that the degree to which a fragment is 'flattened' in the z direction is dependant on its position in the disc. The formation history of the fragments also has a lasting effect on their final morphology. Those that form as a result of mergers have a wider spread of aspect ratios than those that formed on a longer timescale via a more gradual accumulation of mass. The aspect ratios for the second cores in fragments that form at large radii are very close to unity, indicating that the second core is approximately spherical for these fragments. In Figure 5.19 I plot the aspect ratios as a function of their corresponding specific angular momentum. Fragments with higher specific angular momentum have smaller first core aspect ratios. This is clear in the lower panel of the figure.

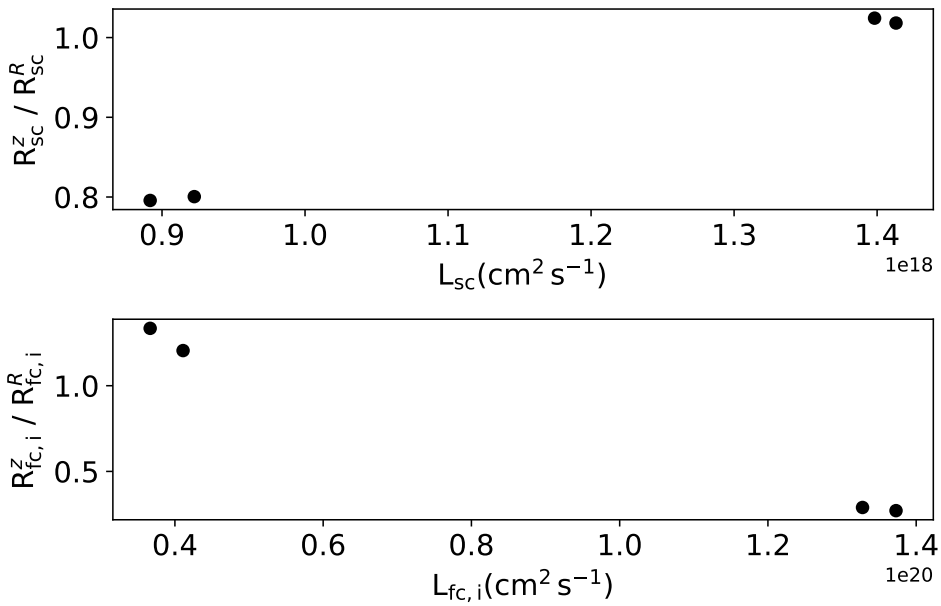

Figure 5.19: Aspect ratios for the second cores and inner boundaries of the first cores as functions of the specific angular momentum for all four fragments. Symbols are defined in Tables 5.2 and 5.3.

5.4.4 Fragment Evolution

I plot the time a fragment takes to evolve from a central density of $\rho_c = 10^{-9}\mathrm{g\,cm^{-3}}$ to $\rho_c = 10^{-3}\mathrm{g\,cm^{-3}}$ as a function the distance from the central star (Figure 5.20; left) and as a function of the specific angular momentum evaluated at the outer boundary of the first core (Figure 5.20;right). Fragments that are formed further out evolve faster in this specific run but this is probably due to those fragments forming due to a collision of proto-fragments. I will re-examine this in the following chapter using a larger ensemble of fragments. Fragments with longer evolution times have higher specific angular momentum, indicating that the formation of the second core may be delayed in these objects as suggested by Mercer & Stamatellos (2020). Though, as noted, the evolution of fragments F3 and F4 is accelerated owing to the merging of two established high density regions of gas.

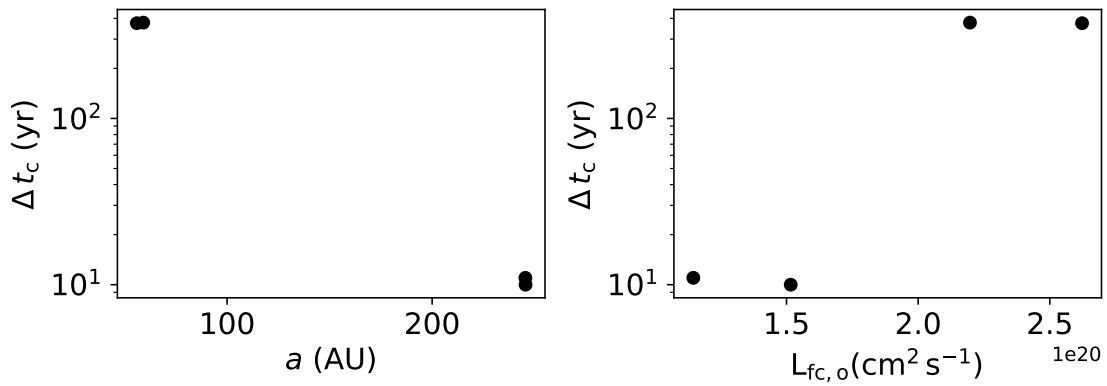

Figure 5.20: The time taken for the fragment to evolve from central densities of $\rho_c = 10^{-9}$g cm^{-3} to $\rho_c = 10^{-3}$g cm^{-3} as a function of the specific angular momentum of the first core, evaluated at its outer boundary.

5.5 Summary

In this chapter I have discussed the formation and evolution of the fragments in the benchmark run. The formation history and general morphology of the fragments are discussed in Section 5.1. I discuss the properties of the fragments by first assuming spherical symmetry in Section 5.2 where the identification of the first and second cores is discussed. In this section I also describe the existence of an inner and outer boundary of the accretion shock around the first core which are used throughout the remainder of the chapter as a point of comparison across all fragments. Finally, in Section 5.3, I introduce the 3 dimensional structure of the fragments by calculating their properties along the ±x, ±y and ±z directions. I find that the ±x and ±y profiles are very similar, meaning that the fragments can be treated as axisymmetric but the structure in the vertical z direction differs significantly from that in the radial x-y direction. The infall velocity in the region around the second core is much larger along the vertical z direction than it is in the radial x-y direction, suggesting that the accretion on the the second core occurs mostly through polar inflows. In Section

5.4 I discuss and compare the axisymmetric and vertical properties of the fragments. I calculate aspect ratios for the second core and inner boundary of the first core and also define an additional aspect ratio determined by the density profile in the radial direction on the x-y plane and the vertical z direction. I find that the fragments are oblate spheroids rather than spherically symmetric as previously assumed (Mercer & Stamatellos, 2020; Stamatellos et al., 2007).

Chapter 6

The Effect of Thermodynamics on the Properties of Disc–Instability Planets

In Chapter 5, the formation and evolution of fragments was discussed in the context of the benchmark simulation. This simulation was performed to provide a basis for comparison to the fragments that form in discs where the thermodynamics are varied as per the values in Table 4.1. In the following chapter, I will present the analysis that has been performed on these fragments and compare them to those that formed in the benchmark simulation.

6.1 General Properties

In most cases, when cooler discs fragment, they result in the formation of more fragments than in hotter discs. This is to be expected as disc temperature is linked to the stability of a disc. A cooler disc is gravitationally unstable over a larger region meaning that, in addition to a greater number of fragments, I also expect fragments

to form over a greater spatial range. Generally, with the exception of morphological inconsistencies caused by merger events, fragments whose thermodynamics are controlled by shallower equations of state result in shallower density profiles.

During the isothermal collapse phase, the fragments are optically thin and so the energy generated as a result of the collapse is readily radiated away. If the isothermal collapse phase is extended, then the disc remains at a low temperature for longer. This provides greater opportunity for fragmentation to occur. In runs 9 - 16, the divergence from isothermality occurs at a higher density than their counterparts in runs 1 - 8 (see Table 6.1) and so I expect the discs whose thermodynamics are determined by these equations of state to produce more fragments.

The equations of state in runs 5, 6, 13 and 14 have very steep first adiabatic zones, see Figure 4.5, and so the temperature at the centre of the fragment increases very rapidly. This means that the temperature at its centre reaches that which is required of hydrogen dissociation at a relatively low density. The opposite is true for runs 7, 8, 15 and 16. The EOS in these runs is very shallow, see Figure 4.5, and so the temperature increase with density is lower than in other equations of state. Indeed, the temperature at the centre of the fragments does not reach that required to trigger the dissociation of hydrogen and so the second core does not form.

6.2 The Effect of the EOS on the Structure of Fragments

Table 6.1 reiterates the parameters used in the specific equations of state, as listed in Table 4.1, with the number of fragments that formed in each run. The runs listed in the table are each part of a pair, differing only in the reference temperature of the disc at 1 AU (see Equation 4.5 (e.g. Run 1 and Run 2 use the same equation of state, but $T_{1\,AU} = 200\,K$ and $150\,K$, respectively). In this section, I will discuss the

equations of state as pairs and the effect of the value of $T_{1\,AU}$ has on the formation and evolution of the fragments where appropriate. In the benchmark run, a 3 - stage barotropic equation of state is used whereas in the following equations of state, I use a 2 - stage EOS, i.e. $\gamma_1 = \gamma_2$. The decision was made in order to limit the parameter space; as, shown by the evolution of a collapsing cloud using a realistic treatment of radiative transfer in Figure 2.2, the change in adiabatic index in small.

Table 6.1: The different equations of state explored in this work, as discussed in Chapter 4. The number of fragments that reached central densities of $\rho_c = 10^{-3} \mathrm{g\,cm^{-3}}$ in each run is given by the N_f. Other symbols are the same as those in Table 4.1.

Run ID	N_f	$\rho_1\,(\mathrm{g\,cm^{-3}})$	$\rho_2\,(\mathrm{g\,cm^{-3}})$	$\rho_3\,(\mathrm{g\,cm^{-3}})$	γ_1	γ_2	γ_3	$T_{1\,AU}(K)$
Benchmark	4	1×10^{-13}	3.27×10^{-12}	5.86×10^{-9}	1.66	1.4	1.1	200.0
Run 1	25	1×10^{-13}	3.16×10^{-11}	5.66×10^{-8}	1.4	1.4	1.1	200.0
Run 2	28	1×10^{-13}	3.16×10^{-11}	5.66×10^{-8}	1.4	1.4	1.1	150.0
Run 3	2	1×10^{-13}	3.27×10^{-12}	3.06×10^{-10}	1.66	1.66	1.1	200.0
Run 4	1	1×10^{-13}	3.27×10^{-12}	3.06×10^{-10}	1.66	1.66	1.1	150.0
Run 5	0	1×10^{-13}	1.78×10^{-12}	7.52×10^{-11}	1.8	1.8	1.1	200.0
Run 6	0	1×10^{-13}	1.78×10^{-12}	7.52×10^{-11}	1.8	1.8	1.1	150.0
Run 7	32	1×10^{-13}	1×10^{-8}	3.20×10^{-2}	1.2	1.2	1.1	200.0
Run 8	47	1×10^{-13}	1×10^{-8}	3.20×10^{-2}	1.2	1.2	1.1	150.0
Run 9	17	6×10^{-13}	1.9×10^{-10}	3.39×10^{-7}	1.4	1.4	1.1	200.0
Run 10	28	6×10^{-13}	1.9×10^{-10}	3.39×10^{-7}	1.4	1.4	1.1	150.0
Run 11	9	6×10^{-13}	1.96×10^{-11}	1.84×10^{-9}	1.66	1.66	1.1	200.0
Run 12	13	6×10^{-13}	1.96×10^{-11}	1.84×10^{-9}	1.66	1.66	1.1	150.0
Run 13	4	6×10^{-13}	1.07×10^{-11}	4.51×10^{-10}	1.8	1.8	1.1	200.0
Run 14	2	6×10^{-13}	1.07×10^{-11}	4.51×10^{-10}	1.8	1.8	1.1	150.0
Run 15	45	6×10^{-13}	6×10^{-8}	1.92×10^{-1}	1.2	1.2	1.1	200.0
Run 16	49	6×10^{-13}	6×10^{-8}	1.92×10^{-1}	1.2	1.2	1.1	150.0

6.2.1 Runs 1 and 2

Runs 1 and 2 form 25 and 28 fragments, respectively. The disc is unstable to gravitational fragmentation over a larger spatial range in run 2 due to the lower

temperature and so the increased number of fragments is expected. This is true for most of the EOS pairs (see Table 6.1). Figure 6.1 shows the profiles of representative fragments from run 1 (blue line; hereafter FR1) and run 2 (orange line; hereafter FR2).

The vertical component of the temperature (dotted lines in Figure 6.1) is higher in FR2 than in FR1 the same is true for the vertical density profile. Though, as in the case of the benchmark run, a number of fragments in both run 1 and 2 form by the merging of two 'proto-fragments' and so this may be a result of this violent evolution. FR2 shows a filament, clear in the right hand panel of Figure 6.2, that tethers it to the rest of the disc. This is also shown by the sharp increase in rotational velocity in panel c) of Figure 6.1 and a corresponding increase in the value of β in panel f). Panel d) shows that the infall velocity along the vertical z direction is much higher than in the radial direction on the mid-plane in FR1 and, though it is still higher, the difference is less dramatic in FR2. Indeed, the infall velocity for FR2 in the radial x-y direction is comparable to that in the vertical z direction inside of $\sim 1\,\mathrm{AU}$, illustrating that the accretion onto the second core is approximately spherically symmetric in this case. The mass of the fragments, shown in panel e) of Figure 6.1 are very similar interior to approximately $\sim 0.2\,\mathrm{AU}$. The first core mass of FR1 is approximately double ($\sim 30\,\mathrm{M_J}$) that of FR2. The morphologies of FR1 and FR2 are shown in the left and right hand panels of Figure 6.2, respectively. As discussed above, FR2 shows very clear evidence of the filament tethering it to the surrounding disc and, though its signature in the rotational velocity and infall velocity profiles of Figure 6.1 is weaker, FR1 also displays such a structure at a larger radii from the centre of the fragment.

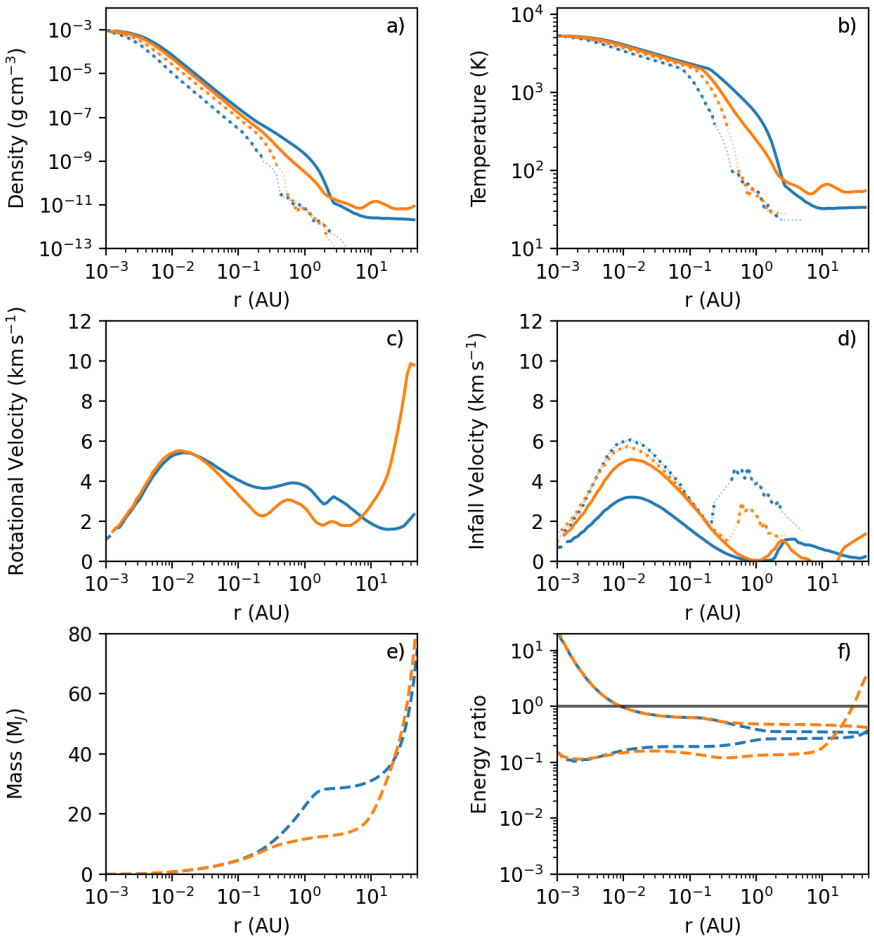

Figure 6.1: Radial (x-y plane; solid lines) and vertical (z; dotted lines) components of the density, temperature, rotational velocity and infall velocity for representative fragments that formed in Run 1 (FR1 ;blue lines) and Run 2 (FR2; orange lines) when their central densities reach $\rho_c = 10^{-3}$g cm^{-3}. Panel e) shows the mass as a function of distance from the centre of the fragment. Panel f) shows the energy ratios $\alpha = E_{therm}/E_{grav}$ (top set of lines) and $\beta = E_{rot}/E_{grav}$ (bottom set of lines). The data in these two panels is spherically averaged. The semi-transparent regions indicate area regions of low, resolution.

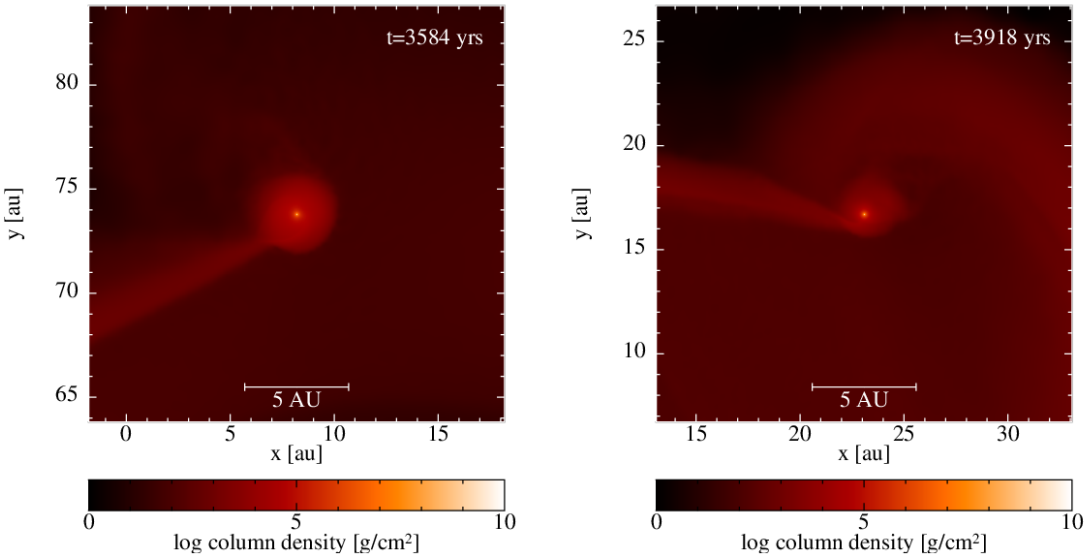

Figure 6.2: Morphologies of representative fragments FR1 and FR2 from run 1 and run 2 (left and right panels, respectively). The stream that tethers the fragments to the rest of the disc is clear in both cases.

6.2.2 Runs 3 and 4

The structure of representative fragments that form in runs 3 and 4, hereafter FR3 and FR4, are shown in Figure 6.3 by the blue and orange lines, respectively. FR3 is one of only two fragments that reach high central densities in run 3 and formed by the merging of a number of 'proto-fragments', resulting in an atypical velocity profile. Despite this difference in formation history, both FR3 and FR4 have very similar density and temperature profiles in the radial direction on the x-y plane out to ∼few AU from the centre of the fragment. There is a variation in the density and temperature of FR3 but this is likely a result of its violent evolution. The rotational and infall velocities of the fragments are high in both cases, particularly compared to the fragments that form in the benchmark run. Indeed, the infall velocity of FR4 along the vertical z direction is the highest of all the representative fragments discussed in this chapter. Its value is double that calculated along the

radial direction on the x-y plane, further suggesting the existence of polar accretion flows through which the fragment accretes mass from the disc. This inflow is likely distorted in the case of FR3 due to the merger event and so there is no evidence of it in panel d) of Figure 6.3. Both fragments have high mass, see panel e) of the figure. The first core masses of FR3 and FR4 are $> 80\mathrm{M_J}$ though the second core masses are below the brown dwarf threshold of 13 $\mathrm{M_J}$. This suggests that the protoplanets (i.e. the second cores) are located at the centre of massive parent clouds from which they may accrete additional mass, possibly later evolving into brown dwarfs. With the exception of in the region close to the centre of the fragments, both FR3 and FR4 have similar values of β, though FR4 has a higher value of α outside of the second core. This suggests that the thermal energy dominates over the gravitational energy outside of this region. This is to be expected for this equation of state as, owing to its relative steepness, the gas in the fragment is at high temperatures at lower densities. This is particularly clear when comparing the temperature profiles in Figure 6.3 with those in Figure 6.1 where, in the latter, the shallower adiabatic region (see Figure 4.5) means that low density gas is cooler.

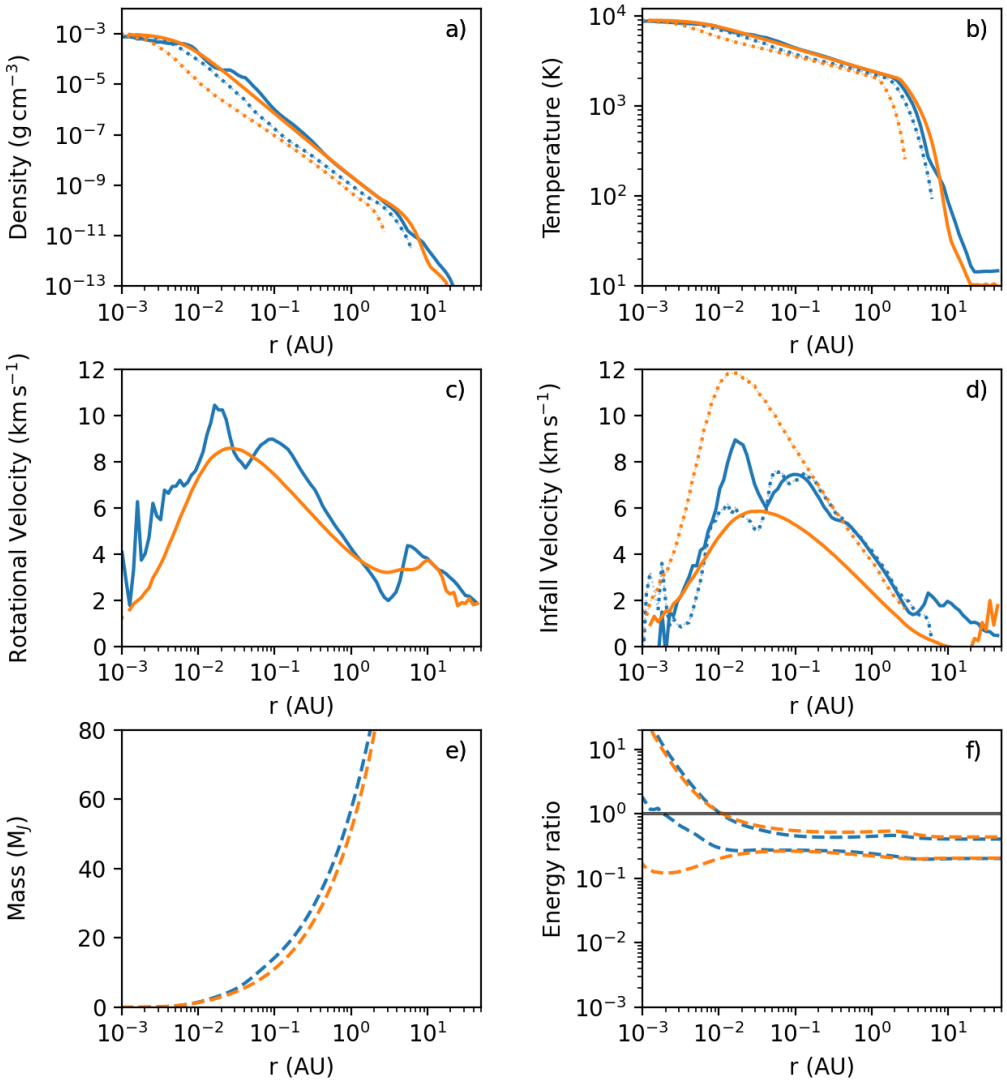

Figure 6.3: Same as Figure 6.1 but for FR3 (blue lines) and FR4 (orange lines).

The morphologies of FR3 and FR4 are shown in the left and right panels of Figure 6.4, respectively. Their atypical shapes are indicative of their violent evolution. FR4 underwent a number of merger events early in its evolution before the central density reached $\rho_c = 10^{-3}$g cm^{-3} and retained a portion of the material from these events

in a halo around the first core.

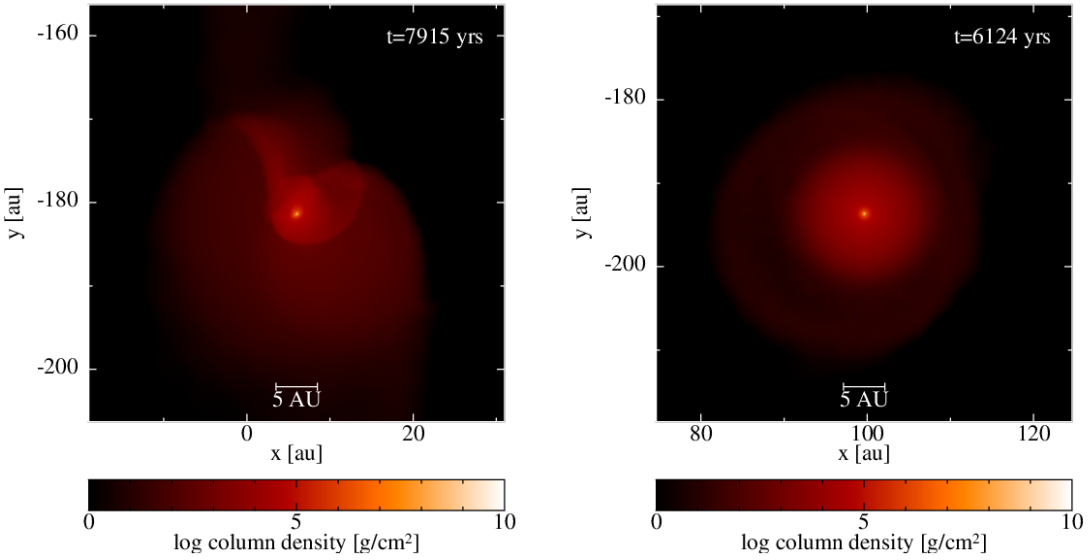

Figure 6.4: Morphologies of FR3 and FR4 when the density at the centre of the fragments reaches $\rho_c = 10^{-3} \mathrm{g\,cm^{-3}}$.

The merger event that contributed to the formation of FR3 not only affects the shape of the first core and the outer regions of the fragment but also that of the second core and its immediate surroundings, this is shown in Figure 6.5. Though the EOS may not effect the specific morphology of the final fragment having undergone a merger event, certain equations of state result in more fragments and so merger events, resulting in fragments similar to FR3, are more common.

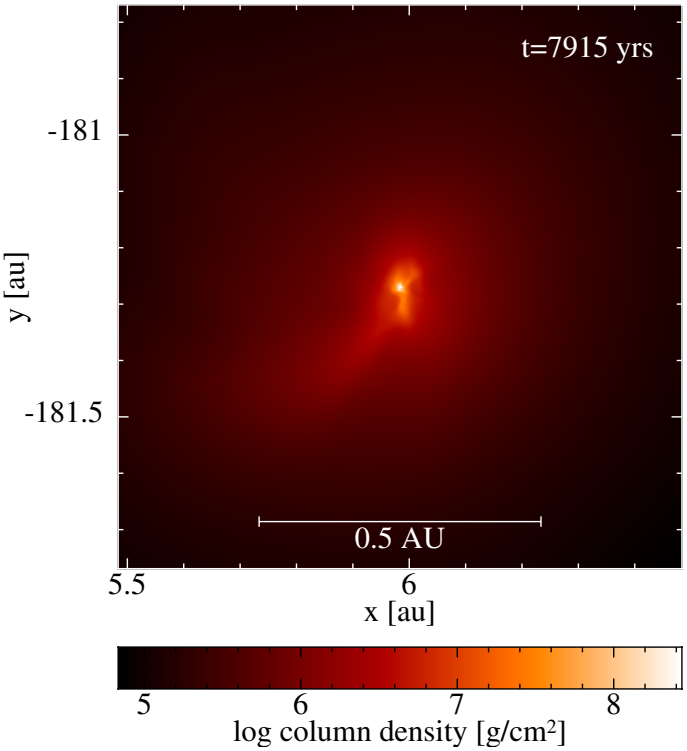

Figure 6.5: The region around the second core of FR3 that formed as a result of a merger event. The violent evolution also effects the morphology of the second core and disrupts the polar accretion flow from which the fragment accretes mass.

6.2.3 Runs 7 and 8

As discussed in Section 6.1, the fragments that form in runs 7 and 8 do not reach the central densities required for hydrogen to dissociate and so the second core does not form. The resolution of the fragments in the vertical z direction is poor in both runs and so the calculation along this component has been omitted. The profiles in panels a) - d) of Figure 6.6 show only the axisymmetric average calculated radially along the x-y plane. As before, panels e) and f) show the spherical average. I have included an additional representative fragment from both runs, equating to 4 fragments in the Figure; FR7-A and FR7-B, indicated by the blue and orange lines, and FR8-A and FR8-B, indicated by the green and red lines, respectively. This is

to illustrate the two different morphological groups that the fragments fall into. In Group A, the fragments show evidence of the first core in the infall velocity profiles in panel d) at $\sim$ few tenths AU from the centre of the fragment and at smaller radii the infall velocity falls to $\sim$ zero. Group B fragments show a peak in the infall velocity at radii of ~ 0.005 AU which I interpret as evidence of the outer boundary of the first core. These fragments tend to have shallower density and temperature profiles, as shown by the orange and red lines in panel a) of the Figure. All four representative fragments in Figure 6.6, despite their morphological differences, have similar rotational velocities (panel d) which gradually reduce at larger radii. The fragments all have lower masses (panel e) than fragments that form in both the benchmark run and the discs whose thermodynamics are determined by steeper equations of state. This is also reflected in the value of β (bottom set of lines in panel f) of the Figure 6.6).

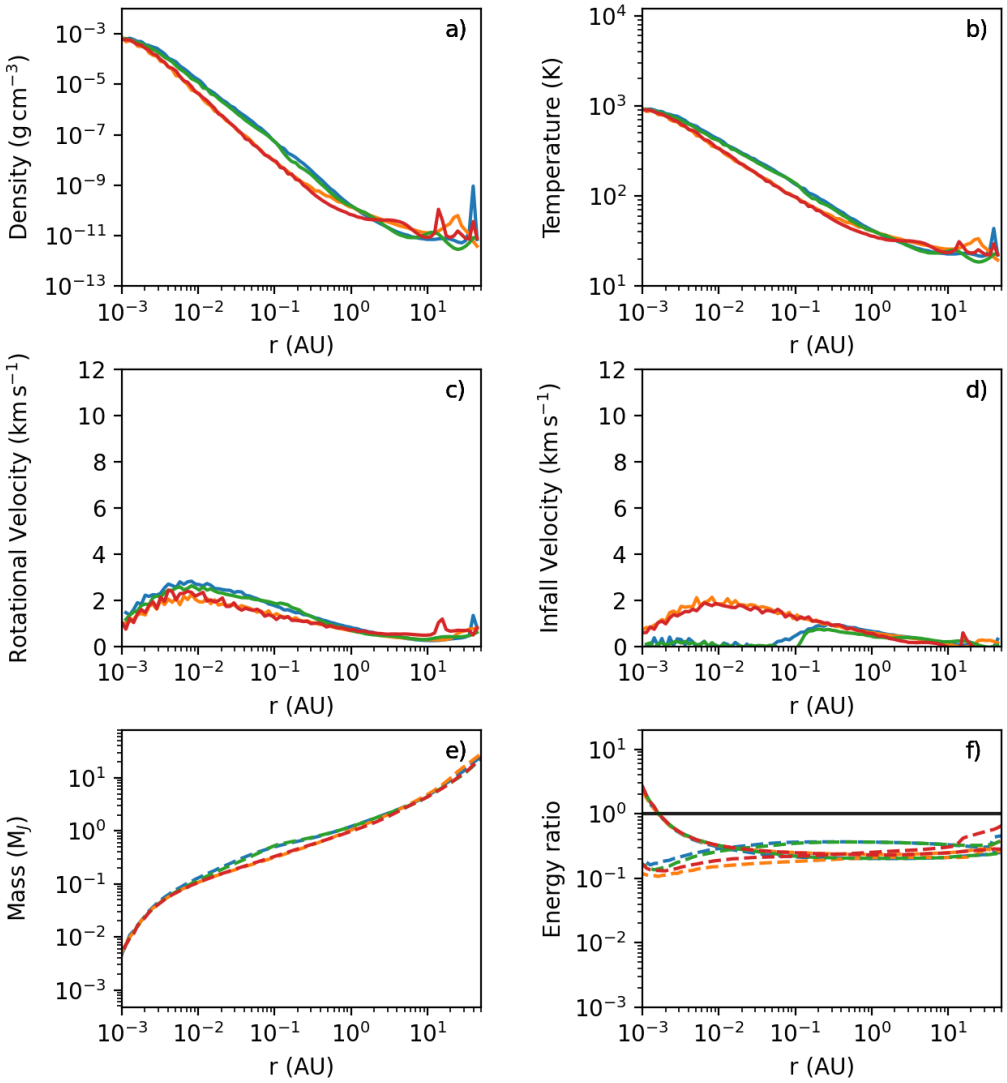

Figure 6.6: Same as Figure 6.1 but for FR7-A (blue lines), FR7-B (orange lines), FR8-A (green lines) and FR8-B (red lines). The mass in panel e) is plotted with a logarithmic scale to highlight the low fragment masses.

The morphologies of the fragments reveal that those that fall into Group A (Figure 6.7; left hand panels), with the peaks in the infall velocity appearing at

larger radii (see Figure 6.6; blue and green lines), have strong spiral features in the material around the dense central core. These spiral are not present in the Group B fragments which are shown in the right hand panels of Figure 6.7. All fragments in Figure 6.7 are far smaller than those that form in the benchmark run. Additionally, the spirals around the Group A fragments are tighter in the run 8 fragments than those in the run 7 fragments.

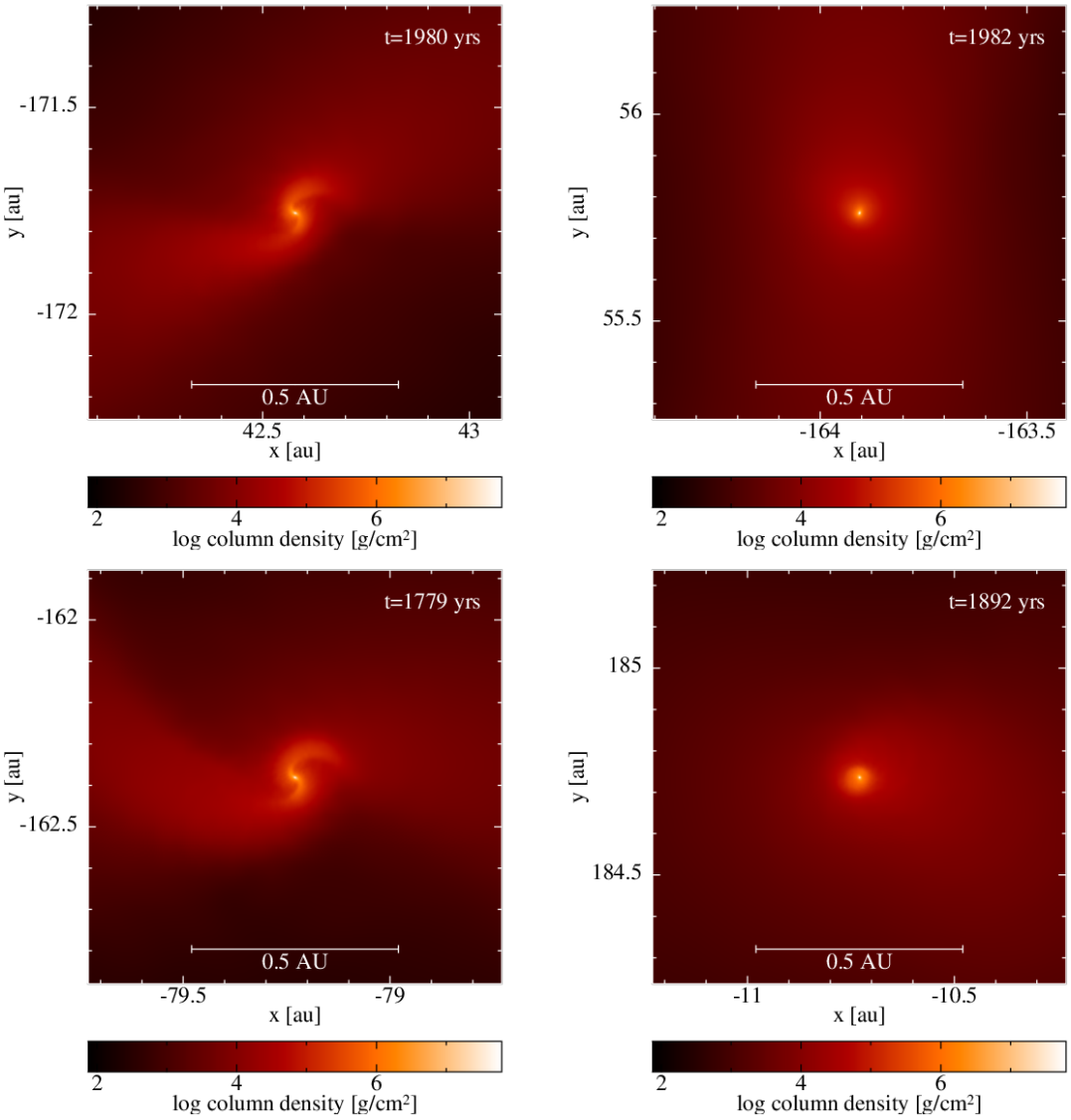

Figure 6.7: Morphologies of the representative fragments in runs 7 (top two panels) and 8 (bottom two panels). Group A fragments are those on the left, Group B are those on the right.

6.2.4 Runs 9 and 10

Runs 9 and 10 differ only from runs 1 and 2 in that the value of ρ_1 is higher for the former. ρ_1 determines the density at which the fragment diverges from isothermality and evolves adiabatically. During isothermal collapse, the temperature at the centre

of the fragment remains constant and so the thermal pressure does not provide sufficient support against gravitational collapse. Therefore, a higher value of ρ_1 means that the collapse occurs on a shorter timescale. At higher densities further evolution is expected to occur on a similar timescale to that in runs 1 and 2 owing to the equations of state sharing the same adiabatic indices. As discussed in §6.1, the onset of adiabaticity at higher densities is linked to a greater number of fragments being formed. Runs 9 and 10 form 17 and 28 fragments respectively, as the cooler disc temperature in run 10 contributes further to the formation of more fragments. The structure of representative fragments from runs 9 and 10 (hereafter FR9 and FR10) are shown in Figure 6.8 by the blue and orange lines, respectively. The peaks in the profiles for FR10 at $\sim 10\,\mathrm{AU}$ are due to this fragment being in close proximity to other fragments and spiral arms in the disc. FR9 and FR10 have similar density structure along the radial direction on the x-y plane within $\sim 0.07\,\mathrm{AU}$, outside of which, the density of FR9 decreases more rapidly. The first core in FR9 is large, the outer boundary of which lies at approximately 10 AU from the centre of the fragment. The infall velocity in the region of the outer boundary of the first core is fairly low when compared to both FR10 and the fragments that formed in the benchmark run. The width of the accretion shock in FR9 is also large, extending across a few AU. This could be a result of the increased specific angular momentum of the fragment which is located on a wider orbit. FR10, located on a shorter orbit, has a relatively narrow accretion shock. This suggests a relationship between the width of the accretion shock the position of the fragment in the disc. Despite these morphological differences, which are also shown in Figure 6.9, both fragments have similar masses for the first and second core (see panel e) of Figure 6.8. Though, due to a higher rotational velocity (panel c)), FR10 has a greater value of β, shown by the bottom set of lines in panel f). The resolution of the fragment in the vertical z direction is poor outside of $\sim 0.1\,\mathrm{AU}$. However, interior to this radius, FR9 and

FR10 show very similar infall velocities. The temperature and density structure of the two fragments displays the expected differences owing to the cooler disc in run 10.

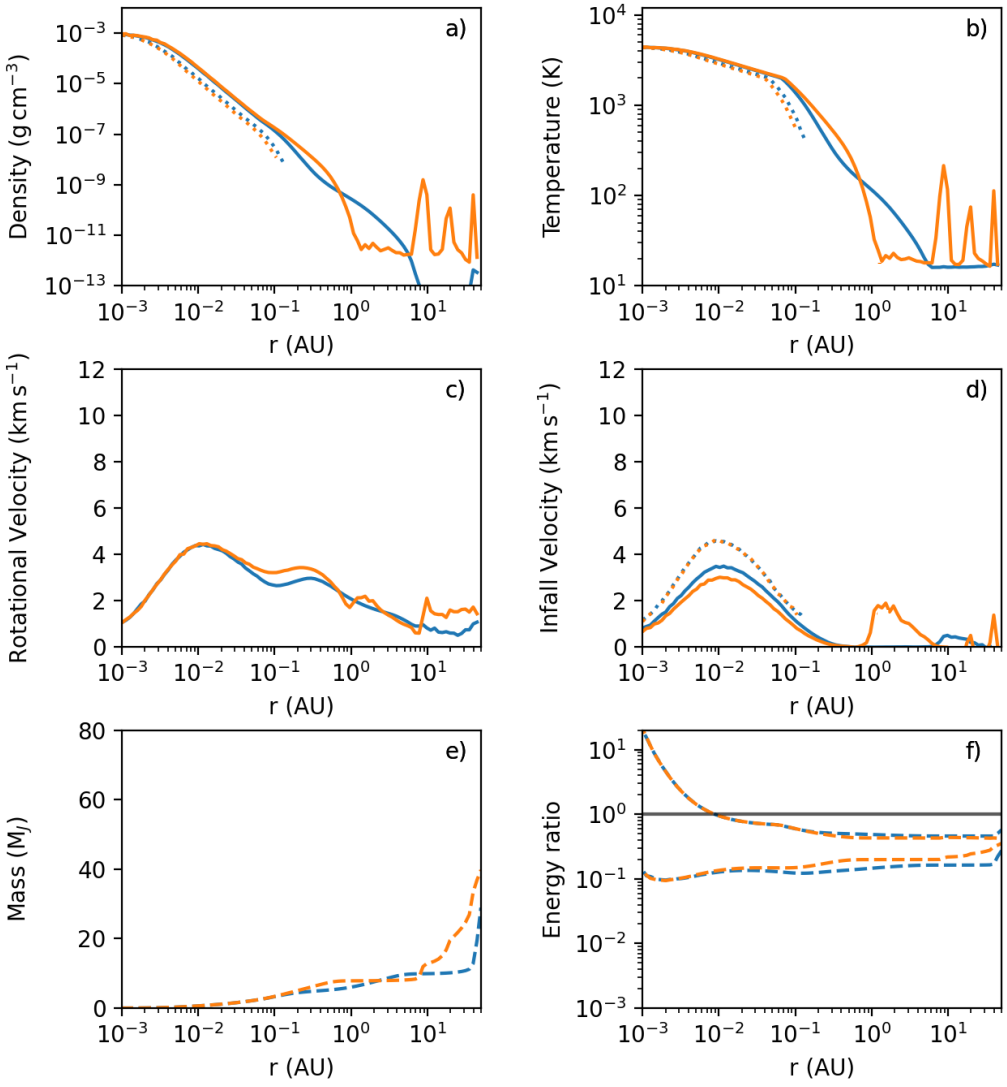

Figure 6.8: Same as Figure 6.1 but for FR9 (blue lines) and FR10 (orange lines).

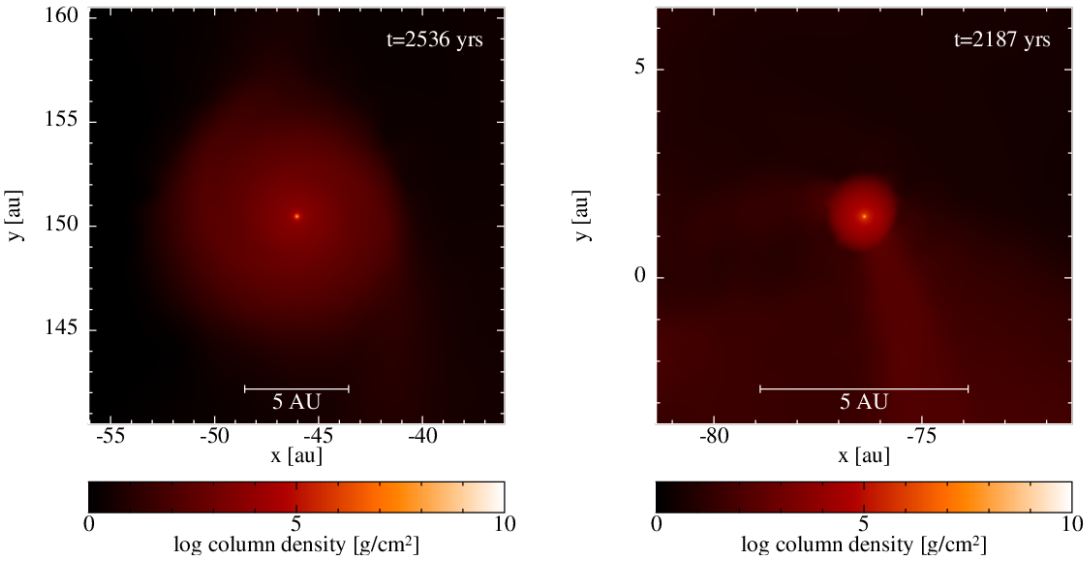

Figure 6.9: The morphologies of fragments FR9 and FR10 (left and right, respectively)

6.2.5 Runs 11 and 12

The fragments that form in runs 11 and 12, FR11 and FR12, shown in blue and orange, respectively in Figure 6.10 have high infall velocities in the region of the second core of similar magnitude to those in the benchmark run but much higher than those in other equations of state such as runs 1 and 2. This high infall velocity along the vertical z direction further suggests the existence of polar accretion flows, through which the second core accretes mass from the disc. The first core is poorly resolved in the vertical z direction in FR11 and FR12 so the vertical infall velocity in this region is difficult to determine. The infall velocity around the outer boundary of the first core in the radial direction on the mid-plane is higher in runs 11 and 12 than it is in runs 1 and 2, leading to a corresponding increase in mass for fragments, shown in panel e).

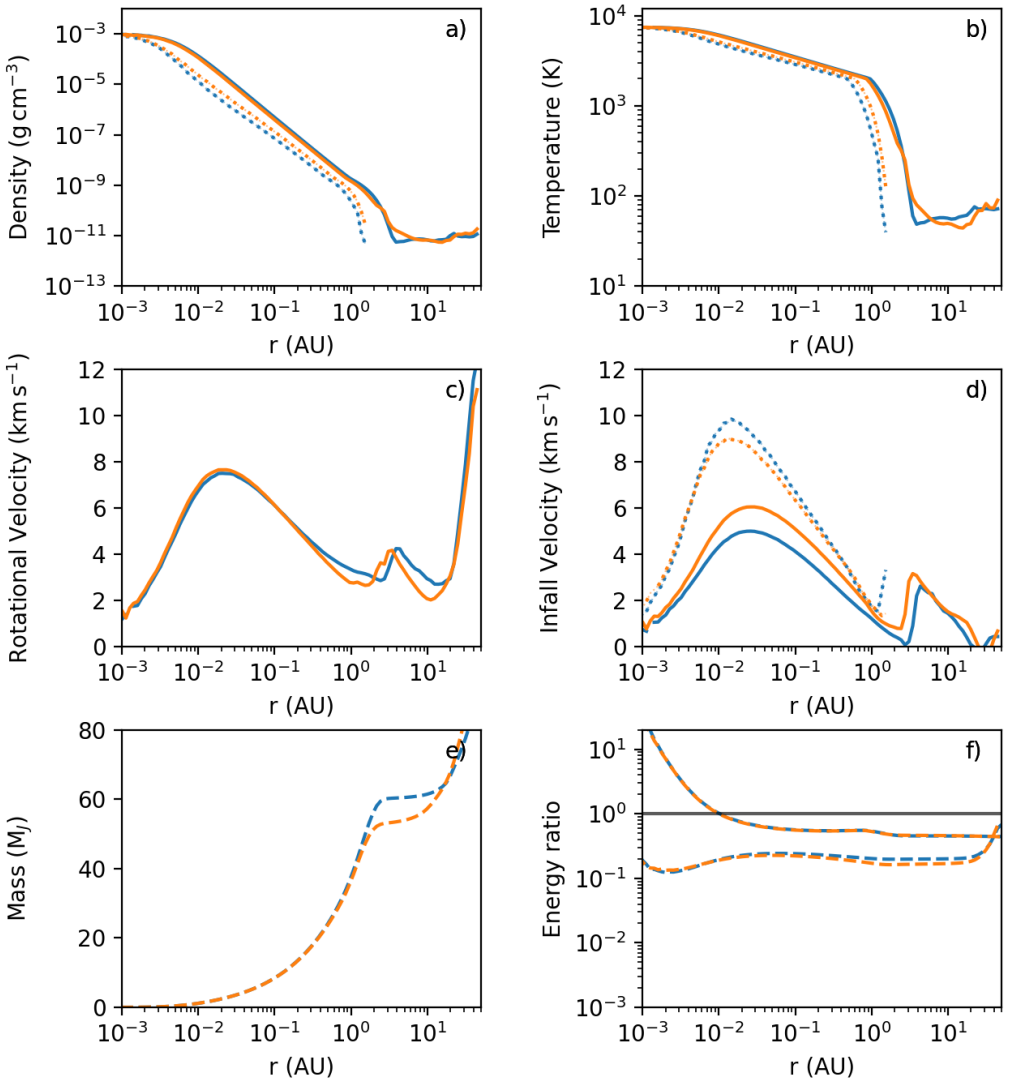

Figure 6.10: Same as Figure 6.1 but for FR11 (blue lines) and FR12 (orange lines).

The morphologies of FR11 and FR12 are shown in the Figure 6.11 (left and right, respectively). Both fragments are larger in scale than those that form in discs whose thermodynamics are determined by shallower equations of state. This suggests that the radius of the fragments, and consequently their mass, depend on the adiabatic

index.

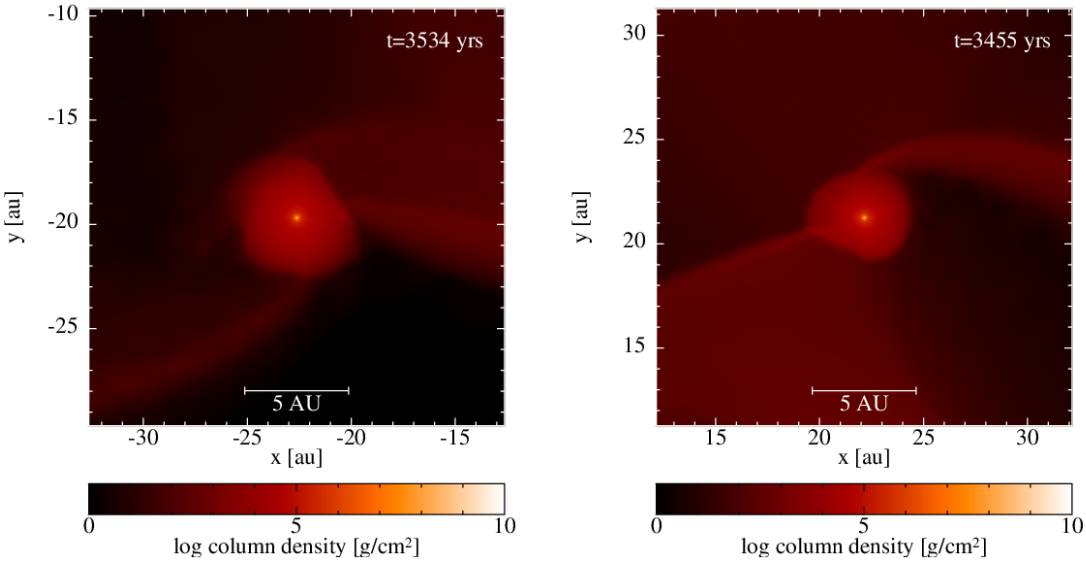

Figure 6.11: Morphologies of FR11 and FR12 when the density at the centre of the fragments reaches $\rho_c = 10^{-3} \mathrm{g\,cm^{-3}}$.

6.2.6 Runs 13 and 14

Runs 13 and 14 are similar to runs 5 and 6 in that they share the same adiabatic indices (see Figure 4.5) though the departure from the isothermal collapse phase occurs at a higher density. This means that only a small number of fragments reach high central densities. Runs 13 and 14 produced only 4 and 3 fragments, respectively. Representative fragments from both runs are shown in Figure 6.12 where FR13 and FR14 and represented by the blue and orange lines, respectively. Both fragments have very similar density and temperature profiles in the radial direction on the x-y plane, despite the difference in disc temperature (see panels a) and b) of Figure 6.12). Additionally, the difference between the density and temperature profiles in the vertical z direction and those in the radial direction on the x-plane is very small, this suggests that, contrary to many other fragments discussed in this chapter, these fragments are approximately spherically symmetric.

The rotational velocities for FR13 and FR14 are very close to one another within a few AU, outside of which they diverge owing to their specific morphologies; the large peak in rotational velocity around FR13 at 20-50 AU is due to its proximity to the centre of the disc and is indicative of the spiral arms on the opposite side of the star. Both FR13 and FR14 have higher infall velocities than the fragments that formed in the benchmark run which, as is the case in runs 3 and 4, is consistent with their high masses, shown in panel e) Figure 6.12. The infall velocity in the radial direction on the x-y plane is very close to that calculated along the vertical z direction for FR13, suggesting that the accretion for this fragment is spherically symmetric, rather than mainly through a polar accretion flow as in many other fragments in this chapter. FR14 does show evidence of such an inflow in its infall velocity along the vertical z direction though it is not as strong as other fragments discussed. The resolution along the vertical z direction is poor exterior to a few AU but, in the case of FR13, the location of the inner core in the radial direction along in the x-y plane is very close to that in the vertical z direction. This indicates that the fragment is spherical in this case. FR14 may be slightly flattened and the first core is located at a larger radii than in FR13.

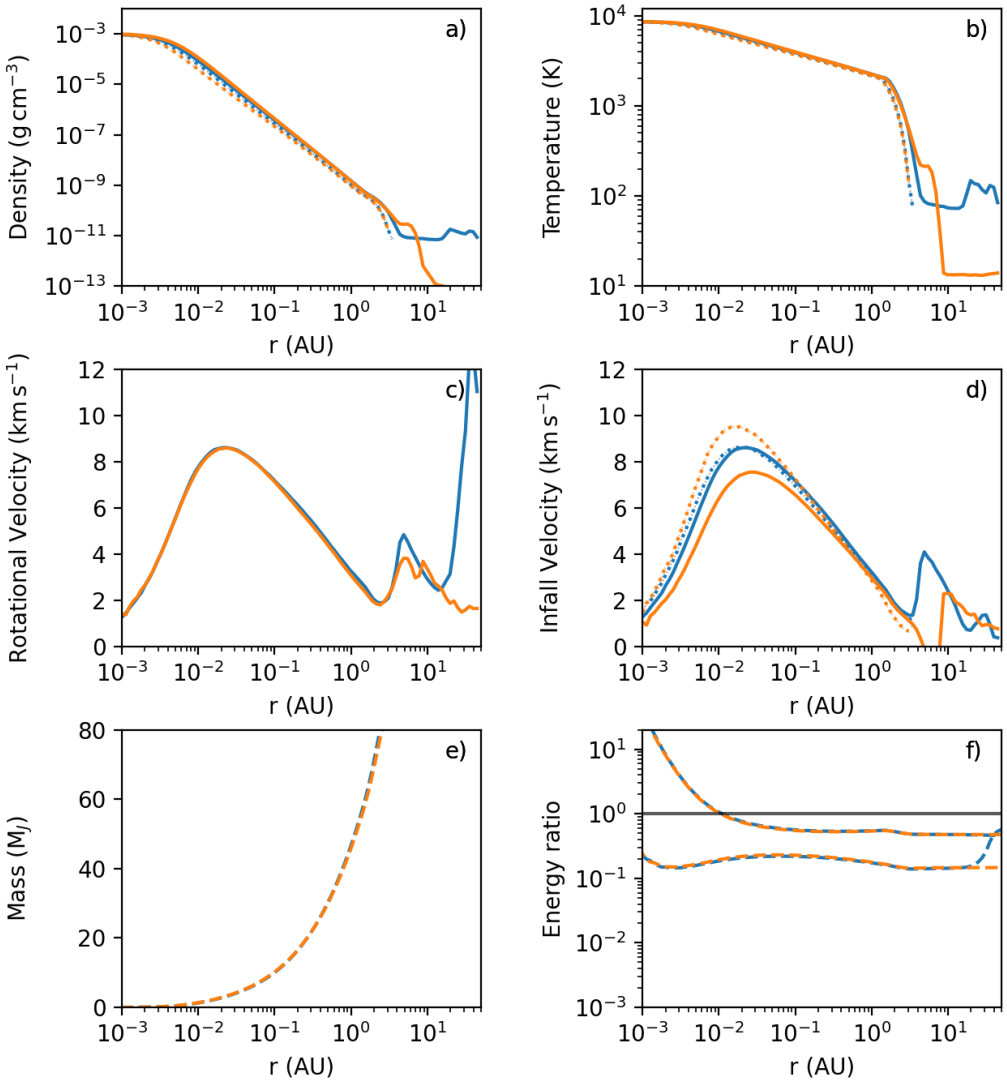

Figure 6.12: Same as Figure 6.1 but for FR13 (blue lines) and FR14 (orange lines).

Figure 6.13 that FR13 (left) and FR14 (right) are close to symmetric. The atypical morphology of FR14 may be a result of a merger event during its evolution. In addition to the morphology of the fragment in the x-y plane, I also plot particles within 5 AU of the centre of each fragment in the x-z plane in Figure 6.14 which shows

that the fragments in these two runs are very close to being spherically symmetric.

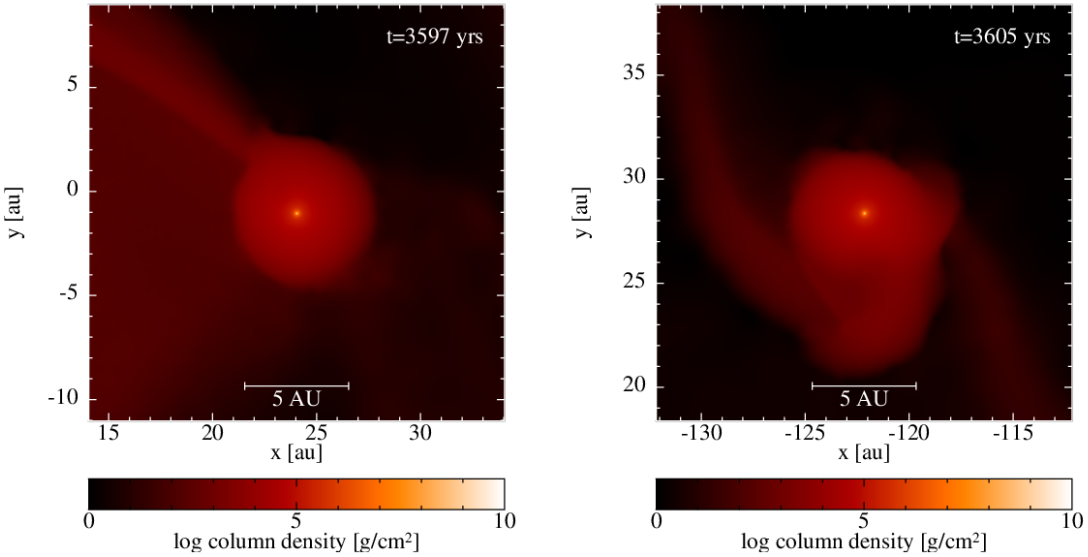

Figure 6.13: Morphologies of FR13 and FR14 when the density at the centre of the fragments reaches $\rho_c = 10^{-3} \mathrm{g\,cm^{-3}}$.

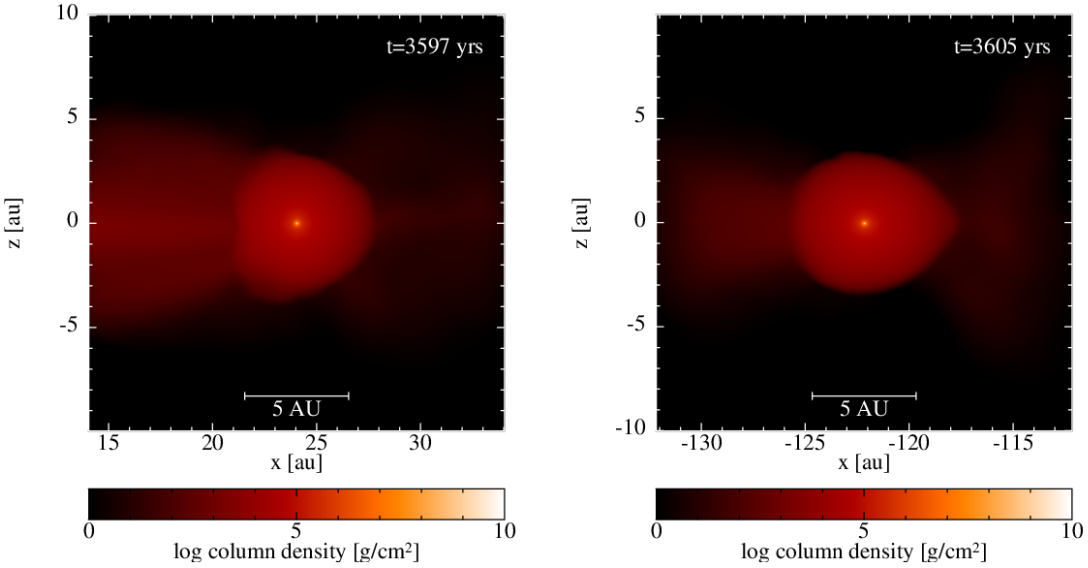

Figure 6.14: Fragments FR13 and FR14 viewed in x-z plane. For these equations of state, the fragments are very close to spherical

6.2.7 Runs 15 and 16

Runs 15 and 16 share the same adiabatic indices as runs 7 and 8 but diverge from isothermality at a higher density. As is the case in runs 7 and 8, the temperature at the centre of the fragments that form in runs 15 and 16 do not reach those required to dissociate molecular hydrogen and trigger the second collapse and so the second core does not form. Figure 6.15 shows the structure of four representative fragments that form in runs 15 and 16. As in runs 7 and 8, two morphological groups emerge; group A fragments that have a first core that extends out to a few tenths of AU from the centre of the fragment, and group B fragments in which the first core has a very small radius. In the figure, group A fragments FR15-A and FR16-A are indicated by the blue and orange lines while group B fragments, FR15-B and FR16-B are shown by the green and red lines respectively.

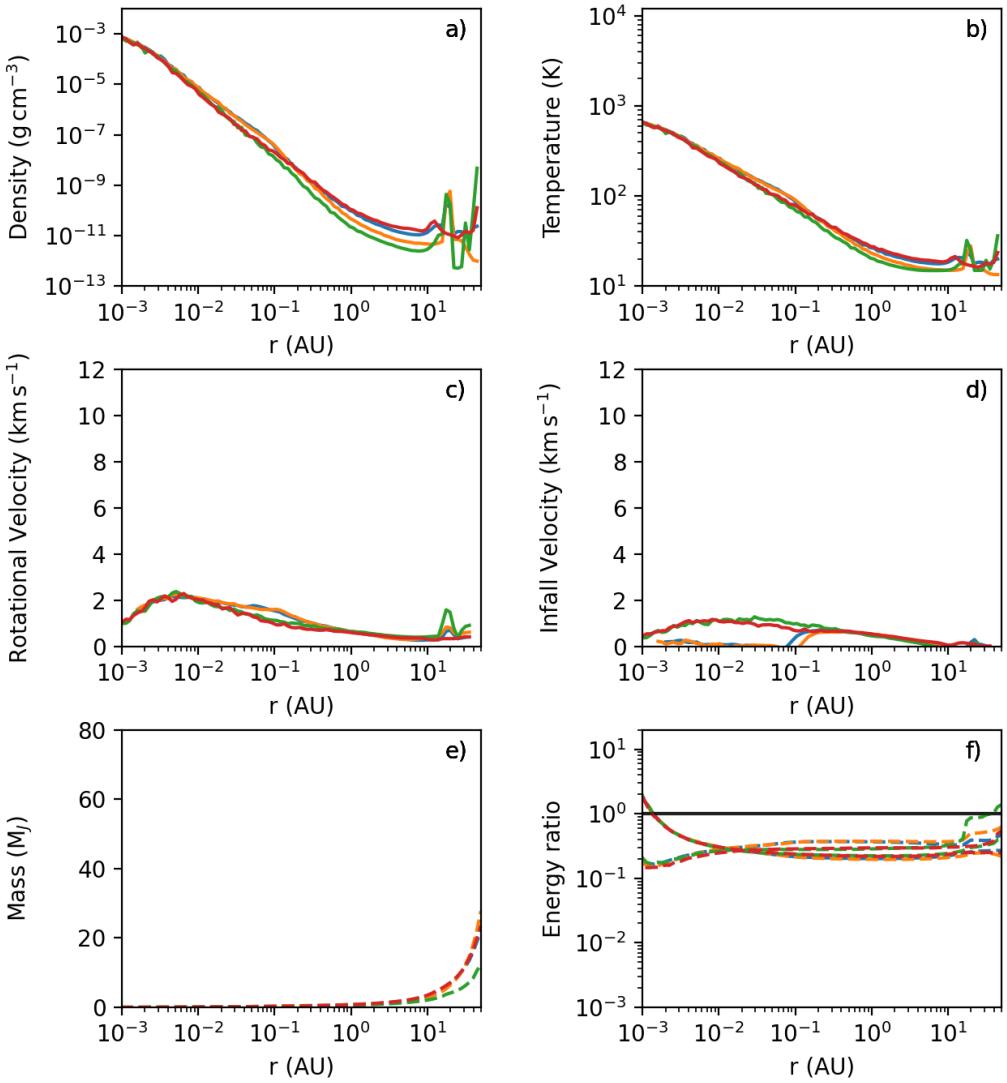

Figure 6.15: Same as Figure 6.1 but for FR15-A (blue lines), FR15-B (orange lines), FR16-A (green lines) and FR16-B (red lines)

The lower thermal pressure inside of the fragment leads to a more compact morphology than those that form in run 7 and 8. This is clear when comparing the morphologies of FR15 and FR16 fragments in Figure 6.16 with those in Figure 6.7.

As before, the group A fragments (left hand panels of Figure 6.16) show evidence of spirals arms on very small scales, within ~ 0.1 AU from the centre of the fragment; these spirals are indicated by an increased rotational velocity around 0.1 AU from the centre of the fragments in panel c) of Figure 6.15. The fragments that belong to group B (right hand panels in Figure 6.16) do not show evidence of spirals and are instead very compact.

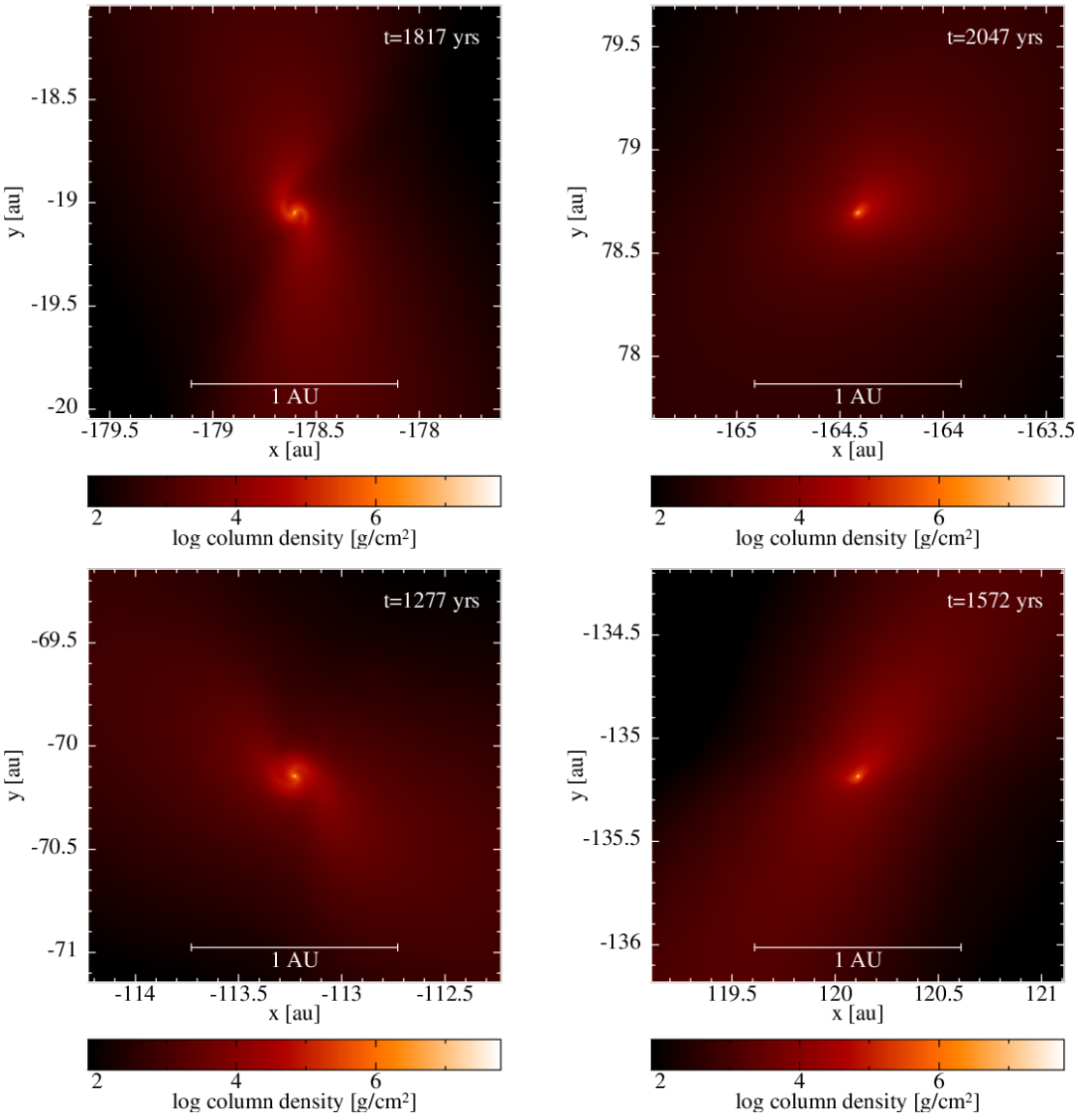

Figure 6.16: The morphologies of representative fragments in runs 15 (top row) and 16 (bottom row).

6.3 The Effect of the EOS on the Properties of Protoplanets

In this section I will discuss the effect of disc thermodynamics on the properties of the fragments, i.e. the protoplanets. I will present the properties of the first and second hydrostatic cores and how the EOS effects their mass and size, followed by a discussion of how the shape of the fragments varies with the choice of EOS.

6.3.1 Properties of the First and Second Cores

Figure 6.17 shows the properties of the first and second cores of fragments that form in simulations with different equations of state as listed in Table 6.1. In panel a) of Figure 6.17, the mass of the second core is shown as a function of its radius. Runs 7, 8, 15 and 16, i.e. those with the shallowest EOS ($\gamma_1 = \gamma_2 = 1.2$) do not appear in this plot due to there being no second core in the fragments that formed in those discs. In these equations of state, the temperature at the centre of the fragments does not reach that required for hydrogen to dissociate and so the second core does not form. Most of the second cores are of between 1 and 10 M_J with the lowest mass fragments having formed in discs with fairly shallow adiabatic regions. These low mass fragments are shown in brown and pink in the Figure, corresponding to runs 9 and 10, respectively. These equations of state have $\gamma_1 = \gamma_2 = 1.4$ (see Table 6.1) and, of those that reach the temperatures required of hydrogen dissociation, have the shallowest first adiabatic zones. The runs with steeper equations of state (runs 3, 4, 11, 12, 13 and 14) form fragments with the highest mass second cores. Though, particularly in the cases of runs 3 and 4, the temperature of the gas increases very rapidly causing the thermal pressure to prevent the formation of many fragments. Indeed, runs 5 and 6 do not produce any fragments, owing to this effect. Despite the differences in EOS, the second core masses are mostly below the mass threshold

for a planet ($13\,M_J$) and have radii of 2 - $8R_\odot$, which is consistent with the findings of Mercer & Stamatellos (2020).

Panels b) and c) show the mass of the inner and outer boundaries of the first core as a function of their respective radii. The low mass, small radius regime is dominated by fragments that form in runs 7, 8, 15 and 16. These runs produce many fragments with very small first cores (see sections §6.2.3 and 6.2.7 and the discussion of group B fragments therein). A small number of the fragments that form in these runs have first core radii $> 1\,AU$. As in the case of the second cores, the highest mass fragments are those that form in discs with steep first adiabatic zones, though these fragments do not have markedly higher radii than those that are of lower mass. Runs 9 and 10 produce fragments that vary widely in the location of the inner boundary of the first core, which ranges from $\sim 1\,AU$ to $\sim 11\,AU$. Though runs 1 and 2, which share the same values of γ_1/γ_2 as runs 9 and 10, produce fragments with a narrower range of inner first core radii but have a wider spread in masses. The relationship between the size of the outer boundary of the first core and its mass is clear in panel c) of Figure 6.17 where a fragment with a larger first core radii is more massive. Panel c) also reveals a clear dependence of both the mass and radius of the outer first core on the slope of the values of $\gamma_1 \text{and} \gamma_2$. The fragments with the lowest mass and radius form in discs with the lowest values of γ and, with increasing EOS steepness (i.e. a stiffer EOS), the mass and radius of the outer first core increases.

The first core shock width (i.e. $R_{\text{fc,o}}$ - $R_{\text{fc,i}}$) as a function of the specific angular momentum of the outer boundary of the first core is shown in panel d) of Figure 6.17. Discs with thermodynamics determined by steeper equations of state produce fragments with higher specific angular momentum and, broadly speaking, greater shock widths, though there are a number of exceptions. Runs 1, 2 and 11 produce a few fragments with large shock widths, larger than the few fragments that are

produced in discs with the steepest equations of state.

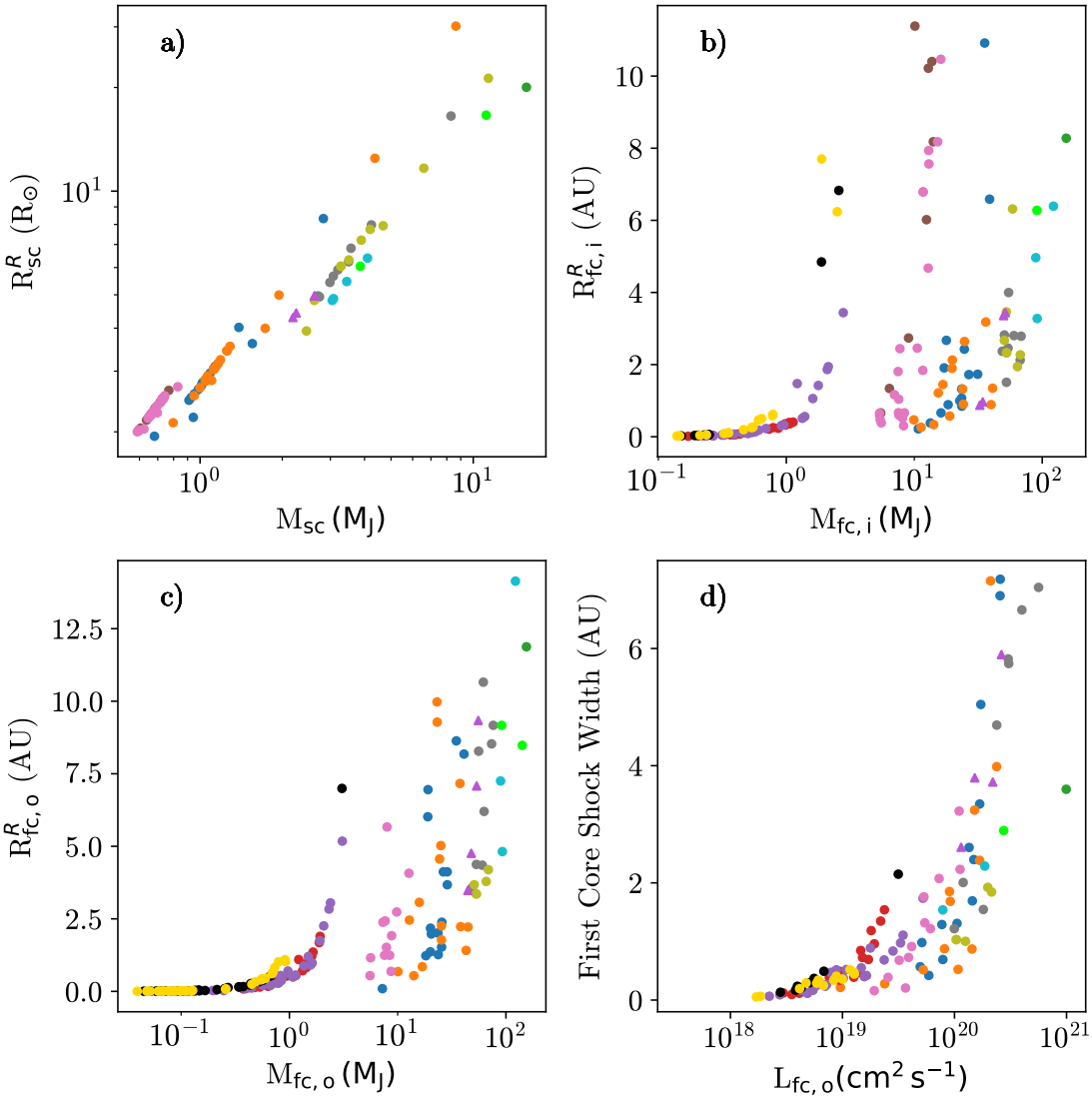

Figure 6.17: The properties of the fragments that form in simulations with different equations of state as listed in Table 6.1. In the interest of clarity, the values evaluated in the vertical z direction have been omitted and a discussion of the shape of the fragments is presented later in section 6.3.3. The triangle markers show the values for the benchmark run fragments.

Figure 6.18 shows the properties of the first core as a function of the distance of the fragment from the central star. The mass contained within the inner boundary

of the first core is plotted in the top panel. This graph shows the relationship between disc temperature and the spatial range over which fragments form. By way of example, in run 2 with $T_{1\,AU} = 150\,K$ (orange points) fragments on shorter orbits than its counterpart in run 1 (blue points) where $T_{1\,AU} = 200\,K$. The same is true for runs 9 and 10 (brown and pink points respectively) in which the cooler disc, run 10, produces fragments as close as $\sim 25\,AU$ from the central star compared to the closest fragment in run 9 ($T_{1\,AU} = 200\,K$) located at $\sim 125\,AU$. As discussed in sections 6.2.3 and 6.2.7, the steepest equations of state produce fragments with very small first core radii (and therefore very low first core masses). The groupings of purple and yellow points clustered around $\sim 50 - 75\,AU$ and $\sim 100 - 150\,AU$ respectively belong to this class of fragments. Both of these, which represent fragments from runs 8 and 16, respectively, share the same adiabatic indices but differ in the first critical density, where the EOS switches from isothermal to adiabatic. Run 16, which has a critical density of $\rho_1 = 6 \times 10^{-13} g\,cm^{-3}$, produces fragments with small first cores at larger radii than run 8 which diverges from isothermality at a lower density. Owing to the small data sets of fragments that form when using steep equations of state, it is difficult to determine a definitive relationship between the density at which the equation of state becomes adiabatic and the radius at which fragments form. However, the locations of fragments that form in runs 1 and 9 and in runs 8 and 16 suggest that such a relationship may exist.

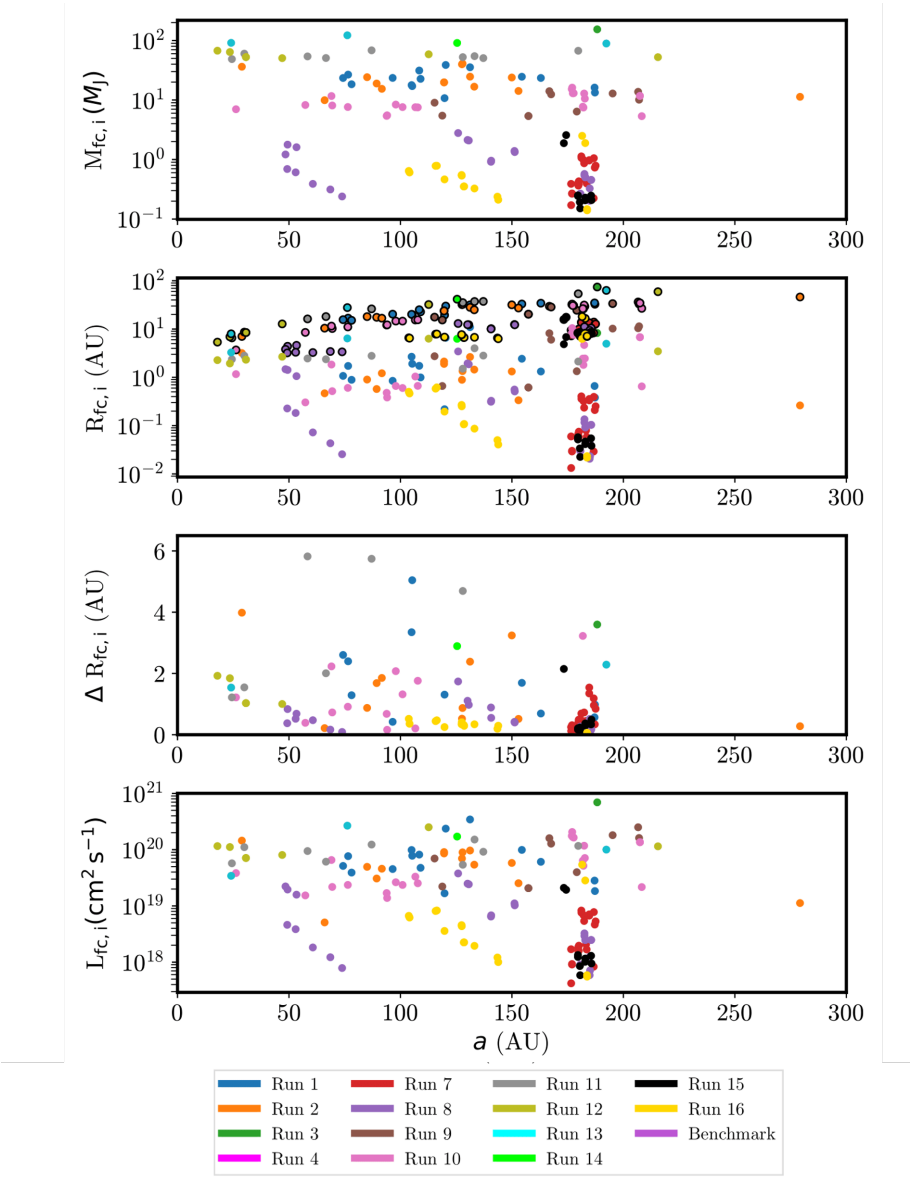

Figure 6.18: The mass, radius, accretion shock width and specific angular momentum (top to bottom) of the first cores of fragments that formed in discs that use the different equations of state listed in Table 4.1 as a function of the distance from the central star. Runs 5 and 6 do not produce fragments with sufficiently high central densities and so they do not appear in the the plot. All points indicate the values calculated in the radial direction on the x-y plane. The triangles correspond to the benchmark run fragments. The points with the black outlines on the second panel indicate the Hill Radius of the fragments.

The second panel of Figure 6.18 illustrates the relationship between the radius of the inner boundary of the first core and the distance of the fragment from the central star. We see that fragments on wider orbits tend to have larger first core radii. The difference between first core radii of fragments on small orbits and those on wide orbits is particularly pronounced for runs 1, 2, 9 and 10 for which $\gamma_1 = \gamma_2 = 1.4$. Steeper equation of state, e.g. runs 11 and 12, show a far smaller difference in $R_{fc,i}$ between fragments on short and wide orbits. The width of the accretion shock (third panel in Figure 6.18) does not show any significant dependence on the position of the fragment in the disc. However, runs with certain equations of state produce fragments with similar shock widths; those that form in run 12 all have shock widths of $\sim 1 - 2\,\mathrm{AU}$ and those in the runs with the shallowest equations of state also tend to have very low shock widths around the first core. Most of the fragments shock widths that are less than $\sim 2.5\,\mathrm{AU}$. The specific angular momentum of the fragments, shown in the bottom panel of the figure, indicates a similar trend as the mass of the first core (shown in the top panel). Indeed, when specific angular momentum is plotted as a function of the mass of the fragment, the relationship is evident (see Figure 6.19). In this plot, the groupings of EOS 'pairs' is very clear and the runs with the steepest equations of state (runs 11, 12, 13 and 14) occupy the region of highest mass and highest specific angular momentum.

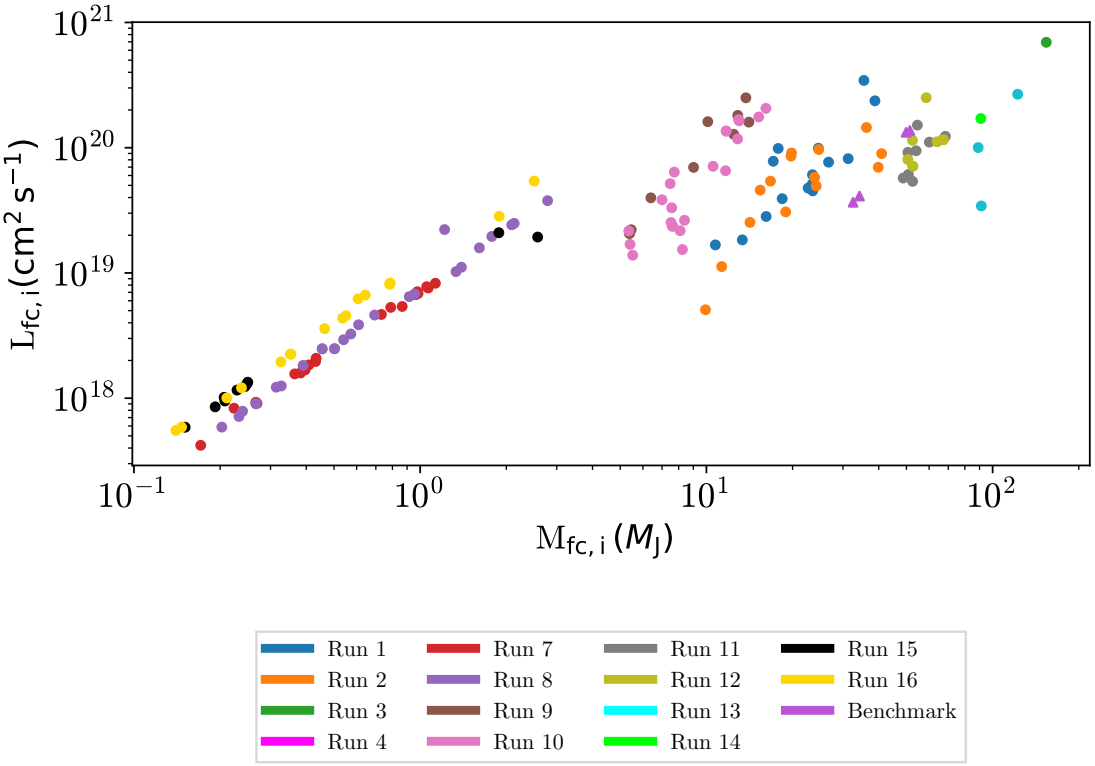

Figure 6.19: The specific angular momentum of the inner boundary within the first core as a function of its mass. The groupings of EOS 'pairs' is very clear.

The properties of the second cores are shown in Figure 6.20 as a function of the distance of the fragment to the host star. With the exception of the highest mass fragment that formed in run 3, all second cores (i.e. the protoplanets) are below the planet mass threshold. Most of the protoplanets that form have masses below 5 M_J which is consistent with the findings of Mercer & Stamatellos (2020). As was the case for the first cores, both the second core masses and their radii (top and middle panels of the Figure, respectively) increase with higher values of γ, although the effect is less prominent than it is in the case of the first cores. The mass, radius and specific angular momentum of the second core do not seem to depend on the position of the fragment in the disc. Fragments that form in discs governed by the same equation of state have similar values for these quantities. However, as in the

case of the first cores, the EOS has a more significant impact. The fragments that form in discs with shallow equations of state have lower specific angular momentum than those in discs with stiffer equations of state.

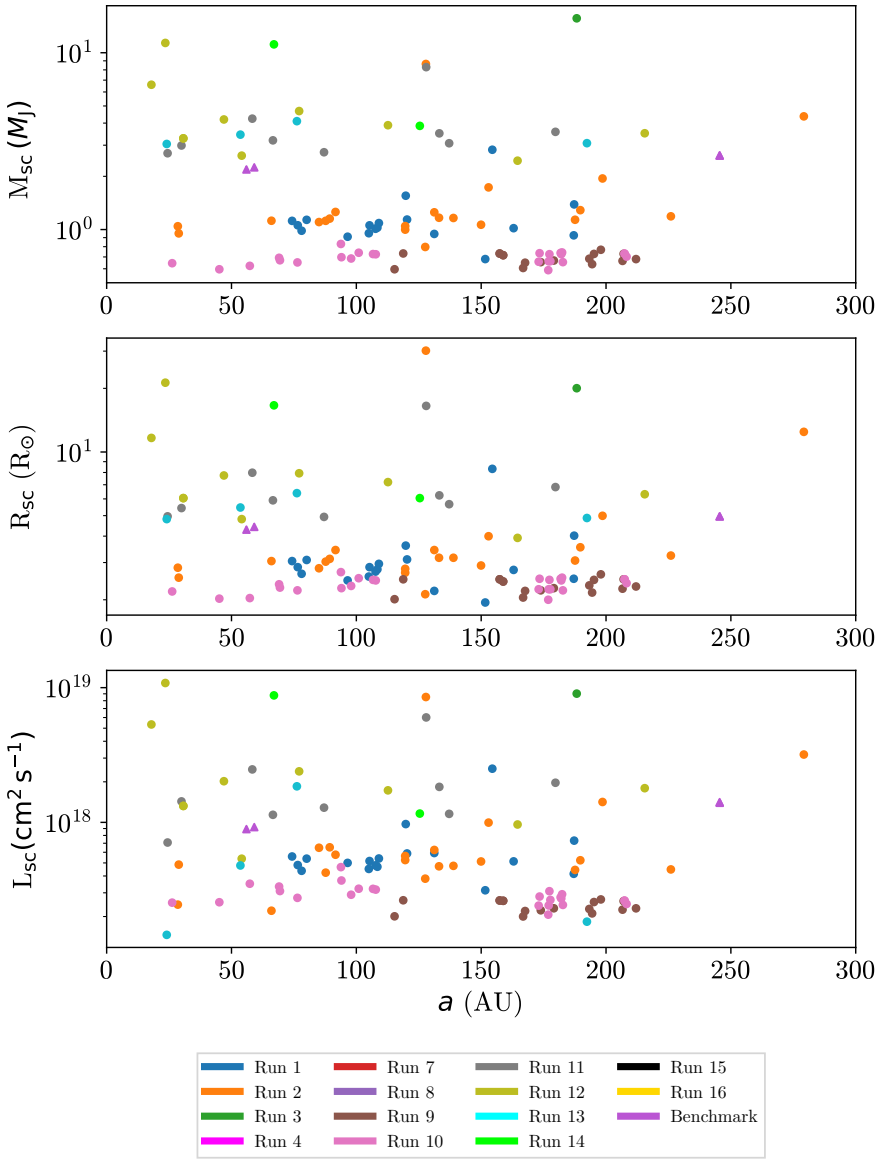

Figure 6.20: The mass, radius and specific angular momentum of the second cores of the fragments that form in discs that use the different equations of state listed in Table 4.1 as a function of the distance from the central star. The symbols are the same as those in Figure 6.18.

6.3.2 Fragment Evolution

As with the benchmark fragments, I also investigate the collapse time of the fragments which I define as the time $\Delta t_{\rm c}$, it takes for the fragments to evolve from $\rho_{\rm c} = 10^{-9}{\rm g\,cm^{-3}}$ to $\rho_{\rm c} = 10^{-3}{\rm g\,cm^{-3}}$. The top panel of Figure 6.21 shows the evolution time as a function of the orbital radius of the fragment. There exists a collection of fragments that collapse on very short timescales ($< 10\,{\rm yrs}$). This group is mostly made up of fragments that form in discs with the shallowest equations of state (runs 7, 8, 15 and 16). In these discs, the temperature at a given density is much lower than for other equations of state (see Figure 4.5) and so the thermal pressure within the fragment is insufficient to slow down the collapse. Indeed, runs 15 and 16 (black and yellow points, respectively) produce fragments that are allowed to evolve to higher central densities isothermally i.e. the thermal pressure in these fragments is lower for longer. The fragments that take the longest to evolve are those that do so in run 9 (brown points). This equation of state has the same adiabatic indices as runs 1,2 and 10 and though the fragments in those runs do form on longer time scales, those in run 9 do so consistently - all run 9 fragments have $\Delta t_{\rm c} > 400\,{\rm yr}$. One would expect the cooler discs in each pair to have fragments that collapse on a shorter timescale, employing the same reasoning behind fragments in discs with shallow equations of state. This is true for runs 9 and 10; the cooler disc (run 10; pink points) produces fragments that collapse on a shorter timescale than their counterparts in run 9, the hotter disc. However, the same cannot be said of runs 1 and 2 (blue and orange points, respectively) where the hotter disc (run 1) produces fragments that evolve on shorter timescales.

The bottom panel of Figure 6.21 shows the relationship between the collapse time and the specific angular momentum at the outer boundary of the first core. The shallowest equations of state have the shortest collapse times and specific angular momenta. In many of these fragments, spiral arms form in the immediate vicinity

and redistribute angular momentum outwards from the centre of the fragment. Most of the fragments that formed in runs 15 and 16 did so on very similar timescales. From Figure 6.21 (bottom panel), it can be seen that fragments with higher specific angular momentum tend to collapse slower.

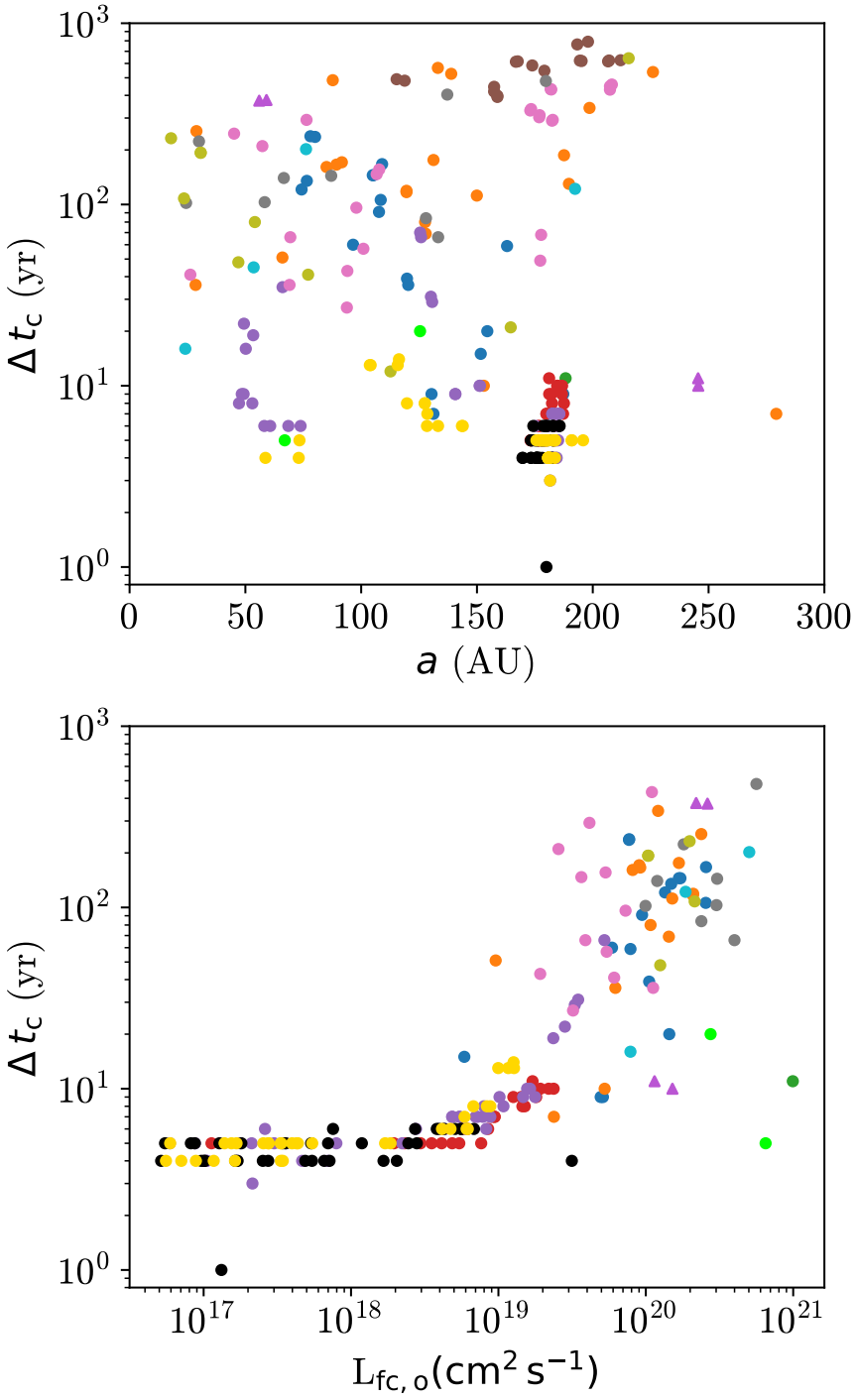

Figure 6.21: The time taken (Δt_c) for the fragments to evolve from a central density of 10^{-9}g cm^{-3} to 10^{-3}g cm^{-3} as a function of their distance from the star (top) and their specific angular momentum (bottom). The triangles show the values for the benchmark run fragments.

6.3.3 The Shape of Fragments

In this section I will discuss the shape of the fragments by comparing the three aspect ratios defined in Chapter 5 and summarised as follows. $e_{\rm fc,i}$ and $e_{\rm sc}$ correspond to the aspect ratio of the first core, evaluated at its inner boundary and the aspect ratio of the second core, respectively. e corresponds to the aspect ratio defined by the radius at which the fragment's density is $10^{-9}{\rm g\,cm^{-3}}$ in the vertical z direction over that in the radial direction on the x-y plane.

The top and middle panels of Figure 6.22 show the aspect ratio of the inner boundary of the first core and the second core, respectively. In many cases, the resolution is insufficient in the vertical z direction to estimate the radius of the first core (top panel). Though the second core is well resolved for most fragments in both the radial direction on the x-y plane and along the vertical z direction, the aspect ratio of the second core (middle panel) does not illustrate a complete picture of the shape of the fragments because fragments that do not form a second core are missing. A full representation of the shape of the fragments is shown in the bottom panel of Figure 6.22 where the aspect ratio e is plotted for all fragments. Most of the fragments have $e < 1$, indicating that the majority of the fragments that form across the whole parameter space are 'flattened' and are oblate spheroids rather than the previously assumed spherical objects. A number of fragments have very high aspect ratios these may be a result of merger events around the time of formation. Those with very low aspect ratios (< 0.1) are likely the result of poor resolution and are unlikely to be physical. Due to the method by which the aspect ratios are calculated (i.e. using the average infall velocity profiles and density profiles to establish values for core radii) there is an uncertainty associated with their values. However, in selecting particles only within a small region around the centre of the fragment, this uncertainty has been minimised. A typical uncertainty for the aspect ratios can be estimated by using the bin width in the region around the first and second cores as

the error in the distance from the centre of the fragment. Doing so yields typical values of $e_{\mathrm{fc,i}} = 0.19 \pm 0.03$, $e_{\mathrm{sc}} = 0.93 \pm 0.15$ and $e = 0.56 \pm 0.09$. These values have been omitted from Figure 6.22 for clarity.

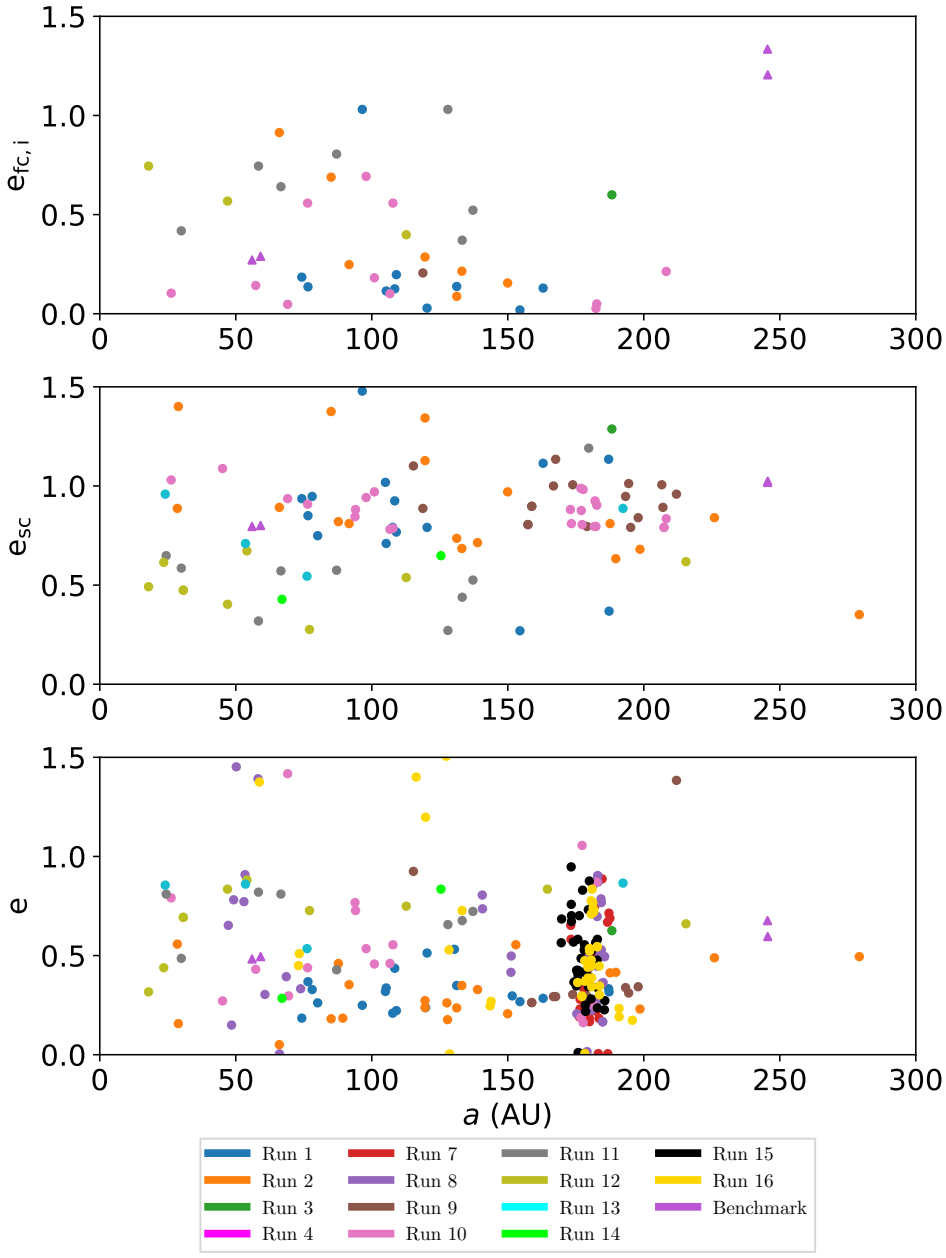

Figure 6.22: The aspect ratios $e_{\mathrm{fc,i}}$ and e_{sc} and e (top to bottom) of all fragments that formed in this study. The triangle markers show the values for the benchmark run fragments.

There is no significant dependence of the aspect ratio of a fragment on its orbital radii, regardless of the equation of state. Within individual equations of state, fragments tend to have similar axis ratios. Discrepancies may be a result of violent evolution. The aspect ratios of fragments from all simulations with different equations of state are less than unity, reiterating that they are indeed flattened. The degree to which they are flattened may be influenced by the specific EOS. Runs 1 and 2 ($\gamma = 1.4, \rho_c = 1 \times 10^{-13}\mathrm{g\,cm^{-3}}$; blue and orange points) have aspect ratios consistently < 0.5 whereas run 10 ($\gamma = 1.4, \rho_c = 6 \times 10^{-13}\mathrm{g\,cm^{-3}}$; pink points) produces fragments that are slightly less flattened which aspect ratios between ~ 0.5 and ~ 0.75. The under-representation of very steep equations of state that switch to adiabatic at $1 \times 10^{-13}\mathrm{g\,cm^{-3}}$ means it is difficult to draw a definitive conclusion as to whether the duration of the isothermal phase has an impact on the shape of fragments. However, fragments in runs 9 - 16 (i.e. those with $\rho_1 = 6 \times 10^{-13}\mathrm{g\,cm^{-3}}$) do have slightly higher aspect ratios in some cases, but not in all.

6.4 Summary

In this chapter I have discussed the properties of fragments that form in gravitationally unstable discs with thermodynamics determined by different equations of state in an effort to determine the effect of the EOS on fragment formation and evolution. The results of this chapter build on those presented in Chapter 5 wherein the properties of benchmark fragments was discussed. The general properties, common across a number of equations of state, are presented in Section 6.1 wherein I discuss the simulations with extreme equations of state with the steepest and shallowest adiabatic regions and the fragments that form therein.

The mass of the fragments depends on the steepness of the equation of state, i.e. the value of γ. The temperature at the centre of fragments that form in the steepest equations of state increases more per unit density than those in shallow equations of

state. The increased thermal pressure means that the fragment must accrete more gas for the collapse to continue (i.e. reach $\rho_c = 10^{-9}\mathrm{g\,cm^{-3}}$ where fragment tracking begins) and are consequently higher mass by the end of the simulation. Indeed, these fragments have amongst the highest mass first and second core masses, as discussed in section 6.3.1. This effect is shown in Figure 6.23 in which I plot the mass and radius of the first core (top two panels) and that of the second core (bottom two panels) as a function of the distance of the fragment from the star. The colour of the marker indicate the value of γ used and their shape show the density at which the equation of state becomes adiabatic. Filled and unfilled markers show fragments that form in discs with reference temperatures of $\mathrm{T_{1\,AU}} = 200\,\mathrm{K}$ and $\mathrm{T_{1\,AU}} = 150\,\mathrm{K}$, respectively.

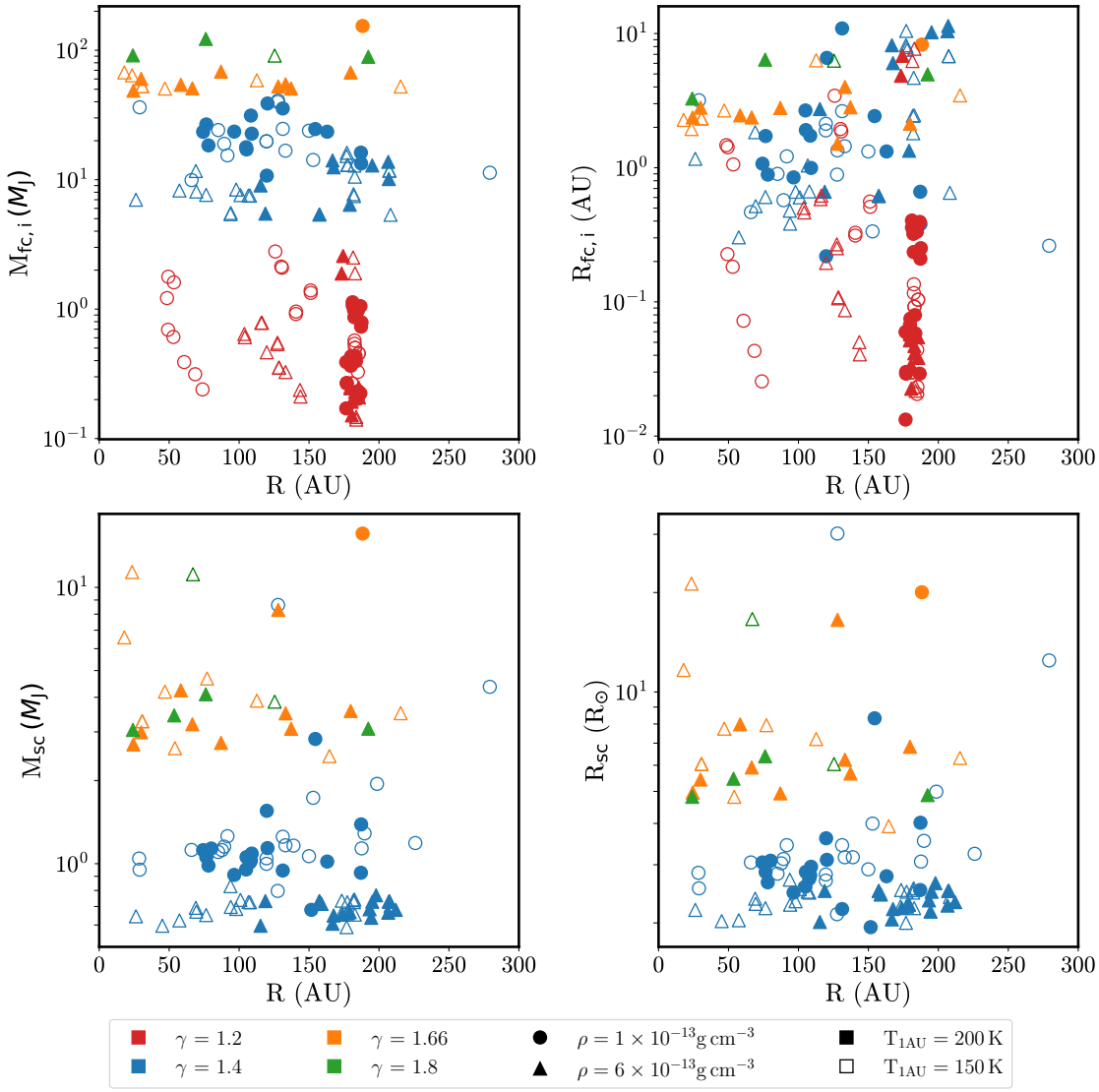

Figure 6.23: The effect of the value of γ on the mass and radius of the fragments. The top panels show this for the mass and radius of the first core (top left and top right panels, respectively) and the bottom panels show the same for the second core. The colour of the markers indicate the value of γ, the shape show the density at which the equation of state switches from isothermal to adiabatic and the filled/unfilled markers indicate the reference temperature of the disc.

Broadly speaking, the width of the first accretion shock increases for steeper

equations of state, as does the specific angular momentum of the fragments. Furthermore, the relative steepness of the EOS also effects the degree to which the second cores are 'flattened', with steeper equations of state forming fragments with lower aspect ratios (see section 6.3.3).

Aside from testing the effect of the adiabatic index of the EOS, I have also investigated the impact that the critical density has on fragment evolution. The critical density, defined by that at which evolution diverges from isothermality and into adiabaticity, is set to $1 \times 10^{-13} \mathrm{g\,cm^{-3}}$ for runs 1-8 and $6 \times 10^{-13} \mathrm{g\,cm^{-3}}$ for runs 9-16. This means that fragments that form in runs 9-16 have a longer isothermal evolutionary phase. As discussed in section 6.1, if the isothermal evolutionary phase is longer, the disc is cooler for longer and so the disc has greater opportunity to fragment. Indeed I find that these equations of state produce more fragments.

I investigate the effect of the disc temperature on the formation and evolution of fragments that form in gravitationally unstable discs by varying the reference temperature at 1 AU. In this way, each EOS is part of a pair (e.g. runs 1 and 2 have the same equation of state and vary only in the reference temperature at 1 AU). I find that cooler discs produce more fragments across a greater spatial range than their warmer counterparts. This is to be expected since the conditions for fragmentation to occur are satisfied over a greater range in a cooler disc than in a hotter one. The disc temperature does not seem to significantly affect the properties of individual fragments however.

As for the benchmark fragments, most of the fragments that form in all simulations with different equations of state tested in this work are flattened to some degree. This means that fragments cannot be assumed to be spherically symmetric as in previous works and their 3D structure must be accounted for. Furthermore, when studying the infall velocities along the vertical z direction, I have found that most fragments that form have a significant polar accretion inflow through which

they accrete mass from the surrounding disc. The relative difference between the infall velocity in the vertical z direction and that in the radial direction on the x-y plane seems to increase with the steepness of the equation of state.

Chapter 7

Discussion

This thesis focused on the properties of protoplanets that form as a result of the fragmentation of gravitationally unstable discs. I performed a numerical study, employing smoothed particle hydrodynamics simulations and a novel fragment tracking algorithm, which allows for the capture of the precise evolution of fragments, to assess the effect of the equation of state on the proprieties of protoplanets. I used a barotropic equation of state, chosen for its approximation of a rigorous treatment of radiative transfer, and began the investigation by running a benchmark simulation with equation of state parameters similar to previous work. I investigated the structure of the fragments by first adopting the common assumption that they are spherically symmetric and then discussed their 3 dimensional structure. Following this, I explored a parameter space wherein the specific equation of state was varied to assess the implications of different thermodynamics on the properties of protoplanets. In this investigation, I treated the fragments as axisymmetric and compared their structure in the radial direction on the x-y plane with that in the vertical z direction. In this chapter I will summarise the results of these investigations and present possible avenues for further consideration.

CHAPTER 7

7.1 3 Dimensional Structure of Fragments

Previous investigations of the fragments that form as a result of fragmentation in gravitationally unstable discs have adopted the assumption of spherical symmetry (Mercer & Stamatellos, 2020; Stamatellos et al., 2007). In the work presented here I investigated the full 3 dimensional structure of the fragments by calculating their density, temperature, rotational and infall velocity profiles along different directions. I found that the structure of the fragments is similar for the ±x and ±y directions but different for many fragments in ±z direction. This shows that the fragments are oblate spheroids rather than spherical. I continued the investigation of further fragments, beyond those that form in the benchmark run. I defined three aspect ratios, that for the first and second core boundaries as well as a density dependant aspect ratio defined by the position in the vertical z direction at which the density of a fragment reaches $10^{-9}\mathrm{g\,cm^{-3}}$ divided by that in the radial direction on the x-y plane. These quantities served as points of comparison when considering the effect of the equation of state on the formation and evolution of fragments.

7.2 Effect of the EOS on the Properties and Evolution of Fragments

The main pursuit of this work was to assess the implications of thermodynamics on the properties of protoplanets. I explored this by running a collection of smoothed particle hydrodynamics (SPH) simulations using the open source code PHANTOM with different implementations of the barotropic equation of state. Beginning with a benchmark run, chosen to match the EOS of previous work, I established a baseline of fragments that were used as points of comparison for fragments that form under different conditions. Of the equations of state tested, those with steeper adiabatic zones formed the most massive fragments; first core masses of these fragments were

$> 80\,\mathrm{M_J}$. Second core masses, i.e. those of the protoplanets, were mostly below the planetary threshold of $13\,\mathrm{M_J}$ and have radii of 2-8 $\mathrm{R_\odot}$ which is consistent with the findings of Mercer & Stamatellos (2020). Broadly speaking, discs with thermodynamics governed by steeper equations of state formed fragments with wider first core accretion shocks and larger specific angular momenta. Though, since runs with the steepest equations of state also form the fewest fragments, this conclusion warrants further work. I also find that discs with longer isothermal evolutionary phases, i.e. those that diverge from isothermality at a higher density (runs 9 - 16) produce more fragments. The shape of the fragments, i.e. their aspect ratios, did not depend on their position. The second core, approximately spherical for fragments that formed in discs governed by shallow equations of state, tended to be flattened to a greater degree in equations of state with steeper adiabatic zones. Additionally, the degree of flattening for the second core was greater for fragments with larger specific angular momentum. The shallowest equations of state, did not reach high enough central temperatures to trigger the dissociation of molecular hydrogen and the second core did not form. Both of these EOS pairs formed fragments that tended to fall into one of two morphological groups: those with first core radii of $\sim 0.1\,\mathrm{AU}$ and those with a much smaller first core at radii of $\sim 0.005 - 0.01\,\mathrm{AU}$.

7.3 Polar Accretion Flows

The investigation into the 3D structure of the fragments revealed a distinct difference in the infall velocity calculated along the radial direction on the x-y plane and that in the vertical z direction, particularly in the region around the outer boundary of the second core. This implies the existence of polar accretion flows from which the fragments also accrete matter from the disc. The infall velocity along the vertical z direction is consistently larger than that calculated along the radial direction in the x-y plane. The flow is disrupted in fragments that formed by the merging of two

or more 'proto-fragments' or where they were the subject of an otherwise violent evolution. Fragments with the largest infall velocities in the vertical z direction are also the most massive, suggesting that large amounts of mass are accreted via this route.

7.4 Considerations for Further Work

This work can be expanded in the following directions:

- I have found that fragments that form as a result of gravitational instability are flattened in the vertical z direction. I suggest a dependence of the aspect ratio of fragment on the specific EOS. However, since the steepest equations of state form very few fragments, this area of the parameter space would benefit from further investigation to improve statistics.

- The mass of the star throughout this study is $M_* = 0.8\,M_\odot$ but Mercer & Stamatellos (2020) show that discs around M dwarfs ($M_* < 0.5\,M_\odot$) are susceptible to gravitational fragmentation with disc to star mass ratios of $0.3 < q < 0.6$. An investigation into the effect of stellar mass on the properties of the protoplanets that form, particularly those that relate to the shape of the fragments and the existence of polar aligned inflows, warrants further work.

- I have used a hybrid equation of state that includes the effect of a barotropic EOS with a locally isothermal one to provide a minimum temperature floor. A comparison between this treatment of thermodynamics, where the individual parameters of the EOS can be precisely controlled, with a more rigorous treatment of radiative transfer would provide a deeper understanding of the collapse of gravitationally unstable fragments.

- A limitation introduced by modelling the thermodynamics with a barotropic equation of state is the lack of cooling. Rather, in a barotropic equation of state, cooling is instantaneous. This means that when two fragments collide, they are far more likely to merge rather than be dispersed due to an increase in thermal pressure associated with the collision. Indeed, throughout this work, I have recorded many instances of fragment mergers. A future piece of work comparing that which has been outlined here and the results from a treatment of radiative transfer that incorporates cooling would serve as a poignant reflection of the applicability of the barotropic equation of state in this context.

7.5 Conclusions

In this thesis I have investigated the fragmentation of gravitationally unstable discs and the effect of the equation of state on the properties of the fragments (i.e. the protoplanets) that form. The key findings of this work are summarised as follows:

- The fragments that form as a result of gravitation instability are rarely spherical symmetrical. By analysing their structure in the radial direction in the x-y plane and that in the vertical z direction, I have determined that most of the fragments that form are oblate spheroids rather than spherical as has previously been assumed.

- The fragments have polar aligned inflows from which they accrete material from the disc. These are evidenced by a high infall velocity in the vertical z direction which is sometimes as much as double that calculated in the radial direction on the x-y plane, i.e. the 'equatorial' flow. The relative difference in the infall velocity along both directions may depend on the specific equation of state. Fragments that form with steep equations of state tend to have very

high infall velocities in the vertical z direction.

- The mass of the fragments depends on the equation of state, with those that form in discs with the highest values of the adiabatic index γ producing the most massive fragments. Discs with thermodynamics governed by equations of state with very steep adiabatic regions (γ=1.8) produce fragments with first core masses $> 80\,\mathrm{M_J}$.

- Shallow equations of state with $\gamma = 1.2$ produce fragments with low central temperatures which do not reach that required for the dissociation of hydrogen and so do not have a second core. These fragments fall into one of two morphological groups; compact objects with very small first core radii and objects with slightly larger first core radii but with spiral features centred on the fragment.

Bibliography

Adachi I., Hayashi C., Nakazawa K., 1976, Progress of Theoretical Physics, 56, 1756

Andre P., Montmerle T., 1994, The Astrophysical Journal, 420, 837

Andre P., Montmerle T., Feigelson E. D., 1987, aj, 93, 1182

Andre P., Ward-Thompson D., Barsony M., 1993, The Astrophysical Journal, 406, 122

Andrews S. M., Williams J. P., 2007, The Astrophysical Journal, 659, 705

Andrews S. M., Wilner D. J., Hughes A. M., Qi C., Dullemond C. P., 2009, Astrophysical Journal, 700, 1502

Ansdell M. et al., 2018, The Astrophysical Journal, 859, 21

Armitage P. J., 2020, Astrophysics of Planet Formation, 2nd edn. Cambridge University Press

Artymowicz P., Lubow S. H., 1994, The Astrophysical Journal, 421, 651

Attwood R. E., Goodwin S. P., Stamatellos D., Whitworth A. P., 2009, Astronomy and Astrophysics, 495, 201

Balsara D. S., 1995, Journal of Computational Physics, 121, 357

Bate M. R., 2009, Monthly Notices of the Royal Astronomical Society, 392, 1363

Bate M. R., Bonnell I. A., Price N. M., 1995, Monthly Notices of the Royal Astronomical Society, 277, 362

Beckwith S. V. W., Sargent A. I., Chini R. S., Guesten R., 1990, The Astronomical Journal, 99, 924

Beuzit J. L. et al., 2019, Astronomy and Astrophysics, 631, 1

Bhandare A., Kuiper R., Henning T., Fendt C., Flock M., Marleau G. D., 2020, Astronomy and Astrophysics, 638, 1

Bhandare A., Kuiper R., Henning T., Fendt C., Marleau G. D., Kölligan A., 2018, Astronomy and Astrophysics, 618, 1

Biller B. A. et al., 2007, The Astrophysical Journal Supplement Series, 173, 143

Bitsch B., Boley A., Kley W., 2013, Astronomy and Astrophysics, 550

Borucki W. J. et al., 2010, Science, 327, 977

Boss A. P., 1997, Science, 276, 1836

—, 2008, The Astrophysical Journal, 677, 607

Bowler B. P., 2016, Publications of the Astronomical Society of the Pacific, 128, 1

Brinch C., Crapsi A., Jørgensen J. K., Hogerheijde M. R., Hill T., 2007, Astronomy and Astrophysics, 475, 915

Cadman J., Rice K., Hall C., Haworth T. J., Biller B., 2020, Monthly Notices of the Royal Astronomical Society, 492, 5041

Cartwright A., Stamatellos D., 2010, Astronomy and Astrophysics, 516, 1

Chauvin G. et al., 2010, Astronomy and Astrophysics, 509, 1

Chini R., Hoffmeister V. H., Nielbock M., Scheyda C. M., Steinacker J., Siebenmorgen R., Nürnberger D., 2006, The Astrophysical Journal, 645, L61

Cullen L., Dehnen W., 2010, Monthly Notices of the Royal Astronomical Society, 408, 669

Dehnen W., 2001, Monthly Notices of the Royal Astronomical Society, 324, 273

Desidera S. et al., 2021, Astronomy and Astrophysics, 651

Dipierro G., Laibe G., 2017, Monthly Notices of the Royal Astronomical Society, 469, 1932

Dodson-Robinson S. E., Veras D., Ford E. B., Beichman C. A., 2009, Astrophysical Journal, 707, 79

Dong R., Fung J., 2017, The Astrophysical Journal, 835, 38

Dong R., Najita J. R., Brittain S., 2018, The Astrophysical Journal, 862, 103

Dong R., Zhu Z., Rafikov R. R., Stone J. M., 2015, Astrophysical Journal Letters, 809, 1

Emsenhuber A., Mordasini C., Burn R., Alibert Y., Benz W., Asphaug E., 2021, Astronomy and Astrophysics, 656, A70

Evans N. J. et al., 2009, Astrophysical Journal, Supplement Series, 181, 321

Facchini S., Juhász A., Lodato G., 2018, Monthly Notices of the Royal Astronomical Society, 473, 4459

Forgan D., Rice K., 2013, Monthly Notices of the Royal Astronomical Society, 432, 3168

Forgan D. H., Hall C., Meru F., Rice W. K., 2018, Monthly Notices of the Royal Astronomical Society, 474, 5036

Forgan D. H., Ilee J. D., Meru F., 2018, The Astrophysical Journal, 860, L5

Fung J., Dong R., 2015, Astrophysical Journal Letters, 815

Gammie C. F., 2001, The Astrophysical Journal, 553, 174

Gardner J. P. et al., 2006, Space Science Reviews, 123, 485

Gaustad J. E., 1963, The Astrophysical Journal, 138, 1050

Gingold R. A., Monaghan J. J., 1977, Monthly Notices of the Royal Astronomical Society, 181, 375

Goodman A. A., Benson P. J., Fuller G. A., Myers P. C., 1993, The Astrophysical Journal, 406, 528

Haisch, Jr. K. E., Lada E. A., Lada C. J., 2001, The Astrophysical Journal, 553, L153

Hall C., Dong R., Rice K., Harries T. J., Najita J., Alexander R., Brittain S., 2019, The Astrophysical Journal, 871, 228

Hall C. et al., 2020, arXiv, 904, 148

Hall C., Forgan D., Rice K., Harries T. J., Klaassen P. D., Biller B., 2016, Monthly Notices of the Royal Astronomical Society, 458, 306

Hartmann L., Calvet N., Gullbring E., D'Alessio P., 1998, The Astrophysical Journal, 495, 385

Hayashi C., 1981, Progress of Theoretical Physics Supplement, 70, 35

Hayashi C., Nakano T., 1965, Progress of Theoretical Physics, 34, 754

Heinze A. N., Hinz P. M., Kenworthy M., Meyer M., Sivanandam S., Miller D., 2010, Astrophysical Journal, 714, 1570

Hughes A., Wilner D., Qi C., Hogerheijde M., 2008, The Astrophysical Journal, 678, 1119

Isella A., Carpenter J. M., Sargent A. I., 2009, Astrophysical Journal, 701, 260

Jiang Z., Tamura M., Hoare M. G., Yao Y., Ishii M., Fang M., Yang J., 2008, The Astrophysical Journal, 673, L175

Johnson B. M., Gammie C. F., 2003, The Astrophysical Journal, 597, 131

Jørgensen J. K., van Dishoeck E. F., Visser R., Bourke T. L., Wilner D. J., Lommen D., Hogerheijde M. R., Myers P. C., 2009, aap, 507, 861

Kitamura Y., Momose M., Yokogawa S., Kawabe R., Tamura M., Ida S., 2002, The Astrophysical Journal, 581, 357

Koch D. G. et al., 2010, Astrophysical Journal Letters, 713

Kratter K., Lodato G., 2016, Annual Review of Astronomy and Astrophysics, 54, 271

Kratter K. M., Matzner C. D., Krumholz M. R., Klein R. I., 2010, Astrophysical Journal, 708, 1585

Kuiper, 1951, Proceedings of the national acadamy of sciences, 37, 1

Lada C. J., 1987, in Star Forming Regions, Peimbert M., Jugaku J., eds., Vol. 115, p. 1

Lafreniere D. et al., 2007, The Astrophysical Journal, 670, 1367

Laplace P., 1796, The System of the World, 2nd edn. University Press for Longmans, Rees, Orme, Brown, and Green

Larson R. B., 1969, Monthly Notices of the Royal Astronomical Society, 145, 271

Lay O. P., Carlstrom J. E., Hills R. E., 1997, The Astrophysical Journal, 489, 917

Lin D. N. C., Pringle J. E., 1990, The Astrophysical Journal, 358, 515

Lissauer J. J., 1987, Icarus, 69, 249

Lodato G., Cossins P. J., 2011, European Physical Journal Plus, 126, 1

Lodato G., Price D. J., 2010, Monthly Notices of the Royal Astronomical Society, 405, 1212

Lodato G., Rice W. K., 2004, Monthly Notices of the Royal Astronomical Society, 351, 630

Lommen D., Jørgensen J. K., Van Dishoeck E. F., Crapsi A., 2008, Astronomy and Astrophysics, 481, 141

Lucy L. B., 1977, The Astronomical Journal, 82, 1013

Lynden-Bell D., Pringle J. E., 1974, Monthly Notices of the Royal Astronomical Society, 168, 603

Maret S. et al., 2020, Astronomy and Astrophysics, 635

Masunaga H., Inutsuka S., 2000, The Astrophysical Journal, 531, 350

Masunaga H., Miyama S. M., Inutsuka S., 1998, The Astrophysical Journal, 495, 346

Mayer L., Lufkin G., Quinn T., Wadsley J., 2007, The Astrophysical Journal, 661, L77

McCaughrean M. J., O'Dell C. R., 1996, The Astronomical Journal, 111, 1977

Mercer A., Stamatellos D., 2020, arXiv, 1

Mizuno H., 1980, Progress of Theoretical Physics, 64, 544

Monaghan J., Gingold R., 1983, Journal of Computational Physics, 52, 374

Morris J. P., Monaghan J. J., 1997, Journal of Computational Physics, 136, 41

Murillo N. M., Lai S. P., Bruderer S., Harsono D., Van Dishoeck E. F., 2013, Astronomy and Astrophysics, 560, 1

Nayakshin S., 2010a, Proceedings of the International Astronomical Union, 6, 101

—, 2010b, Monthly Notices of the Royal Astronomical Society: Letters, 408, 36

—, 2017, Publications of the Astronomical Society of Australia, 34

Nelson A. F., 2006, mnras, 373, 1039

Nero D., Bjorkman J. E., 2009, apjl, 702, L163

Nielsen E. L. et al., 2019, The Astronomical Journal, 158, 13

Paneque-Carreño T. et al., 2021, The Astrophysical Journal, 914, 88

Pérez L. M. et al., 2016, Science, 353, 1519

Pollack J. B., Hubickyj O., Bodenheimer P., Lissauer J. J., Podolak M., Greenzweig Y., 1996, Icarus, 124, 62

Price D. J., 2007, Publications of the Astronomical Society of Australia, 24, 159

—, 2012, Journal of Computational Physics, 231, 759

Price D. J. et al., 2018a, Monthly Notices of the Royal Astronomical Society, 477, 1270

Price D. J., Monaghan J. J., 2007, Monthly Notices of the Royal Astronomical Society, 374, 1347

Price D. J. et al., 2018b, Publications of the Astronomical Society of Australia

Pringle J. E., 1981, araa, 19, 137

Ribas Á., Merín B., Bouy H., Maud L. T., 2014, Astronomy and Astrophysics, 561, A54

Ricci L., Testi L., Natta A., Brooks K. J., 2010, Astronomy and Astrophysics, 521

Rice W. K. M., Armitage P. J., Bate M. R., Bonnell I. A., 2003, Monthly Notices of the Royal Astronomical Society, 1030, 1025

Ricker G. R. et al., 2014, Journal of Astronomical Telescopes, Instruments, and Systems, 1, 014003

Schoenberg I. J., 1946, Quarterly of Applied Mathematics, 4, 45

Shakura N. I., Sunyaev R. A., 1973, Symposium - International Astronomical Union, 55, 155

Springel V., Hernquist L., 2002, Monthly Notices of the Royal Astronomical Society, 333, 649

Stamatellos D., Ichiro Inutsuka S., 2018, Monthly Notices of the Royal Astronomical Society, 477, 3110

Stamatellos D., Maury A., Whitworth A., André P., 2011, Monthly Notices of the Royal Astronomical Society, 413, 1787

Stamatellos D., Whitworth A. P., 2008, Astronomy and Astrophysics, 480, 879

—, 2009, Monthly Notices of the Royal Astronomical Society, 400, 1563

Stamatellos D., Whitworth A. P., Bisbas T., Goodwin S., 2007, Astronomy and Astrophysics, 475, 37

Stevenson D. J., 1982, Planetary and Space Science, 30, 755

Takakuwa S., Saito M., Lim J., Saigo K., Sridharan T. K., Patel N. A., 2012, Astrophysical Journal, 754

Tanigawa T., Ohtsuki K., Machida M. N., 2012, Astrophysical Journal, 747

Terebey S., Shu F. H., Cassen P., 1984, The Astrophysical Journal, 286, 529

Terry J. P., Hall C., Longarini C., Lodato G., Toci C., Veronesi B., Paneque-Carreño T., Pinte C., 2022, Monthly Notices of the Royal Astronomical Society, 510, 1671

Tobin J. J., Hartmann L., Calvet N., Chiang H. F., Looney L. W., Wilner D. J., Loinard L., D'alessio P., 2012, Nature, 492, 83

Tripathi A., Andrews S. M., Birnstiel T., Wilner D. J., 2017, The Astrophysical Journal, 845, 44

Veronesi B., Paneque-Carreño T., Lodato G., Testi L., Pérez L. M., Bertin G., Hall C., 2021, The Astrophysical Journal Letters, 914, L27

Vigan A. et al., 2012, Astronomy and Astrophysics, 544

Vorobyov E. I., Basu S., 2010, Astrophysical Journal Letters, 714

Weidenschilling S. J., 1977, Monthly Notices of the Royal Astronomical Society, 180, 57

Williams J. P., Cieza L. A., 2011, Annual Review of Astronomy and Astrophysics, 49, 67

Wilner D. J., Ho P. T. P., Kastner J. H., Rodríguez L. F., 2000, The Astrophysical Journal, 534, L101

Yen H. W., Takakuwa S., Ohashi N., Ho P. T., 2013, Astrophysical Journal, 772